

Acoustic emission monitoring of corrosion-fatigue damage evolution in submerged steel structures: a global parametric analysis

Pieter Sytze Kingma

Acoustic emission monitoring of corrosion-fatigue damage evolution in submerged steel structures: a global parametric analysis

by

Pieter Sytze Kingma

Student Name	Student Number
Kingma	4359585

Supervisor, Chair:	Dr. L. Pahlavan	TU Delft
Supervisor:	Dr. R. Hageman	MARIN
Committee member:	Dr. H. Den Besten	TU Delft
Daily supervisor:	Ir. F. Riccioli	TU Delft
Project Duration:	Nov, 2021 - July, 2022	
Faculty:	Faculty of Mechanical, Maritime and Materials Engineering, Delft	

Preface

Dear reader,

When I started my thesis, I set three goals. 1) Go to the TU every day as much as I can, because I have learned during the pandemic that working from home brings me close to zero. 2) Graduate before my planned trip to Guatemala and Belize, which meant no room for delay. And 3) make sure to have a career to start with in September, because the government will stop funding, and I already spent too much time working in supermarkets or delivering pizzas. I am proud to say that it looks like I will be reaching all of them.

First of all, I would like to thank my supervisors Pooira Pahlavan and Remco Hageman for their supervision throughout the last 9 months. I would like to show great appreciation to Filippo Riccioli, my daily supervisor, for learning from his expertise, the valuable feedback, all the fun moments in the steel lab, the discussion over bad coffee. I know that many of my friends were jealous that they did not have a “Filippo” around for their thesis.

In addition I would like to thank an old roommate, Paul, whose old TU Delft employee card enabled an unlimited supply of free coffee, and Daan Schoorl for driving me to the TU everyday during the cold and rainy winter months until he graduated. My girlfriend, for teaching me stone cold discipline and pushing me out of the bed at 7 AM.

This research has been part of the DONUT Joint Industry Project. I was fortunate to present my findings at the yearly conference to the industrial partners. It was a valuable experience. Finally, I would like to apologize to everyone who had to bear my never ending stories about mooring chains. Now everybody knows they are awesome.

*Pieter Sytze Kingma
Rotterdam, July 2022*

Summary

Floating offshore production units are typically anchored to the seabed with mooring chains. Structural degradation of mooring chain steel can lead to premature failure with large environmental and financial consequences. In the oceanic environment, corrosion and fatigue are the dominant failure modes for mooring chains. These damage mechanisms are hard to predict and even harder to identify at early stages of damage evolution. Continuous research to develop improved monitoring techniques is performed to increase the safety and reliability of these structures. However, inspection techniques that can accurately and quantitatively diagnose these damage mechanisms in the submerged steel parts are yet insufficient.

Acoustic emission (AE) monitoring is a non-destructive evaluation technique that can identify structural degradation in solid materials. The technique consists of recording and processing the ultrasonic waves generated by irreversible changes in the material matrix due to damage growth. This research is focused on the global parametric analysis of the primary features of AE signals recorded during corrosion-fatigue experiments performed with submerged steel and non-contact sensors. Three experiments have been analyzed to assess which of the AE primary features can most accurately correlate to the fatigue damage evolution.

Signal characterization based on their energy and duration was performed to distinguish three levels of severity. Based on a global parametric analysis the hit-rate and energy-rate have the highest potential and show good correlation to the corrosion-fatigue damage evolution. However, the global features seem to differ notably between different samples and several moments with absence of recorded activity precede final failure. Performing assessment only based on the global features is not considered sufficient. Thus, local analysis methods for AE signals is suggested to extract further information on the source of the emitting damage mechanisms.

Contents

Preface	i
Abstract	ii
1 Introduction	1
1.1 Background and motivation	1
1.2 State-of-the-art	2
1.3 Research questions	6
1.4 Collaboration Partner	6
1.5 Structure of the research	6
2 Methodology	7
2.1 Introduction to ultrasound waves	7
2.1.1 Non-contact sensors	7
2.1.2 Mathematical formulation of waves	8
2.1.3 Primary Features	9
2.1.4 Rate of emission	9
2.2 Fatigue crack propagation rates	10
2.3 Image processing techniques	12
3 Experiments	15
3.1 Experimental setup	15
3.1.1 Specimens	15
3.1.2 Equipment	17
3.1.3 Instrumentation	19
3.2 Corrosion-Fatigue experiment	22
3.2.1 Testing approach	22
3.2.2 Test Matrix	22
3.2.3 Monitoring approach	23
4 Results and Discussion	25
4.1 Pre-processing	25
4.1.1 Filtering of the data	25
4.1.2 Corrosion analysis	27
4.1.3 Crack length measurements	29
4.2 Global Parametric Analysis	32
4.2.1 Sample 1	33
4.2.2 Sample 2	38
4.2.3 Sample 3	42
4.3 Discussion	49
4.3.1 Correlation of signal parameters to damage evolution	49
4.3.2 Characterization of different damage mechanisms	49
4.3.3 Experiments improvements	50
5 Conclusions and future work	52
5.1 Conclusion	52
5.2 Recommendations	53
References	56
A Primary Features	59
A.1 Sample 1	59
A.2 Sample 2	61

A.3 Sample 3	63
B Footage & Crack size measurement	65
C Pre-Corrosion data	67

Introduction

1.1. Background and motivation

In the offshore energy industry, mooring chains are deployed in floating structures to ensure a fixed position relative to the seabed. Examples of these offshore structures are floating wind turbines and solar panels, or production units to exploit natural resources. Figure 1.1, illustrates two floating structures moored to the seabed through a system of multiple mooring lines [1].



Figure 1.1: Floating structures with mooring chains, [1],[2]

The cyclic behaviour of ocean waves leads to fatigue accumulation in a mooring system. Additionally, the degradation of the chain can be accelerated by the corrosive sea water environment [3]. Mooring chains are designed to withstand the different damage mechanisms, the decay in strength and stiffness, and should maintain their safety and reliability throughout the predetermined lifetime.

Despite the design standards and regulations, premature mooring line failure still occurs more often than desired. Damage to valuable assets, environmental damages due to spillages of hydrocarbons, or fatal incidents are examples of consequences of mooring line failure. Ma et al. [4] and Fontaine et al. [5] examined over 80 mooring line failure events. They concluded that corrosion, fatigue and corrosion-fatigue contribute to almost half (46%) of the prevalent failure events in mooring chains (Figure 1.2).

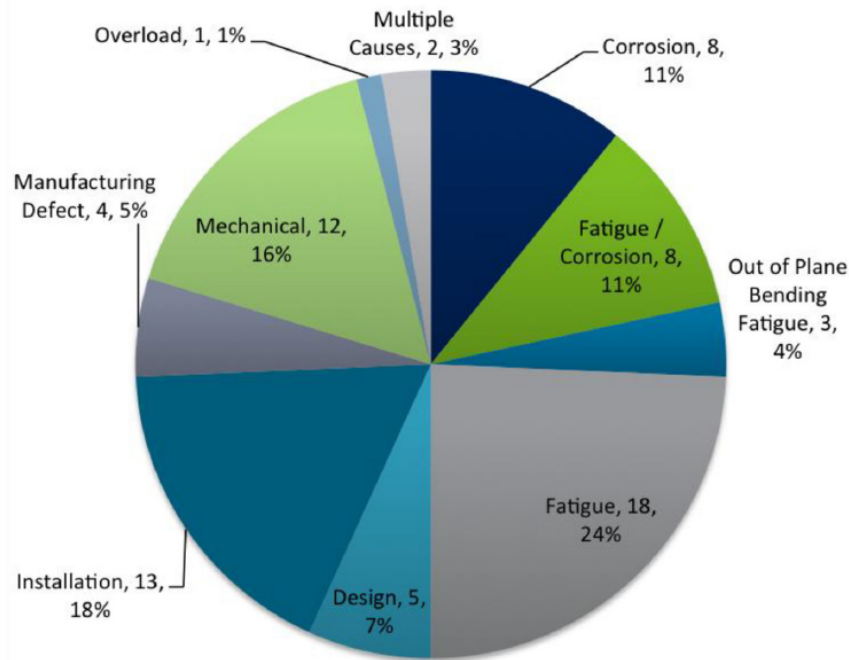


Figure 1.2: Prevalent failure modes in the survey of [5].

The complex, unpredictable and aggressive character of the corrosion and fatigue damage mechanisms lead to persistent occurrence of premature chain failure. Therefore, multiple inspection techniques have been developed to periodically evaluate the damage evolution during operation of mooring systems. Hageman et al. [6] and Wen et al. [7] presented advanced inspection technologies for mooring integrity management. Their conclusions indicate that there is still much to gain in the field of non-destructive testing (NDT) of mooring chains to assess the integrity.

Structural Health Monitoring (SHM) is the process of gathering and analyzing data from on-board sensors to assess the structural integrity [8]. On contrary to conventional NDT methods, SHM is often an integrated part of the structure to facilitate continuous monitoring. SHM aims to identify and describe structural damage or degradation at the earliest possible time in a safer, faster, and more effective way [9]. Traditionally, it consists of four stages, operational evaluation, data acquisition, feature extraction and diagnosis and prognosis.

SHM methods can be broadly divided into active and passive methods [10]. Active methods require a given excitation to the structure and measure the response, e.g. ultrasonic guided waves (UGW). For passive methods, the damage evolution itself will evoke a signal that can be measured, e.g. acoustic emission (AE). The passive character makes acoustic emission monitoring an effective inspection tool for long-term integrity assessment of structures. The focus of this thesis will be on passive methods of SHM. Acoustic emission monitoring is a technique that records the elastic stress waves that are generated by damage mechanisms acting inside or on the surface of a structure.

1.2. State-of-the-art

A variety of damage mechanisms and sources of acoustic emission exist. In this section, the relevant research on corrosion and fatigue induced AE is discussed.

Corrosion

Corrosion is the destructive attack of a metal by its reaction with the environment. This attack is the result of a chemical, bio-chemical or electrochemical interaction between the metal and the surround-

ing substances [11]. Various forms of corrosion exist, the two most prevalent forms acting on mooring chains are uniform corrosion and pitting. The two main sources of corrosion induced AE that have been identified in the past are the electrochemical reactions taking place inside a corrosion-pits and the friction and/or breaking of hydrogen bubbles that are created in the process. Figure 1.3 shows how aggressive and locally corrosion pits present themselves.



Figure 1.3: Local attack of corrosion [12]

Several authors have studied corrosion as a source of acoustic emission. Fregonese et al. [13] found that the AE activity during the initiation steps of pit corrosion was not very numerous. But when the pits start to propagate, the AE activity starts to become significant. They believe that the AE source within the pits is assumed to be friction between the evolving H₂ bubbles inside the pits.

Jirarungsatian and Prateepasen [14] investigated the possibility of using acoustic emission monitoring for detection of various corrosion mechanisms. They tried to assign certain AE features to the different stages of pit formation. Duration and resonance frequency have been used to discriminate between different AE sources. They found that bubble breakage induces signals with higher frequencies compared to the ones generated by the propagation of the corrosion pits.

Tang et al. [15] applied the acoustic emission technique to monitor pitting corrosion of Q235 carbon steel. They found that the characteristic features of pitting corrosion at the start of nucleation are low count and low to medium duration. In later stages of the pitting process, the AE hits consisted of higher count and higher duration.

Xu et al. [16] investigated AE signals for 304SS in different solutions to better characterize the AE behavior and discriminated the AE events into two categories. Type I has low values for amplitude, duration, rise time and count. Type II has higher values for these features. Duration and amplitude seem to classify the pitting process the best, and hydrogen bubble evolution is the main source of acoustic emission during pitting.

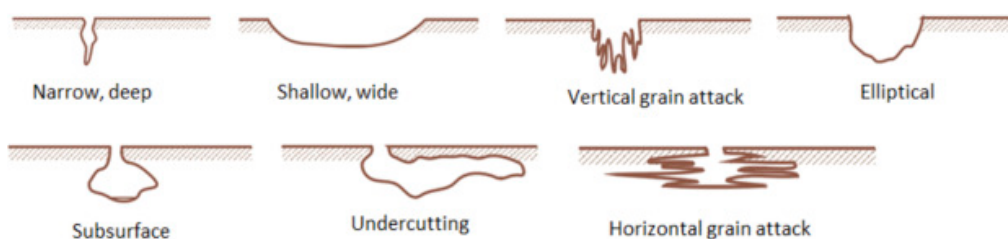


Figure 1.4: Prevalent pit shapes

Fatigue

Fatigue is considered one of the dominant failure modes for engineering structures like mooring systems. Fatigue is a degradation mechanism that can lead to failure of a structure due to cracks that are initiated by a cyclic stress [17]. Previous research has identified several sources of fatigue induced AE. Crack tip propagation is often considered the main source of AE. This is the mechanical tearing of metallic bonds that leads to the release of stress waves. Secondary AE sources can be impact of the crack tip during unloading and cyclic plasticity, which is the irreversible rearrangement of structural dislocations in the plastic zone near the crack tip.



Figure 1.5: Fatigue in mooring chain [18]

Different primary features can be extracted from the recorded AE waves to characterize and diagnose structural integrity. AE has been used to monitor fatigue damage in various materials like metals, concrete and composites. It has been demonstrated that the primary features can correlate to the fatigue damage evolution.

Moorthy et al. [19] investigated the influence of microstructure on AE signals, and found that the material microstructure influences the amount of AE activity and primary features such as count and energy. Aggelis et al. [20] tried to correlate acoustic emission features to the different stages of crack growth. It was concluded that some features are sensitive to damage processes and are prone to change in different stages of crack growth. The researchers found that a sharp increase in Duration, Rise time and Ramp indicate the transformation from tensile cracks to shear cracks.

Morton et al. [21] found that acoustic emission activity can be related to the stress intensity factor range ΔK . It can be described by the AE features as a loglinear function, the same way as the fatigue crack growth rate is described by Paris and Erdogan [22]. Roberts and Talebzadeh [23] performed fatigue tests with compact tension specimens to relate acoustic emission features to Paris' fatigue crack propagation rule. This paper aims to rewrite Paris' equations in terms of acoustic emission features. Based on the experiments a loglinear relationship between count rate dc/dN and stress intensity factor range ΔK is developed.

Yu et al. [24], Rabiei et al. [25], Kumar et al. [26] and Chai et al. [27] all contributed in trying to find the AE parameter that can most accurately correlate to the damage evolution and that is able to distinguish between the different stages of fatigue crack growth. They conclude that count and energy are the features that show the highest potential.

Chai et al. [28], Karimian et al. [29] and Sauerbrunn et al. [30] looked into entropy as the parameter to monitor fatigue damage evolution. Entropy is mathematical formulation of the waveform and is a way to describe the disorder and uncertainty within a signal.

Additionally, Bhuiyan et al. [31],[32] performed research in identifying waveform characteristics of fatigue cracks using acoustic emission. Two different types are discriminated. Type 1 is short duration, large amplitudes and energy in the 250-400 kHz frequency range and are assumed to originate from the source of fatigue crack growth. Type 2 has larger duration and energy in the 30-100 kHz frequency

band and are assumed to be induced by ‘clapping’ and ‘rubbing’ of the crack tip surface during the unloading phase of the load cycle.

Corrosion-fatigue

Corrosion accelerated fatigue is a damage mechanism that presents itself in the high cycle fatigue regime (HCF). This is the fatigue regime where the fatigue life is no longer dominated by the stress range, which is considered low cycle fatigue (LCF), but by the structural imperfections on the surface of inside the material matrix. Corrosion-fatigue is the phenomena where a corrosion pit acts as the initiation point for fatigue crack to develop. The pit-to-crack transition is referred to as the moment that the dominated damage mechanism shifts from corrosion to fatigue. Experiments trying to simulate corrosion-fatigue damage are not widely performed.

Palin-Luc et al. [33] found that the fatigue life of mooring chain at 10^8 cycles is reduced 74% when subjected to a corrosive environment (e.g. artificial sea water) compared to a non-corrosive environment of air. In a corrosive environment, the fatigue life of mooring chains can be dominated by growth of corrosion pits. Increased thickness and safety factors alone might not be sufficient to prevent premature mooring line failure. Figure 1.6 shows how a corrosive environment can influence the fatigue life.

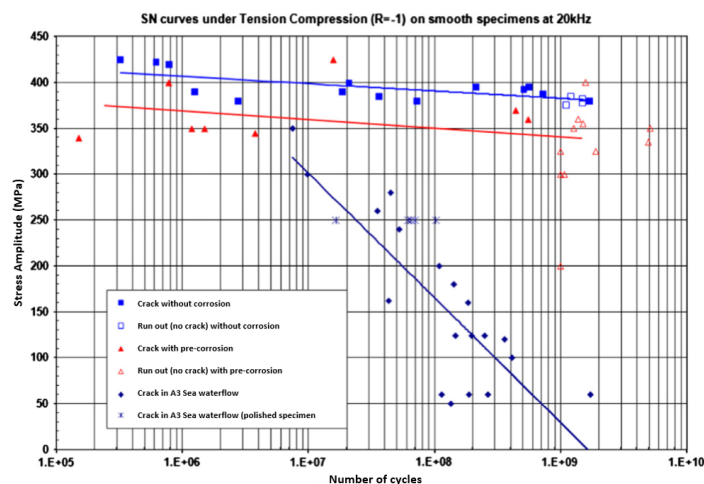


Figure 1.6: Influence of corrosive environment on fatigue life [33]

Chang et al. [34] performed acoustic emission monitoring of corrosion-fatigue damage evolution and draws similar conclusions as Roberts and Talebzadeh [23]. The count rate can be coupled to the fatigue crack growth rate through a loglinear relationship.

In order to better understand and quantify the fatigue capacity and degradation of mooring chains, a number of full scale fatigue tests have been performed. Rivera et al. [35], Angulo et al. [36] and Angulo et al, [37] performed full scale experiments with a load ratio of 0.925 and a load frequency of 0.5 Hz. The experiments were executed with the chain submerged in artificial seawater to mimic offshore conditions and lasted 72 days. They concluded that an increase in crack growth rate was related to an increase in duration, amplitude and energy. A parametric filter was designed based on the primary AE features.

Knowledge gap

According to the state-of-the-art, acoustic emission monitoring seems to be sensitive to different stages of damage evolution. Feature-based analysis can be used to examine the primary features of ultrasound signals. Count, energy and entropy have been regularly discussed and related to the fatigue crack growth rate. Waveform-based analysis can be used to interpret the distribution and similarity

between waves to relate multiple events.

Based on the literature survey, it can be concluded that non-contact acoustic emission monitoring is not widely investigated. Additionally, the acoustic emission features in the different stages of corrosion-fatigue damage evolution of submerged steel structures are not universally established. A new research direction is proposed to achieve more know-how on non-contact monitoring of fatigue crack propagation in submerged steel structures.

1.3. Research questions

By the end of the literature study a knowledge gap was found in the development of non-contact acoustic emission monitoring of corrosion-fatigue damage evolution of submerged mooring chain steel. More research using submerged specimens is desired. Given the existing state of the art and gaps in literature, the following research question is formulated:

'Which of the acoustic emission primary features can most accurately correlate to the corrosion-fatigue damage evolution of submerged mooring chain steel using non-contact sensors?'

In order to address the the main research question, three sub-questions are formulated.

- What is the contribution of corrosion-induced AE during corrosion-fatigue testing of submerged mooring chain steel?
- How do the acoustic emission features change throughout the different stages of fatigue crack growth?
- Is it possible to distinguish between sub-stages of stable crack growth based on the global primary features?

1.4. Collaboration Partner

MARIN, the Maritime Research Institute Netherlands, is one of the world's leading independent maritime institutes. MARIN is one of the companies involved in the DONUT Joint Industry Project (JIP). This JIP is coordinated by TU Delft, and organised with the help of the FPSO Forum & JIP Week. In the FPSO Forum & JIP Week, offshore energy companies, operators, contractors, yards, research institutes and safety authorities share their experience to improve the industry wide practices, [38].

1.5. Structure of the research

In order to answer the research questions, a corrosion-fatigue experiment has been performed with continuous AE monitoring of the damage evolution. A steel specimen has been pre-corroded and subjected to fatigue loading in a water tank up to failure. The recorded data was complemented by two earlier performed experiments.

In Chapter 2, the theory on the propagation and generation of ultrasound waves is discussed, and a hypothesis is formulated. Chapter 3 presents the experimental set-up, the equipment, sensors and the test matrices. Chapter 4 presents the results of the global parametric analysis of three corrosion-fatigue experiments. The chapter ends with a discussion on which primary features are most suitable to identify damage evolution. Chapter 5 contains the conclusions, recommendations for the future research and suggestions to improve test set-up for new experiments.

2

Methodology

2.1. Introduction to ultrasound waves

Acoustic emission is described as the sudden release of energy that is associated with the development of degradation, e.g., crack growth inside a material, which excites elastic stress waves that travel from the source into the surroundings and can be measured by a transducer. Sources of these elastic waves can range from structural deformation in a material matrix, to electrochemical reactions during corrosion. Depending on the source and the environment, different type of waves can exist.

Acoustic emission typically consists of elastic waves that lead to various modalities of particle motions inside a material. In a thick solid medium waves propagate in various forms. For longitudinal waves (P-waves), the motion of the particles oscillate in the direction of the traveling wave. Transverse waves (S-waves), also known as shear waves, oscillate perpendicular to the traveling direction. If a wave travels at the surface of a solid medium and the wavelength is much shorter than the thickness of the solid, the surface waves are called Rayleigh waves. When waves travel through thin plates, i.e. plate thickness decreases to the wavelength or smaller, they are referred to as Lamb waves [39].

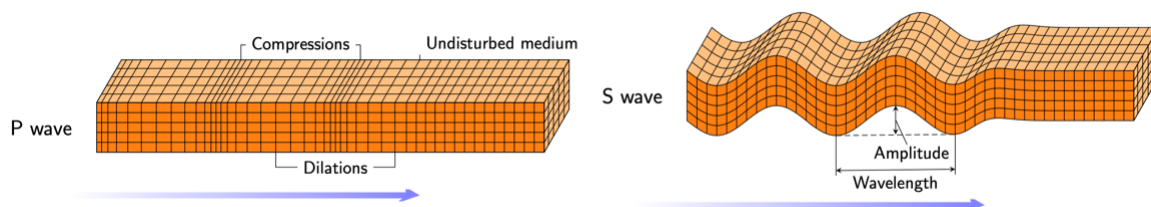


Figure 2.1: Example of P waves (left) and S waves (right)

Traditional AE monitoring consist of placing one or multiple piezoelectric AE transducers (PZTs) directly on the structure on several locations. This way, the sensors can record the waves that travel through the structure. For practical reasons it is undesirable to place the PZTs directly on the mooring chain, because they are usually covered in some layer of marine growth. Removing the accumulated marine growth from the mooring chain is not favourable for both financial and technical reasons.

2.1.1. Non-contact sensors

Figure 2.2 exemplifies the emission of elastic waves due to a damage mechanism acting on the chain. In case of corrosion-fatigue damage evolution at the surface of submerged mooring chains, a variety of waves are excited and travel through the steel chain links. Detaching the sensors from the structure brings some challenges. Not all of the damage induced waves are able to transfer from the solid steel to the liquid seawater. Unlike P-waves, S-waves are not able to propagate through a fluid. This means

that, when using non-contact sensors only, the evaluation of the state of integrity can be performed only using the recorded waves that were successfully transmitted to the liquid.

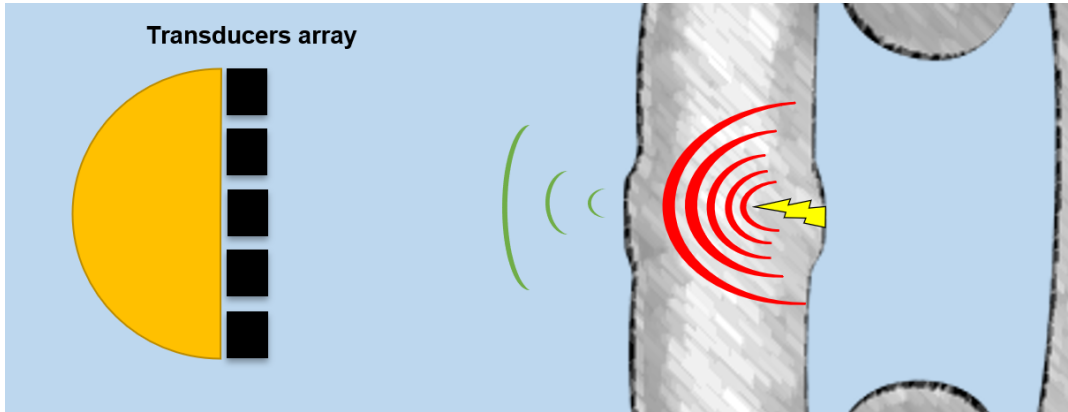


Figure 2.2: Schematic example of wave generation in submerged mooring chain

Krautkramer et al. [40] discussed the possibility for elastic waves to travel from one medium to another. Krautkramer explains that, under certain conditions, waves are able to switch from solids to fluids, although usually in a more or less altered direction, intensity and mode. Alkhateeb [41] studied the possibility of measuring damage induced signals with submerged non-contact sensors. Emitted signals were successfully recorded, but the magnitude and the quality of the data descended considerably.

2.1.2. Mathematical formulation of waves

Pahlavan et al. [42] and Scheeren et al. [43] presented an analytical framework to describe the propagation and transmission of ultrasonic waves through the geometry and interfaces of steel structures. Similar notation can be used to describe an elastic wave that is generated at the source and the corresponding signal that is presented by a data acquisition system. Figure 2.3 presents a schematic overview of a situation of non-contact monitoring of a submerged mooring chain.

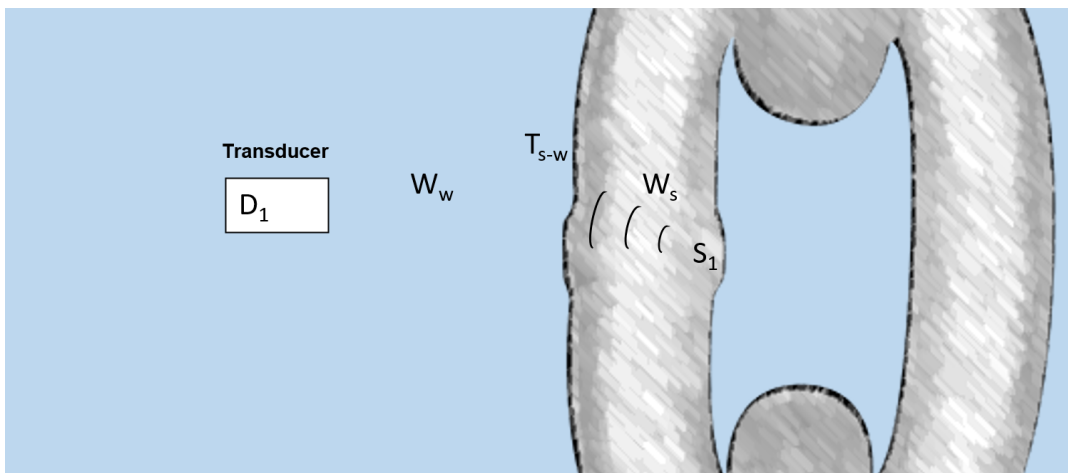


Figure 2.3: Propagation of waves from source S_1 to sensor D_1

In Figure 2.3, the source S_1 and the sensor D_1 are located at the shown positions. If an AE signal is generated due to a change in the material matrix, it start propagating away from the source. If the wave has sufficient energy, it can propagate into the water and be recorded by the non-contact AE transducer. The measured signal P_1 , represented in Equation 2.1, is the convolution of the source signal S_1 , with the wave propagation function of both the structure W_s and the water medium W_w , the

transmission between the two media T_{w-s} and the transfer function of the receiving sensor D_1 . The analytical formulation of the measured signal is a convolution operation in the time domain:

$$P_1 = D_1 * W_w * T_{w-s} * W_s * S_1 + N_1 \quad (2.1)$$

where $*$ represents convolution, and N_1 denotes all mode conversions, scattering of the transmitted responses and environmental noise. In case of non-contact acoustic emission monitoring of mooring chains, a layer of marine growth even adds an additional layer between the source and the signal, adding more components to the equation.

2.1.3. Primary Features

Figure 2.4 presents the primary features of the AE signal that are typically used to perform conventional acoustic emission analysis. A short description of these features are listed below. AE waves are commonly presented in function of time and their amplitude in voltage, often in mV or dB.

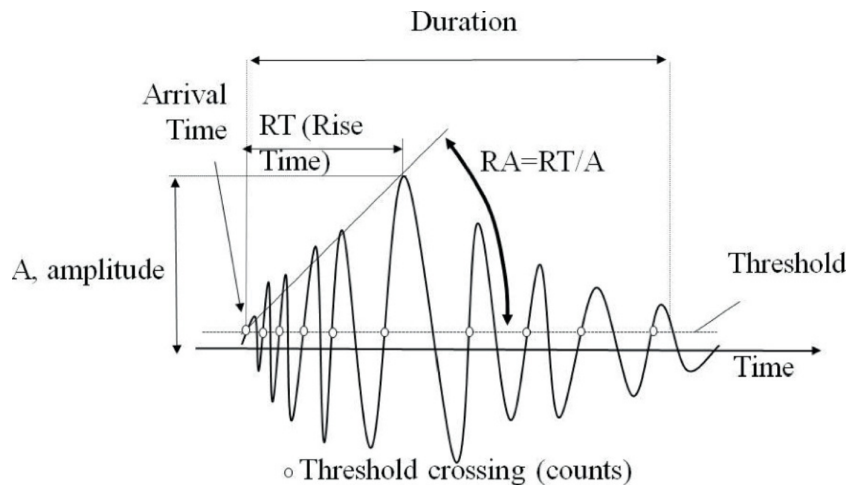


Figure 2.4: Example of AE waveform in the time domain, [39]

- Hit: a signal that exceeds the threshold and is recorded by the data acquisition system.
- Threshold [mV]: A predefined voltage that must be exceeded by the incoming waveform in order to trigger the acquisition. It ensure the avoidance low amplitude noise signals.
- Amplitude, A [mV]: The peak voltage of the signal waveform (positive or negative).
- Rise Time, RT [μs]: the time interval between the triggering time of AE signal (1st count) and the time of the peak amplitude.
- Duration, DUR [μs]: the time interval between the 1st count and the last descending threshold crossing.
- Average Frequency, AF [Hz], which is calculated in time domain as the ratio of the total number of counts over the duration of the waveform in Hz.
- Counts [-]: the number of times within the signal, that the threshold is exceeded in an upward crossing.
- Energy, ENE [eu]: Energy is generally defined as a measured area under the rectified signal envelope (MARSE). The unit eu is energy unit : $1 [eu] = 10^{-14} [V^2s]$

2.1.4. Rate of emission

The results of AE analysis often consists of graphs presenting the primary features plotted against the time, load cycles, the crack length or some other damage indicator. Conclusions can be drawn on

the evolution, magnitude and frequency of the parameters. When describing experiments that have been continuously monitored throughout the entire lifetime, the cumulative of some of the features like count and energy is often presented. From a practical point of view, for operational mooring chains, it could be less convenient to monitor the entire lifetime, and thus make the cumulative an ineffective indicator for damage. Therefore, the rate of emission will be investigated to provide more effective and serviceable results.

The rate of emission can be derived for all the primary features. In literature, count-rate, energy-rate and hit-rate have been regularly studied. The derivation of these parameters is discussed with energy as example. The energy-rate is described as the average release of energy per load cycle and is calculated using equation 2.2.

$$dE_w/dn = \left(\sum E_w \right) / N \text{ for } \{i = 1, 2, \dots, W\} \quad (2.2)$$

$$N = \frac{n_{total}}{W} \quad (2.3)$$

The equation makes use of a pre-defined amount of cycle windows, W . The window size, N is a function of the total load cycles until failure divided by the amount of cycle windows.

$\sum E_w$ is the sum of the energy of all the hits that are recorded within a window. The rate of emission is the summated energy divided by the window length. In other words, the rate of emission is the average emitted energy per cycle. The rate of emission can also be calculated in the form of hit-rate. This is the average amount of recorded signals per load cycle.

2.2. Fatigue crack propagation rates

In 1963, Paul. C. Paris and Fazil Erdogan published a paper that presented a mathematical formulation to approximate the fatigue crack propagation rate [22]. The relationship is presented in Equation 2.4 and relates stress intensity factor ΔK to the fatigue crack growth rate da/dN .

$$da/dN = C(\Delta K)^m \quad (2.4)$$

$$\Delta K = Y(a)\Delta\sigma\sqrt{\pi a} \quad (2.5)$$

Where C and m are material dependent properties that can be empirically found. Stress intensity factor ΔK is a fatigue damage parameter defined by the crack length a , the applied stress range σ and $Y(a)$, which is a multiplication factor that is described by the location and orientation of the crack with respect to the load and geometry. Igwemezie et al. [44] combined experiments and previous research to present empirically found values for m and C for marine steel.

The authors divided the fatigue life into three stages. Stage I encompasses the start of the fatigue life and crack initiation. Stage II is the stable crack propagation phase. Stage III is the unstable crack propagation phase that leads to imminent failure. Their relationship is demonstrated in Figure 2.5. The loglinear part of the red line approximates the fatigue crack propagation rate. The relationship states that the growth rate, da/dn , increases with an increased crack length, a . Several authors have tried to relate acoustic emission characteristics to the different stages of crack growth using this relationship [24], [27],[45]. The relationship will be used in this thesis to draft a hypothesis.

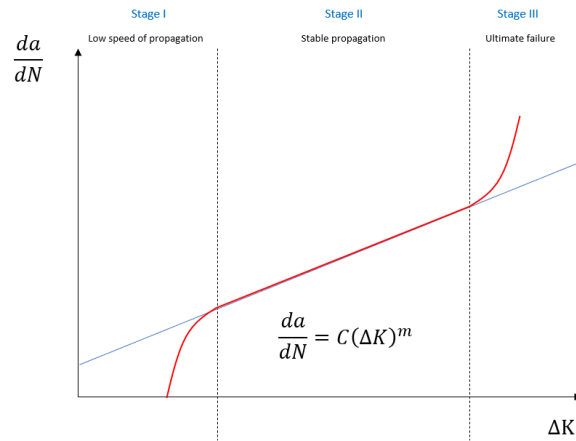


Figure 2.5: Paris' crack propagation relation.

Fatigue induced acoustic emission

Based on Paris' relation between crack length and crack growth rate, a hypothesis can be formulated. Elastic stress waves are generated through the release of energy in propagating crack tips. Theoretically, the magnitude of released energy is assumed to increase throughout the fatigue life.

In the book of '*Fatigue of structures and materials*' by Jaap Schijve [17] it is explained that the stress intensity factor K gives an indication of the stress severity around the tip of a crack. For increasing crack lengths, the local peak stress at the crack tip is also increasing. This assumption is exemplified in Figure 2.6. The figure shows the stress distribution in two vertically loaded plates. The peak stress for the left specimen σ_{peak1} at crack length a_1 is smaller than the peak stress σ_{peak2} at crack length a_2 .

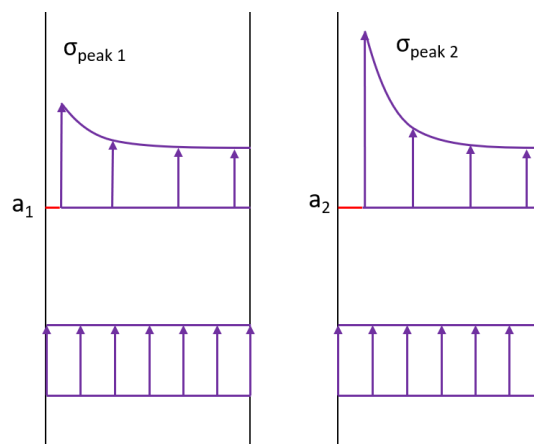


Figure 2.6: Difference in peak stress at the crack tip for different crack lengths.

Higher stresses in the crack tip are expected to lead to higher stress releases during crack tip propagation. Based on this notion, the emission of elastic stress waves should increase in magnitude for higher crack lengths. Therefore, the recorded release of energy should increase towards the end of the fatigue life.

According to Krautkramer et al. [40], if the energy of the emitted waves increase for larger crack sizes, it should also lead to more and more waves being able to switch media. In case of submerged mooring chains, it is expected that the hit-rate increases with some correspondence to the increased crack length.

Figure 2.7 highlights two regions in the stable crack propagation stage of Paris' relation. It is expected

that the fatigue cracks propagating in region B emit signals with higher energy in comparison to region A. This means that either the energy of the recorded hits increases throughout the experiment, or the hit-rate increases towards the end of the fatigue life, because in earlier stages the energy of the emitted signals was too low to exceed the threshold of the sensors.

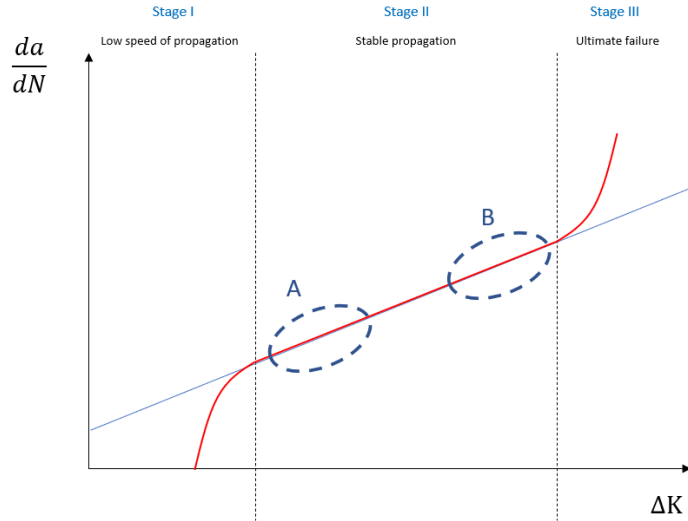


Figure 2.7: Two regions of different propagation rates

In other published work involved with investigation of energy emission, this hypothesis could be confirmed. Figure 2.8 presents two examples found in literature from acoustic emission measurements that indicate a sharp increase in release of energy towards the end of the fatigue life. More examples of this behaviour have been found in the work of Kumar et al. [26], Sauerbrunn et al. [30] and Angulo et al. [37]. The work of these authors shares the objective of finding the signal characteristics that identify early stages of crack growth. The novelty of this research is the implementation of non-contact submerged monitoring.

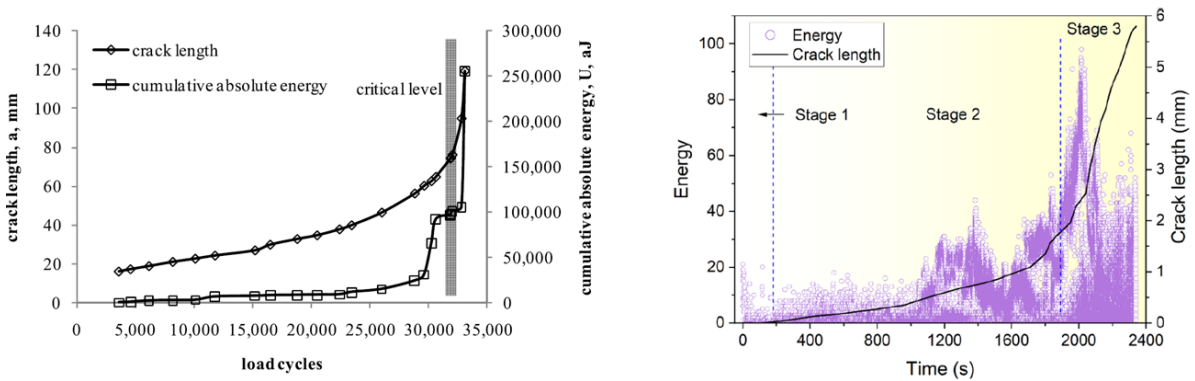


Figure 2.8: AE measurements from (left) Yu et al. [24] and (right) Chai et al. [46]

2.3. Image processing techniques

One of the goals of the experiments is to monitor and measure the crack length. An accurate crack length can be used to derive the fatigue crack propagation rate and the stress intensity factor range ΔK . Chapter 3 will present the monitoring techniques that have been used. In this section it is discussed how image processing can be used to approximate the crack length.

Throughout the experiment, pictures and videos will be made of the fatigue experiment. By means of image processing, the differences between the pictures (or frames of a video) can be subtracted from each other to expose the differences. In case of fatigue crack propagation, the differences between two pictures made between a certain amount of load cycles will represent the crack that has grown. Figure 2.9 shows a schematic example of how the identification of crack growth is performed.

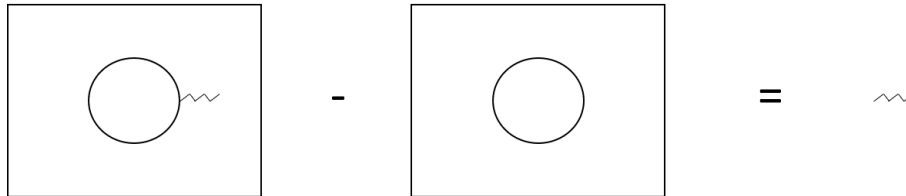


Figure 2.9: Primitive example of image processing

The figure shows two hypothetical images. They contain a plate with a hole in the middle. The left image contains a crack, and the right one does not. With image processing, the matrices defining the colors of the figure can be subtracted to expose the differences between the images. What is left from this example is a floating crack.

Digital images can be described by a matrix that contain color codes for every pixel. An example of how this process works is exemplified in Figure 2.10. The black and white shapes in this figure are described by their corresponding matrices. This example shows how two images consisting of 16 pixels can be compared to one another. Images with higher resolution are described by larger matrices and color in images is described with use of $M \times N \times 3$ dimensional matrices with specific red, green and blue components.

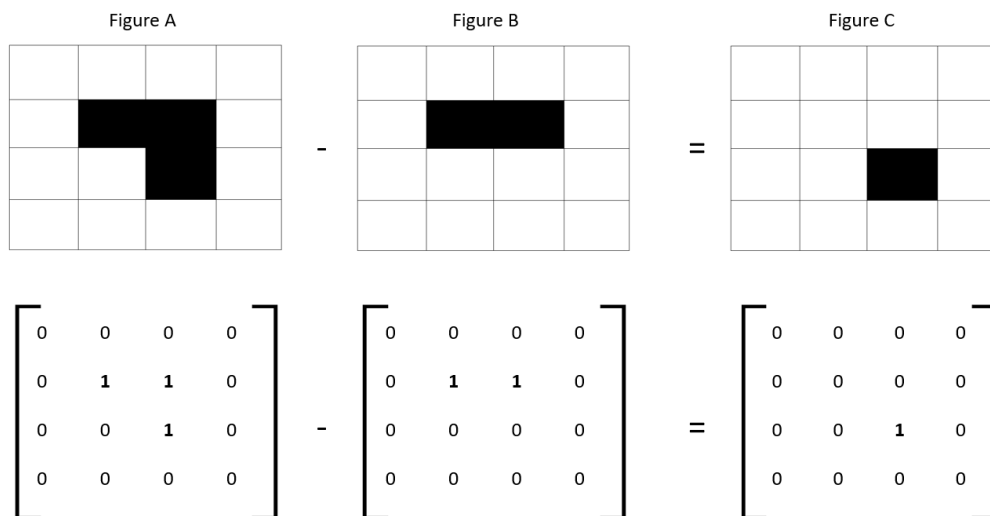


Figure 2.10: Digital image processing

In order to achieve the highest accuracy of exposure of the crack, the images must be aligned perfectly. This is generally executed by marking the object of interest with reticle patterns, like a crosshair. A crosshair acts as a reference point and can be used to align two images even if there is a displacement between the two figures. By analyzing a the section of two figures that contain the crosshairs, it is possible to find the shift in horizontal and vertical direction. A simplified overview of this process is present in Figure 2.11.

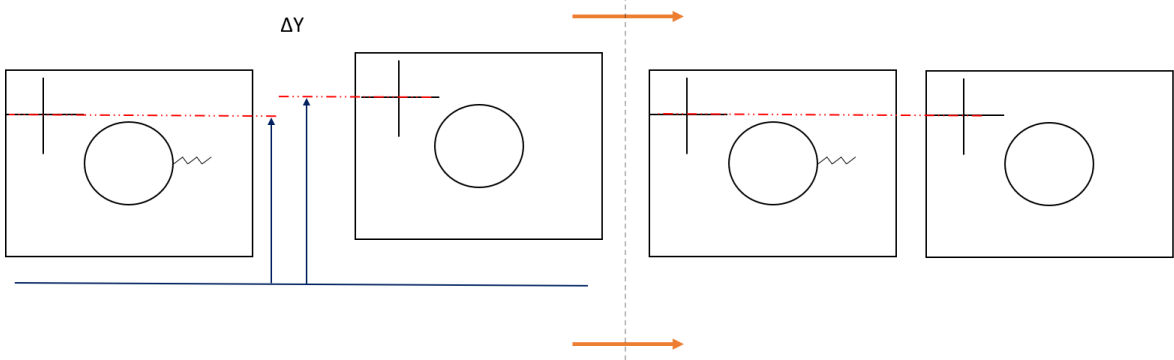


Figure 2.11: Primitive example of image processing

ΔY can be derived by comparing the distance between the crosshairs and an additional reference line. In this example, the blue line at the bottom denotes the reference line. Once the vertical shift is eliminated, the process can be repeated for the horizontal shift ΔX . Ideally, this process should approximate perfect alignment. The results of the visual observation are presented in Section 4.1.3. In case of rotated and highly deformed shapes, it becomes increasingly difficult to perform this operation accurately. The outcome of the results will be used to assess if the presented technique can obtain the desired accuracy.

3

Experiments

Corrosion-fatigue experiments have been performed to study the acoustic emission generated during evolution of damage. The experiments cover two types of mooring chain damage, being corrosion and fatigue. This chapter discusses the applied techniques and methods to monitor the degradation of submerged steel. Also, the equipment used in these experiments is motivated.

3.1. Experimental setup

3.1.1. Specimens

The goal of the experiments is to monitor the damage mechanisms acting on submerged steel structures. Dogbone shaped specimens have been used to resemble offshore mooring chains. Figure 3.1 shows how a rectangular plate can be an representative specimen to simulate the damage mechanisms acting on the surface of a chain link.

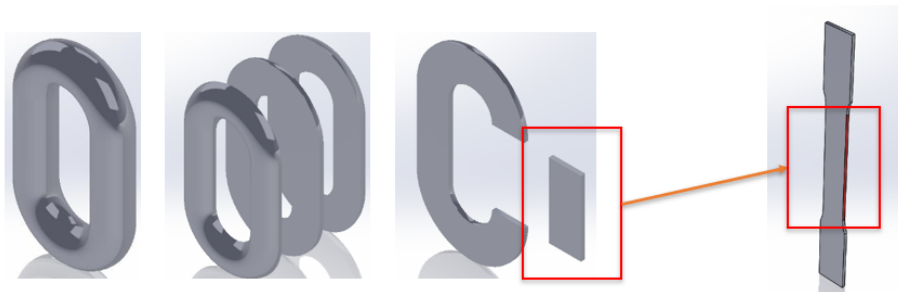


Figure 3.1: From chain link to specimen.

Figure 3.2 shows a schematic overview of the dogbone specimen used for the experiments.

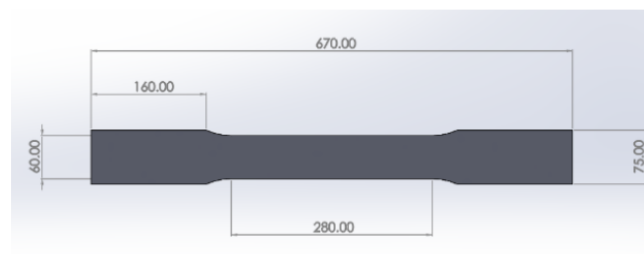


Figure 3.2: Dimensions of the dogbone specimen

Steel Grade

Typically R3, R3S, R4, R4S and R5 grade steel are the alloys used in mooring chain manufacturing, [47]. The experiment was executed with an S420NL specimen. Table 3.1 shows the properties of S420NL and the resemblance to the properties of R3 and R4 steel.

Steel grade	Yield stress N/mm ²	Tensile strength N/mm ²	Elongation %
R3	410	690	17
S420NL	420	480-620	20
R4	580	860	12
S600NL	600	650-820	11-13 at 20 c°

Table 3.1: Reference steel grades

Preparation of the specimen

To prevent leakages during the test, the specimen must be connected the bottom of the water tank. The procedure works as follows.

The steel specimen is glued to a connector disc using a flexible glue. Figure 3.3 shows the different components used in the preparations of the specimens. Once the connector disc is properly bonded to the specimen. The specimen can be placed inside the corrosion cell. The disc is mounted on the bottom plate of the cell with nuts and bolts and a neopreen sealing ring. Once the nuts and bolt are tightened, the corrosion cell is watertight. It is of great importance that the connector disc is placed exactly perpendicular to the specimen. Once the specimen is loaded, vertical deformation will lead to stress variations in the mounting kit. If the angle between the disc and the specimen deviates to far from 90 degrees, the kit will disband during the fatigue experiment with consequence of leakage. Checking for leakage at the bottom of the corrosion cell should be performed regularly throughout the experiment.



Figure 3.3: Connecting the specimen to the connector disc.

Exposed surface

One of the goals of the experiment is to create controlled environment with a predetermined location of failure. This is achieved by manually creating a hot spot where the specimen will fail during the fatigue test. In advance of the experiments and the mounting to the connector disc, except for a small circular area in the middle of the plate, the steel specimen is treated with a thin layer of epoxy to protect the steel from the accelerated corrosion. The so called "exposed surface" is the only part of the steel specimen that is in direct contact with the artificial seawater. Figure 3.4 shows how the exposed surface and the location of the strain gauge is protected when applying the epoxy layer to the specimen. The two pieces of tape are removed after once the epoxy has dried.

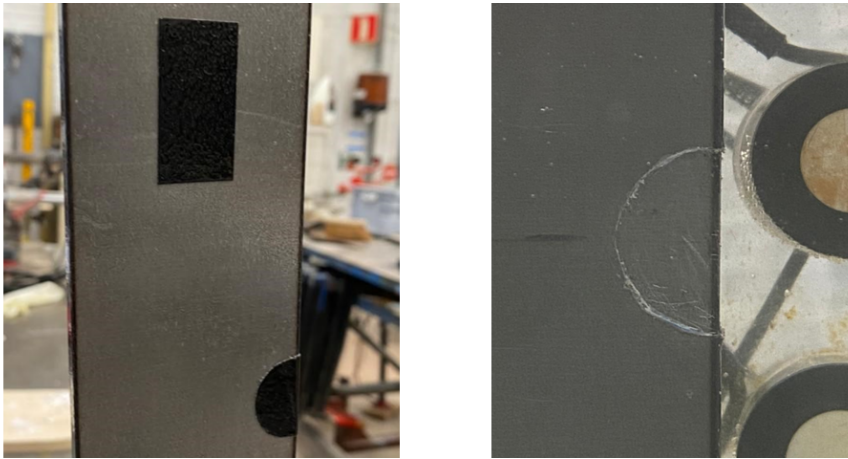


Figure 3.4: Sealing tape on the location of the exposed surface and strain gauge (left) and result (right).

3.1.2. Equipment

Different types of equipment have been used for the various aspects of this multidisciplinary experiment. The fatigue related items are the Instron fatigue testing machine, the dogbone specimens, as discussed above, and the strain gauge, used for measuring the elongation of the specimen throughout the experiment. The corrosion related items are the different electrodes and the power station. The monitoring related items are the two types of AE sensors, the hydrophones, the sensor holder and the data acquisition system (DAQ). For the visual observation an underwater camera has been used.

Fatigue testing machine and corrosion cell

The specimens have been loaded using the Instron axial-torsion servo-hydraulic fatigue testing system. This machine is located in the steel lab of the Civil Engineering and Geosciences faculty. In addition to this machine, a corrosion cell is introduced to be able to perform submerged fatigue testing. Submerged fatigue testing is rarely performed due to the risk of leakage and the potential damage to the equipment as a consequence.

Figure 3.5 shows a schematic and real view of the fatigue testing machine and the corrosion cell. The ingenious element of this set-up is that the corrosion cell remains water tight even though the steel specimen is being deformed in vertical direction.

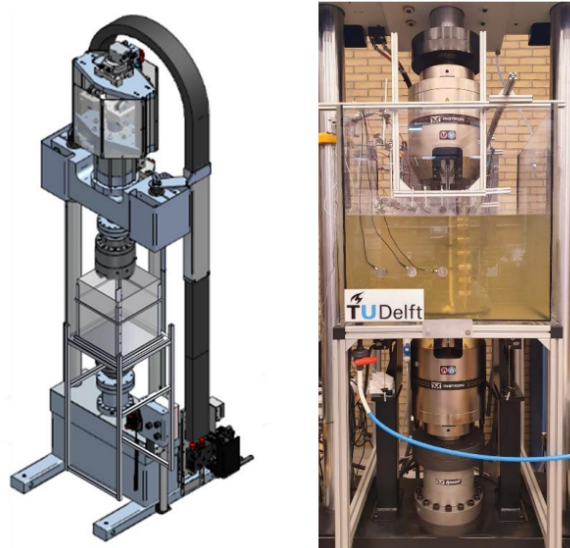


Figure 3.5: Instron fatigue testing system extended with corrosion cell

Accelerated corrosion

Artificial seawater is used to simulate the environment of mooring chains and is achieved by creating a solution of water and sodium chloride (NaCl). The desired salinity is obtained keeping a 3.5% NaCl concentration. This is obtained with a salinity meter and a temperature meter. The process is displayed in Figure 3.6.



Figure 3.6: Production of artificial seawater and salinity test (middle)

The corrosion process has been accelerated with help of a potentiostatic system. The steel plate is part of a electrical circuit with three electrodes. The objective of this system is to enforce the corrosion process by applying a current to the steel specimen. In the accelerated corrosion process, the steel plate will act as the working electrode. A graphene bar works as counter electrode, and a silver rod is added as reference electrode to measure the current. A DC power supply is used to set a fixed electric potential of -0.541 V over the system. The current increases the amount of oxygen atoms to react with the iron particles in the steel specimen and, therefore, increases the iron dissolution rate.

Figure 3.7 shows the potentiostatic system and the electrodes placed in the corrosion cell. In the left figure, the black clamp is gripped to the steel plate that will act as the working electrode. The red clamp is connected to the graphene bar and will act as the counter electrode. The silver electrode is wired to the potentiostatic system to monitor the electric potential in the corrosion cell.

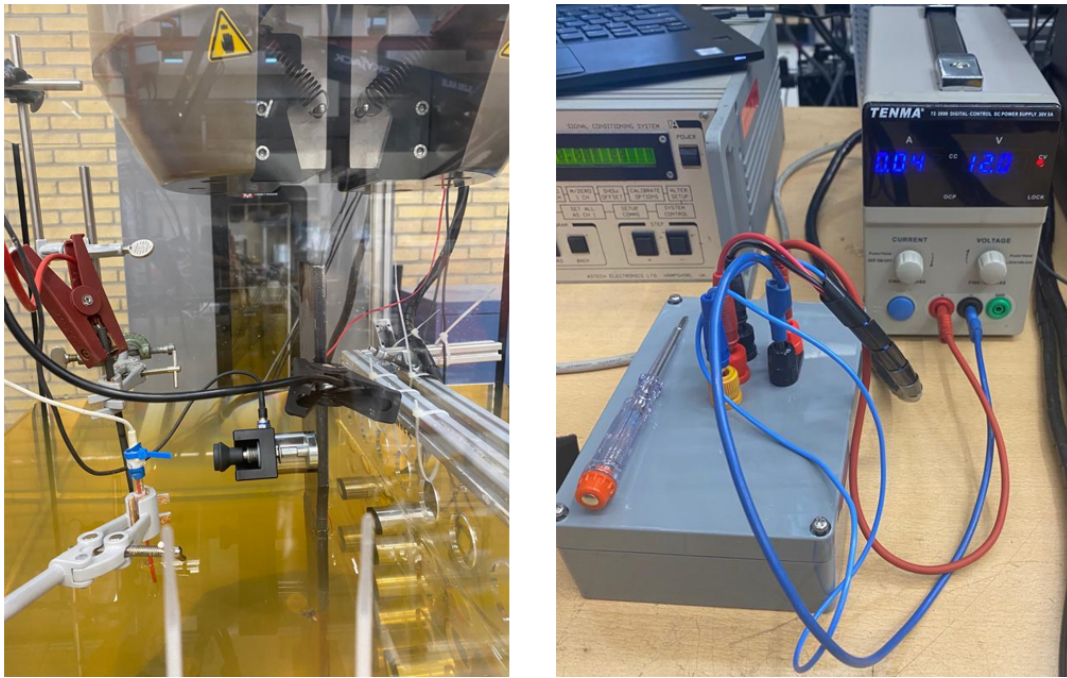


Figure 3.7: Placement of the nodes and clamps (left) and the potentiostatic system (right)

3.1.3. Instrumentation

Underwater camera: GoPro

One of the objectives of the experiments is to measure the crack propagation rate. The visual observation is performed with a GoPro Hero 8 to continuously monitor the crack length. The GoPro is displayed in figure 3.8. The camera is not equipped with a manual focus function, but it focuses on objects located at least one foot away. Therefore, it is not possible to place the GoPro at a close distance.

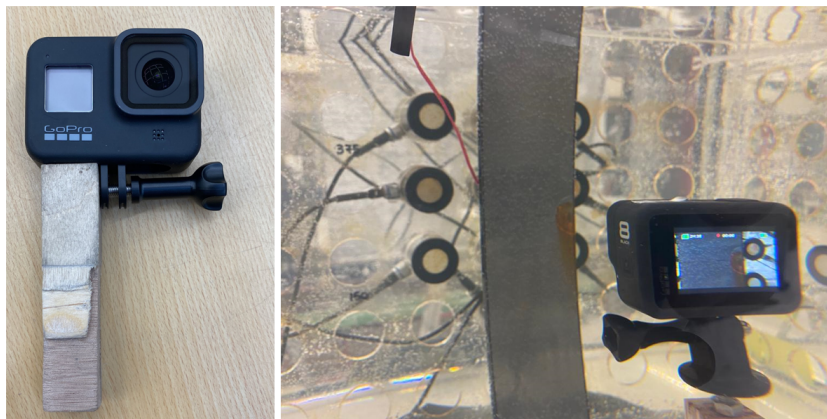


Figure 3.8: GoPro placed on mount.

Figure 3.9 shows the crack path of two previously performed experiments for sample 1 and 2. From the figures can be seen that the crack path starts either at the top or the bottom of the exposed surface. The settings of the camera are set to shoot footage with a frame rate of 24 fps. The frame where the specimen is loaded with the highest stress can be found manually by investigating 24 consecutive frames after the start of the fatigue test. Once this frame number is found, the frames can be sampled every 24 frames. As a result, each sampled frame shows the specimen is in fully stretched position.

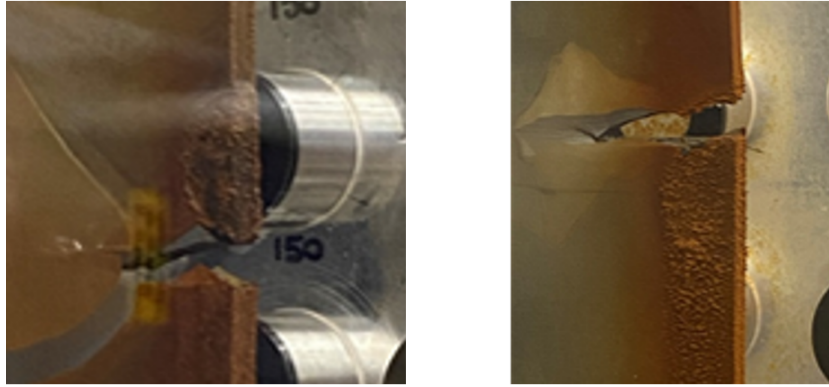


Figure 3.9: Crack path sample 1 (left) and sample 2 (right)

The battery and mini SD are two minor barriers to the corrosion-fatigue experiment. A fully charged battery will run out of power after approximately 1.5 hours of filming. An additional battery pack, an extra SD card and a charging station are used to ensure that the experiment does not have to be paused to charge the battery.

Acoustic emission sensors

Two type of sensors have been used to monitor the acoustic emission induced by the different damage mechanisms. Piezoelectric acoustic emission transducers with integrated preamplifier are the first type to be used to monitor the elastic waves generated during the corrosion-fatigue experiments. An AMSY Vallen Data Acquisition System is used to record the signals from the transducers. A laptop is connected to the data acquisition system to save the data and to visualise the monitored signals in real-time. The properties of the different sensors are displayed in table 3.2.

Quantity	Type	Frequency range [kHz]	Sampling Frequency [MHz]
8	VS150-WIC-V01	100-450	2.5
4	VS375-WIC-V01	250-700	2.5

Table 3.2: Acoustic Emission Transducers

These watertight sensors have integrated pre-amplifiers of 34 dB and are of the resonant type. This means they are specifically sensitive to signals with a frequency content close to the resonant frequency. To ensure the ability to record a broad spectrum of signals, two different resonant sensors have been chosen. Figure 3.10 shows the frequency response of the two sensors. The graphs show the frequency ranges of the two types of sensors.

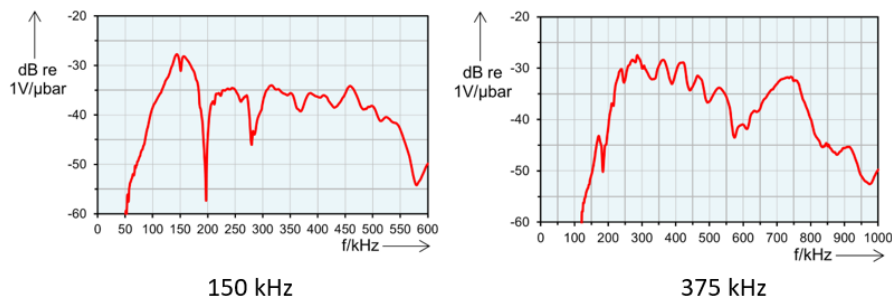


Figure 3.10: Frequency response function of 150 kHz (right) and 375 kHz (left) sensors

Hydrophones

In addition to the Vallen AE sensors, custom made hydrophones are added to the experimental set-up compared to the previous two experiments. These sensors are connected with external amplifiers located between the sensor and the DAQ. Figure 3.11 presents the two types of sensors used in this experiment. The hydrophones are the outer four black sensors.



Figure 3.11: 9 Vallen AE sensors and 4 hydrophones.

Sensor Layout

Figure 3.12 presents the sensor layout for the previous two experiments and the renewed sensor layout for the experiments performed in this thesis. In the first two experiments, six 150 kHz sensors were placed in an array in front of the specimen. The remaining sensors were placed at varying locations in the corrosion cell to investigate how far signals emitted from the exposed surface could reach. The results of the first two samples will be discussed in Chapter 4.

For the new round of experiments, the AE sensors were placed in the "patch" formation. Outermost sensors 1 and 6 from the first two experiments were placed in a cross. The 375 kHz sensors are placed closely to the 150 kHz sensors. The hydrophones were placed at the edge of the patch, as they were allocated after the pre-corrosion process.

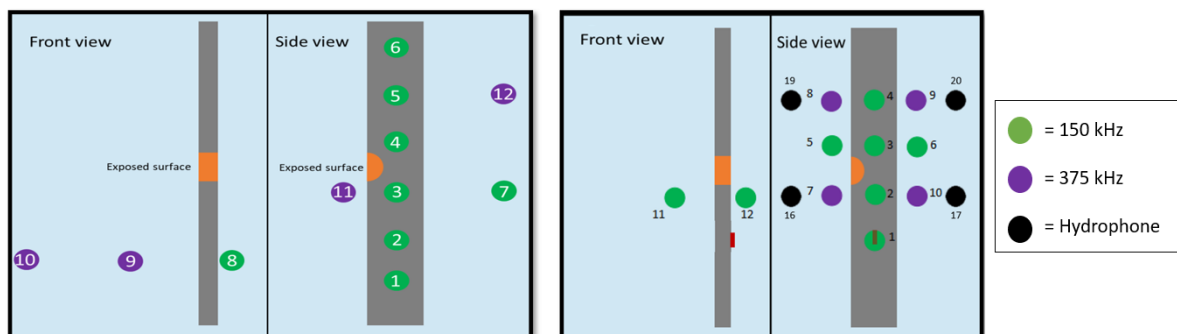


Figure 3.12: Sensor layout for sample 1 and 2 (left) and sample 3 (right)

3.2. Corrosion-Fatigue experiment

3.2.1. Testing approach

The experiments consist of two phases. The pre-corrosion phase and the corrosion-fatigue phase. Two dogbone shaped specimens of S420NL grade steel have been be treated with accelerated corrosion for five days, which is approximately 100 hours. The test plan for five weeks of experiments is presented in figure 3.13. In the first two weeks, sample 3 and sample 4 have been subjected to accelerated corrosion in the water tank.

	31 Jan. 2022	1 Feb. 2022	2 Feb. 2022	3 Feb. 2022	4 Feb. 2022	5 Feb. 2022	6 Feb. 2022	7 Feb. 2022	8 Feb. 2022	9 Feb. 2022	10 Feb. 2022	11 Feb. 2022	12 Feb. 2022	13 Feb. 2022	14 Feb. 2022	15 Feb. 2022	16 Feb. 2022	17 Feb. 2022	18 Feb. 2022	19 Feb. 2022	20 Feb. 2022	21 Feb. 2022	22 Feb. 2022	23 Feb. 2022	24 Feb. 2022	25 Feb. 2022	26 Feb. 2022	27 Feb. 2022	28 Feb. 2022	1 Mar. 2022	2 Mar. 2022	3 Mar. 2022	4 Mar. 2022				
Pre-corrosion sample III																																					
Pre-corrosion sample IV																																					
Commissioning of corrosion-fatigue setup																																					
Commissioning of sample III																																					
Corrosion-fatigue sample III																																					
De-commissioning sample III																																					
Commissioning of sample IV																																					
Corrosion-fatigue sample IV																																					
De-commissioning sample IV																																					
Commissioning of small scale chain links																																					
Noise assessment test chain links																																					
De-commissioning and closure																																					

Figure 3.13: Test plan as executed

After the fatigue test of specimen 3, small scale chain links have been subjected to corrosion-fatigue in one day of testing. The goal of this experiment was to monitor the noise that the shackles produce under cyclic loading. The results of these experiments are not part of this thesis and, therefore, not discussed in this report. However, the chain links can be seen in Figure 3.11.

3.2.2. Test Matrix

The load conditions for sample 3 and 4 in are listed in Figure 3.14. The table contains the load levels, load ratio R , the expected fatigue cycles (EFC) and the total fatigue cycles (TFC) as measured in the experiments.

The predicted cycles to failure are calculated using the DNVGL offshore standard for position monitoring: DNVGL-OS-E301 [48]. The mean SN curve is calculated using equation 3.1. Where $\log(a) = 12.8$ and $m=3$. m is a material specific variable and a is the condition of simultaneous corrosion-fatigue loading of the specimen. $\Delta\sigma$ is the stress range and N is the total number of cycles. The total amount of cycles can be estimated based on the applied stress range. The total amount fatigue cycles up to failure are subject to variability in microstructure and differentiate both above and under the expected value.

$$\log(N) = \log(a) - m * \log(\Delta\sigma) \tag{3.1}$$

	No.	Pre-corroded/Pristine	Load level [kN]	Frequency [Hz]	σ_{mean} [Mpa]	σ_{min} [Mpa]	σ_{max} [Mpa]	R	Expected fatigue life** (cycles)	Obtained fatigue life (cycles)
Done	1	Pre-corroded	96 (30% MBL*)	2	200	50 (24 kN)	350 (168 kN)	0,14	250.000	107.471
Done	2	Pristine	84 (26,5% MBL*)	2	175	50 (24 kN)	300 (144 kN)	0,16	400.000	396.044
	3	Pre-corroded	99,6 (31,4% MBL*)	2	208	65 (31 kN)	350 (168 kN)	0,18	275.000	-

Figure 3.14: Test matrix

3.2.3. Monitoring approach

Two cameras have been used for the crack length measurement. Due to the boundaries of the batteries for the camera, it was not possible to run the fatigue test for the entire day continuously. One day of testing has been split into one hour runs of 7200 load cycles. After every 7200 load cycles, pictures have been taken with a 12 MP camera from outside of the corrosion cell. During each run of 7200 load cycles, the underwater camera filmed the fatigue test. Over 40 hours of footage has been shot to visualize the damage of the specimen.

At the end of every run, around 7150 load cycles, the AE measurement and the fatigue test would be paused. At this moment, the underwater camera would be removed and pictures would be taken from the loaded specimen. After the pictures had been taken, the fatigue test continued for the last couple of load cycles. During this moment, the SD card and battery of the underwater camera were replaced for a charged battery, an empty SD card and a new AE measurement were prepared. Once the 7200 cycles were completed, a new program of 7200 cycles would be started, the underwater camera would be placed, and once the fatigue test was running properly around the mean value, the new AE measurement would be started.

The interruption of the fatigue test lasted between 3 to 5 minutes. It is assumed that these breaks did not influence the fatigue life of the specimen.

Previous experiments

The corrosion-fatigue experiments of sample 1 and 2 have been performed by other researchers contributing to the DONUT JIP. The experiments have been performed under similar loading conditions. In Table 3.15, the conditions and outcome of these two experiments are presented. Sample 1 was subjected to accelerated corrosion before starting the fatigue test. During the pre-corrosion process several corrosion pits might have been formed that increase the surface roughness. These pits can act as initiation point for fatigue cracks and, depending on shape and size, severely decrease the fatigue life. Sample 2 started the submerged fatigue test without the pre-corrosion phase. The projected fatigue life of 250.000 - 400.000 cycles fall in the mid cycle fatigue (MCF) range. This suggests that the influence of interior and exterior defects does not necessarily play a significant role in fatigue life. However, it is interesting to see that the pre-corroded specimen failed much sooner than anticipated. The difference between expected fatigue life and measured fatigue life underlines the risks of the highly unpredictable character of corrosion-fatigue.

	No.	Pre-corroded/Pristine	Load level [kN]	Frequency [Hz]	σ_{mean} [Mpa]	σ_{min} [Mpa]	σ_{max} [Mpa]	R	Expected fatigue life** (cycles)	Obtained fatigue life (cycles)
Done	1	Pre-corroded	96 (30% MBL*)	2	200	50 (24 kN)	350 (168 kN)	0,14	250.000	107.471
Done	2	Pristine	84 (26,5% MBL*)	2	175	50 (24 kN)	300 (144 kN)	0,16	400.000	396.044

Figure 3.15: Load conditions sample 1 and 2.

During the experiments of sample 1 and 2, a different sensor layout has been used. Figure 3.16 presents the previous sensor layout. 6 sensors were placed in an array and 6 other sensors were placed in the proximity. The sensors that were located closest to the exposed surface are sensors 3 and 4. Their positions correspond to sensors 2 and 3 for the experiment of sample 3.

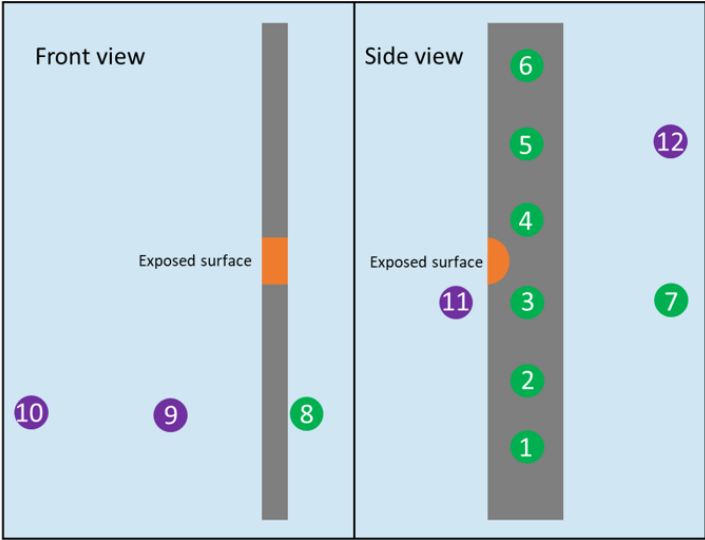


Figure 3.16: Sensor layout used for sample 1 and 2

Results and Discussion

In this chapter, the results of the corrosion-fatigue experiments are presented. First, the applied data processing methods, the contribution of corrosion related acoustic emission and the results of the visual observation of the crack size are addressed. The filtered data of the AE sensors of sample 1,2 and 3 will be analysed. Afterwards, the data of the Hydrophones of sample 3 is analyzed.

4.1. Pre-processing

4.1.1. Filtering of the data

Throughout the corrosion-fatigue experiments millions of events have been recorded by the AE sensors and the hydrophones. Not all the recorded events are equally relevant when analyzing the data. Before starting to analyze the recorded data, some form of pre-processing must be performed to try to eliminate a substantial portion of meaningless noise. Two types of events can be distinguished based on their waveform being, "burst" types and "continuous" types. An example of both signal types is displayed in Figure 4.1.

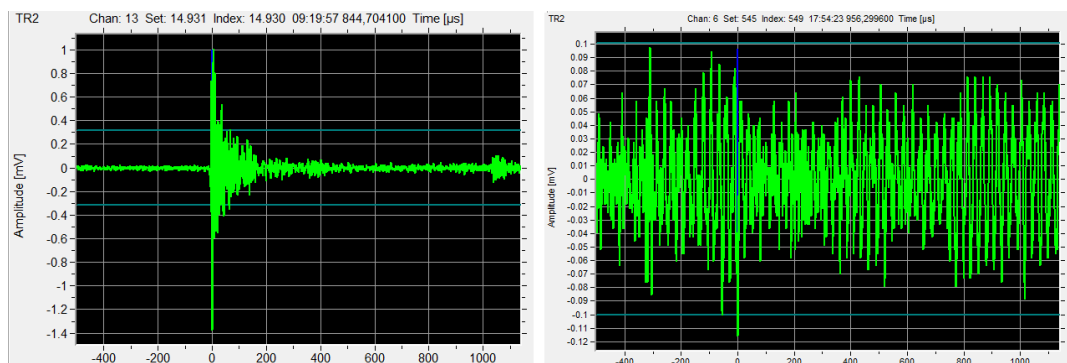


Figure 4.1: Burst type (left) and continuous type (right) signals

Burst signals show strong amplification in front of the signal and a gradual decay until it dies out back to the low amplitude noise. Continuous signals exceed the threshold level of the recording device, but might be generated by coincidence and do not contain relevant information. It is important that the acoustic emission signals that are generated by the damage mechanisms should show at least some significance with respect to the environmental noise. Otherwise it is not possible to distinguish the damage induced signals from the background noise.

SNR Example

A distinction can be made with help of a signal-to-noise (SNR) threshold. This filtering technique can be applied to analyze the waveforms of all the recorded signals and is able to divide all the waveforms

into two groups. A choice can be made on the severity of the applied SNR filter. Figure 4.2 gives a schematic overview on the operation performed by an SNR filter. The figure displays a random hypothetical waveform. The SNR filter approximates the average deviation prior to the maximum deviation of the waveform. In the figure, the assessed noise level is visualized with the orange dashed lines. For this particular waveform the filter estimates a noise level of 1 mV. The gray dotted line represents an SNR filter of 5. That means that the threshold that this waveform must exceed to be characterized as burst type, is 5 times 1 mV = 5 mV. In this case, the peak amplitude of 8 mV exceeds the threshold and, therefore, the signal is considered a burst type.

The strictness of the SNR filter can be specified in advance. For higher magnitudes of the SNR filter, the amount of signals characterised as burst type will decrease. For the example in Figure 4.2, if an SNR filter with a magnitude of 10 would be applied to this waveform, it would be considered a continuous type.

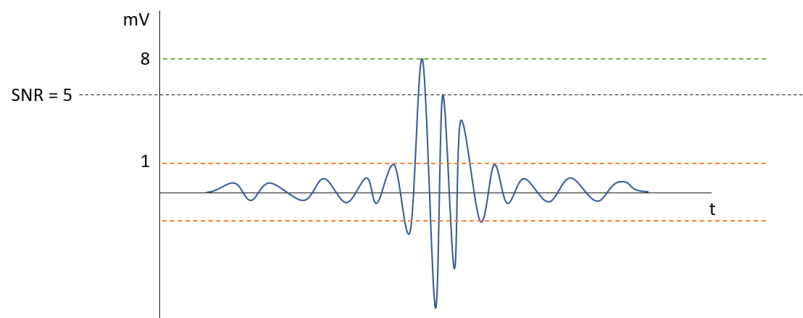


Figure 4.2: Schematic overview of SNR filter.

The influence and effect of the SNR filter will be explained with the recorded data of sample 3. Figure 4.3 presents the peak amplitude of all the recorded hits in the corrosion-fatigue experiment for three different SNR levels. From the figure can be seen that SNR filters eliminate a significant portion of the events. SNR filters have the risk of eliminating potential relevant signals. Therefore, to be cautious, an SNR filter of 5 will be used to continue to data processing.

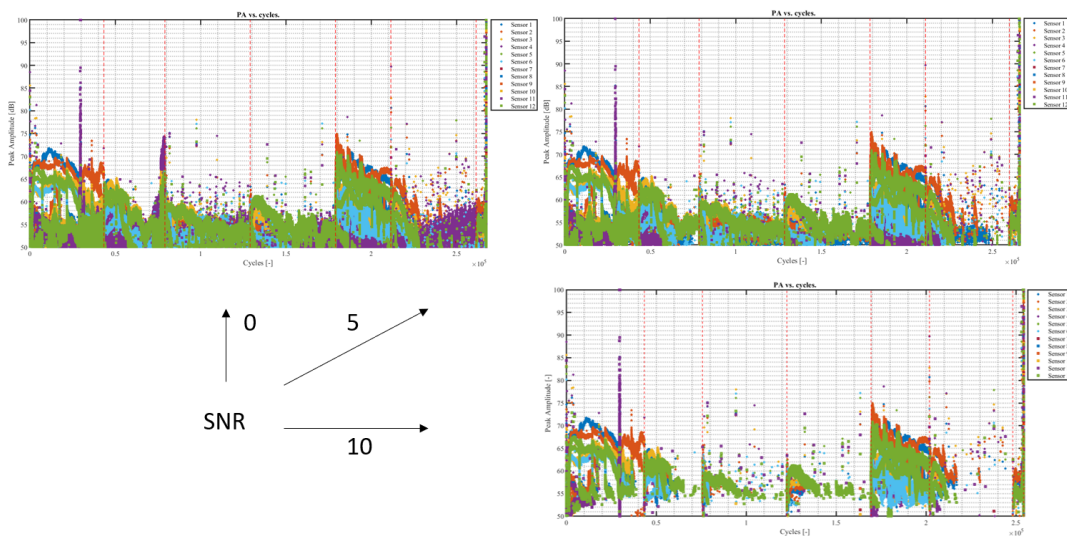


Figure 4.3: Influence of SNR filters.

4.1.2. Corrosion analysis

Pre-corrosion of sample 3

The goal of the pre-corrosion process is to create a weak spot on the dogbone specimen. Sample 3 has been subjected to 100 hours of accelerated corrosion. Figure 4.4 presents the degradation of the exposed surface at three different moments during the process. In the figure can be seen that already after two days, almost the entire exposed surface is covered by corrosion deposits. The figure also shows the change in color of the artificial seawater due to pollution of rust particles. The polluted water decreases the quality of the images.

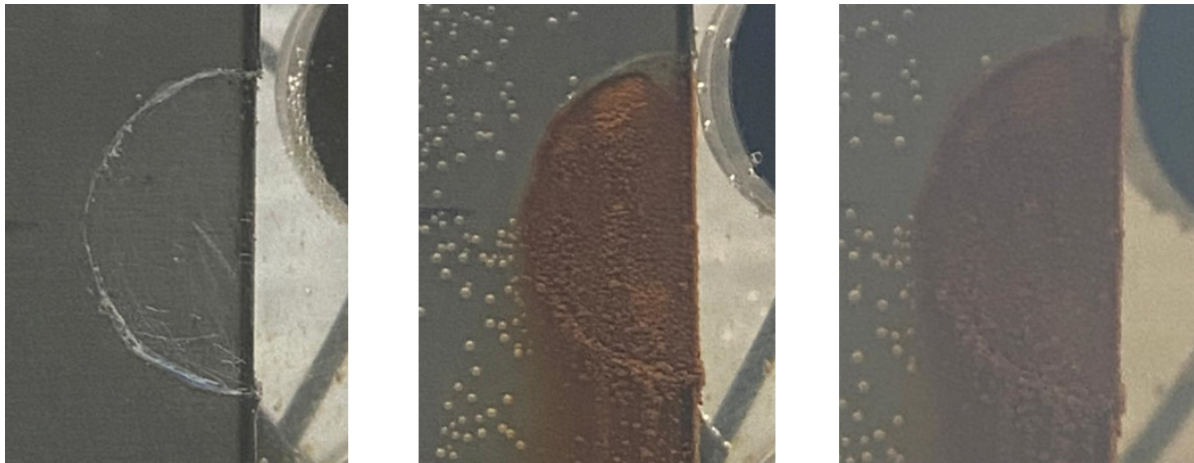


Figure 4.4: Sample 3 after 0 (left), 44 (middle) and 71 (right) hours of corrosion

The pictures of the exposed surface indicate that at several locations, if not at the entire surface, the passive film has ruptured due to aggressive reaction with the abundance of chloride ions present in the artificial seawater. After 100 hours of accelerated corrosion, it is likely that pit initiation has occurred at several locations at the exposed surface. It will be one of these pits that, under cycles stress, will gradually transform into a crack.

For an unnotched dogbone specimen, on a macroscopic level, there are no locations with high geometric variability like sharp corners that lead to increased stress concentration factors. Therefore, it is expected that the crack path will initiate somewhere at the exposed surface at the location of one of the largest pits at the beginning of the fatigue test. The transition area between the exposed surface and the epoxy layer is the expected location where corrosion will occur most severe. The crevice in the interface between the two surfaces is likely to accumulate more severe corrosion than the rest of the exposed surface. It is, therefore, expected to act as the initiation point for the crack to develop. This hypothesis is enforced by the location of crack initiation from sample 1 and 2, as was presented in Figure 3.9.

Analysis of the corrosion induced acoustic emission

In this section the contribution of the corrosion related acoustic emission will be analyzed. The goal of is to find the characteristic features of corrosion-induced emissions.

The corrosion measurements of several stages of the experiment of sample 3 will be investigated. The pre-corrosion was divided into 10 data sets. Additionally, the night measurements during the corrosion-fatigue experiment will also be analyzed.

Figure 4.5 contains four 2 different ways to present the AE data for two threshold settings. During the corrosion only parts of the experiment, the threshold of the DAQ was set to 40 dB. During the simultaneous corrosion-fatigue parts, the threshold was set to 50 dB. Figures B and D thus show a

filtered version of Figures A and C. Figures 4.5.A and 4.5.B shows that the peak amplitude of the hits plotted over the time of one single night of pre-corrosion. The two figures show that the recorded hits are primarily located within 40 to 50 dB and only a small percentage exceeds the threshold of 50 dB. Appendix C contains complementary figures from the pre-corrosion phase.

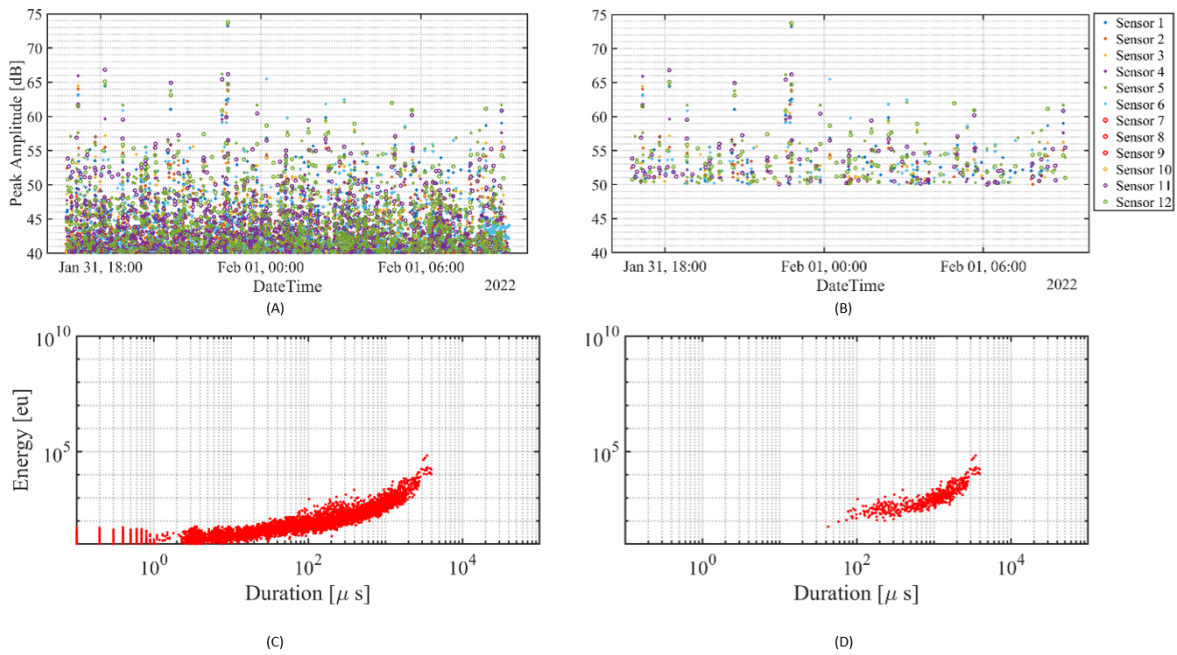


Figure 4.5: Corrosion induced activity during pre-corrosion of sample 3

Figures 4.5.C and 4.5.D display the hits based on the signal parameters energy and duration. These figures will be discussed to further extend in the discussion in section 4.3.

Figure 4.6 shows the calculated hit-rate for all the sensors throughout the pre-corrosion phase of the experiment. In this figure can be seen that the average hit-rate of corrosion-induced AE is between 10^{-2} and 10^{-3} hits per second.

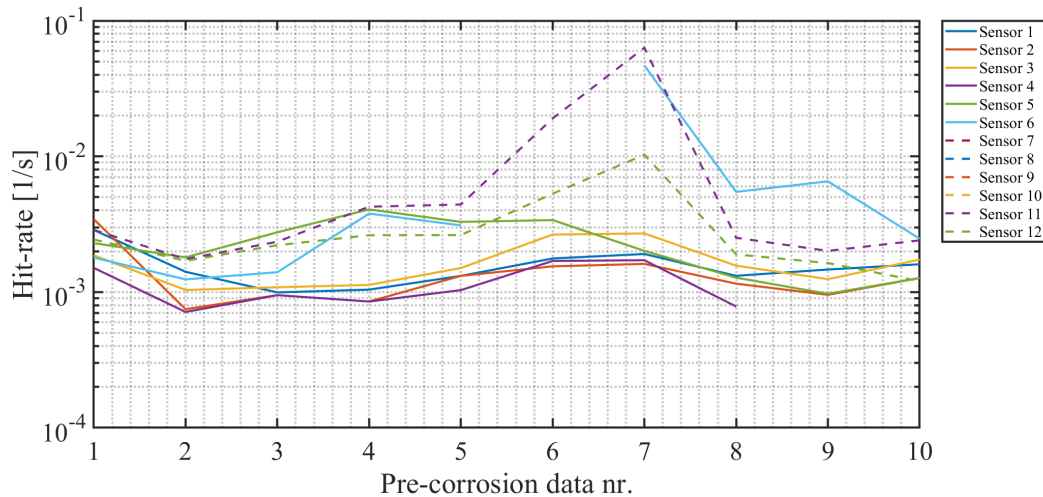


Figure 4.6: Corrosion induced activity during pre-corrosion of sample 3

4.1.3. Crack length measurements

As the monitoring strategy for crack length measurement explained in Chapter 3, two cameras have been used. Over 40 hours of footage and hundreds of pictures have been made to visualize the damage of the specimen. The results will be demonstrated for the continuous video and the periodic photos.

Periodic pictures

Figure 4.7 shows four pictures at different stages of the experiment. From the figure can be seen that the visibility in the tank changes considerably throughout the experiment. The water was polluted by drifting corrosion particles.

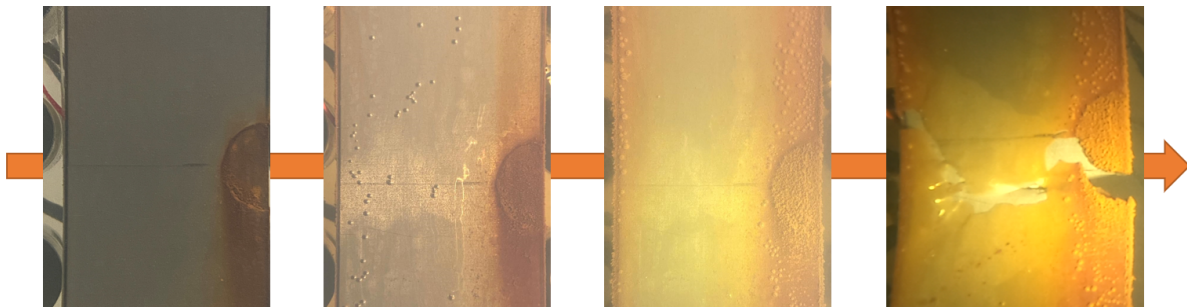


Figure 4.7: Pictures at four different stages of the experiment

Towards the end of the fatigue test of sample 3, the visibility decreased up to a point that an additional light source was required to brighten the exposed surface. Figure 4.8 shows the pictures taken at the final stages before failure. The rightmost figure is taken 6000 load cycles before failure. Meaning that the fatigue life was over 97%. The figures to the left are all 7200 cycles earlier than the figure to the right.

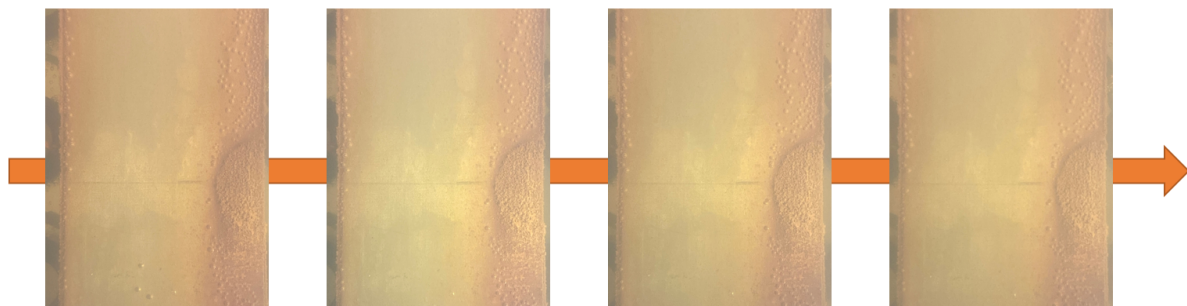


Figure 4.8: Pictures from left to right taken after stage: 38, 39, 40 and 41.

Figure 4.9 shows magnified versions of Figure 4.8 and zooms in on the bottom part of the exposed surface. Due to the difference in lighting and sharpness of the pictures, the crack cannot be seen with the naked eye.

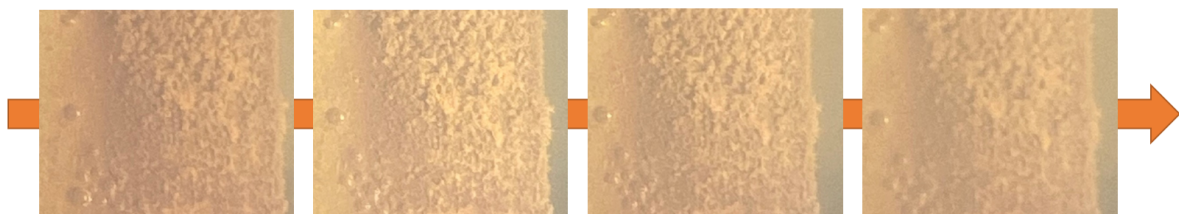


Figure 4.9: Magnification of the location of the crack.

With use of the image processing techniques presented in Chapter 2, the structural changes in the surface could be enhanced. Figure 4.10 shows the processed images for run 39 and 41.

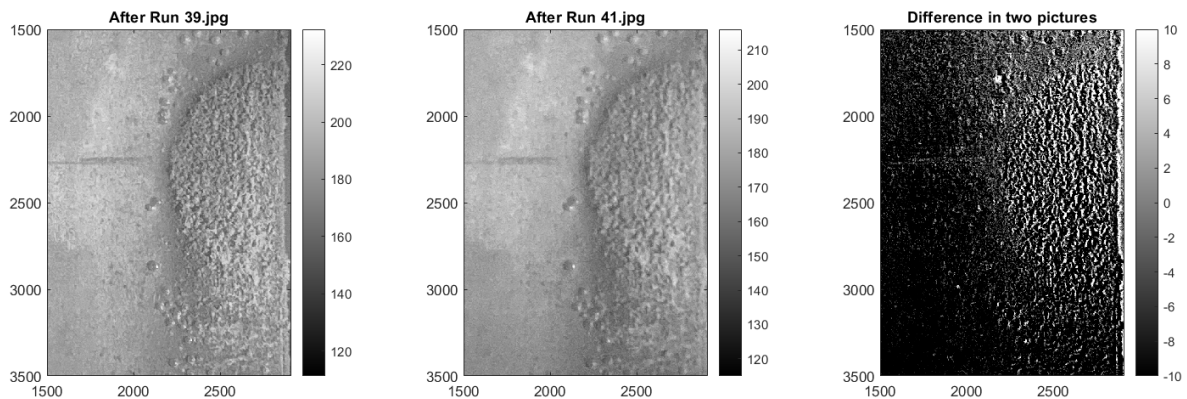


Figure 4.10: Processed images of run 39 and 41.

Unfortunately, even with the added light source, the quality of the pictures taken from outside the water tank got insufficient to accurately identify the crack.

Continuous videos

The footage of the underwater camera provided more satisfactory results than the periodic pictures. The video of the final 6000 cycles contains visible crack propagation. The frame of the video were sampled and aligned using image processing. A video was made that visualizes the propagation of the crack. Figure 4.11 presents four frames that are part of the video that captured the propagation of the fatigue crack in the last cycles before failure.

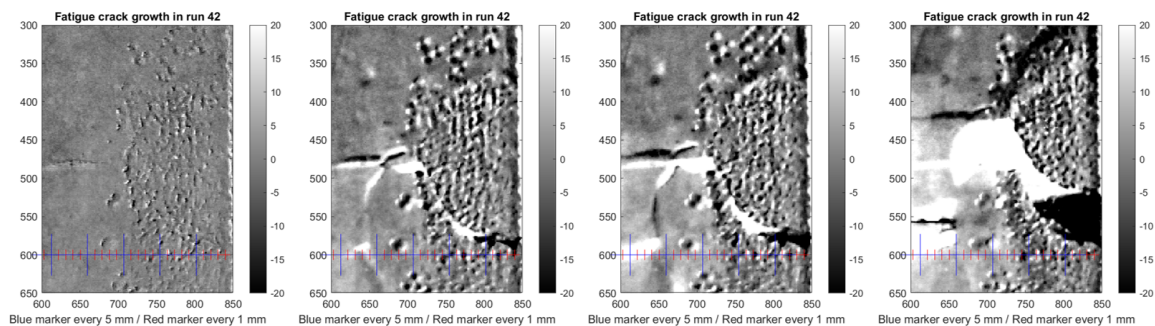


Figure 4.11: Four frames of the crack propagation video.

In Figure 4.11 can be seen that the crack path does not run in a smooth horizontal direction, perpendicular to the applied load. Figure 4.12 shows the crack path of failed sample 3. In this figure can be seen that the protective epoxy layer disbanded from the steel during the test. The crack path of the epoxy layer is not in line with the crack path of the steel. The epoxy layer is in front of the steel crack. This makes it nearly impossible to accurately measure the crack length. Even if the visibility and the quality of the cameras and images was better.



Figure 4.12: Final crack of failed sample 3.

Actions to improve visual observation

If this form of crack length measurement is repeated for a new round of experiments, it is suggested to consider some adjustments to the experimental setup.

- Reconsider the epoxy as protective layer. Perhaps a layer of insulating grease can be used to prevent the steel sample from corroding. This way there will be no hard edges in front of the crack path.
- Maintain high visibility in the water through continuous filtering of the tank. An external filter with a flow of water from and to the tank could prevent pollution from corrosion particles.
- Corrosion deposits attached to the crack path influence the exposure of the crack. From a scientific point of view, the exposed corroded surface should not be interfered with. However, if the priority within the research project shifts towards highly accurate crack length measurement, it should be reconsidered.

4.2. Global Parametric Analysis

The corrosion-fatigue experiment of this thesis has been performed with sample 3. However, the results of the global parametric analysis will be performed in chronological order and will, therefore, start with sample 1. No investigation of sample 1 and 2 has been published yet. First, the definition of the global parametric analysis is explained to manage expectations.

The term **"global"** implies that the analysis takes all the recorded hits into account. The counterpart of a global analysis would be a local parametric analysis of the data. This requires the use of a localization algorithm that determines location of the source of AE events.

The term **"parametric"** denotes the primary features of the waveforms. The traditional primary features of are:

- Peak Amplitude
- Rise-time
- Duration
- Energy
- Counts

The focus of this analysis will depend on the rate of emission of hits, counts and energy, and the combination of energy and duration. Several authors, [24], [27], [28] and [46], have compared the rate of emission of the primary features and concluded that the energy-rate is the parameter that correlates best to the damage evolution. The authors listed above all made use of AE sensors placed directly in contact with the specimens. Using non-contact sensors decreases the reliability of the primary features as explained in Chapter 2. Therefore, in addition to energy-rate, the hit-rate will be investigated, because it is waveform independent and, therefore, less sensitive to changes of the waveform due to convolution.

Full-scale fatigue tests of mooring chains have been monitored with acoustic emission by [35], [36] and [37]. They found that crack induced AE is characterised by high levels of energy and duration, and that noise type signals contained low energy levels. A similar approach is used to distinguish between different recorded signals.

Crack path and selected sensors.

The parametric analysis of sample 1 and 2 will be primarily focused on the recorded hits of sensor 3 and 4. In Figure 3.16 can be seen that these are the sensors directly in front of the crack. If AE signals are emitted from the exposed surface, these are the two sensors that should measure them first. For sample 3, sensor 2 and 3 are directly in front of the crack. Note that the crack path in sample 1 and 3 starts from the bottom of the exposed surface. Whereas the crack path in sample 2 starts at the top of the exposed surface. This is important because the sensor located most closely to the crack is expected to record the highest amount of activity.

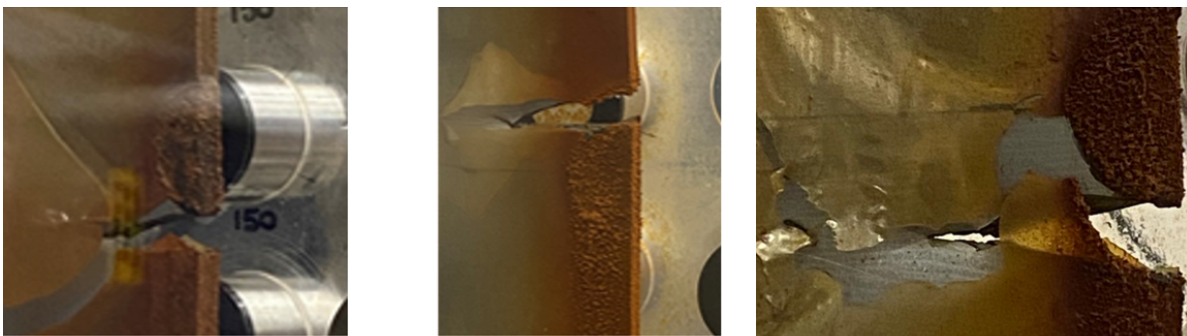


Figure 4.13: Crack path sample 1 (left), sample 2 (middle) and sample 3 (right)

4.2.1. Sample 1

Figure 4.14 presents the peak amplitude of the AE hits recorded during the corrosion-fatigue experiment of sample 1. From the figure can be seen that sensor 3 seems to record a larger amount of activity in comparison to sensor 4. It is also interesting to see that there is barely any activity in the first 50.000 fatigue cycles. It might be that there is acoustic emission in this stage of the fatigue life, but that the magnitude of those signals does not exceed the sensors threshold, or that the hits are eliminated due to the SNR = 5 filter.

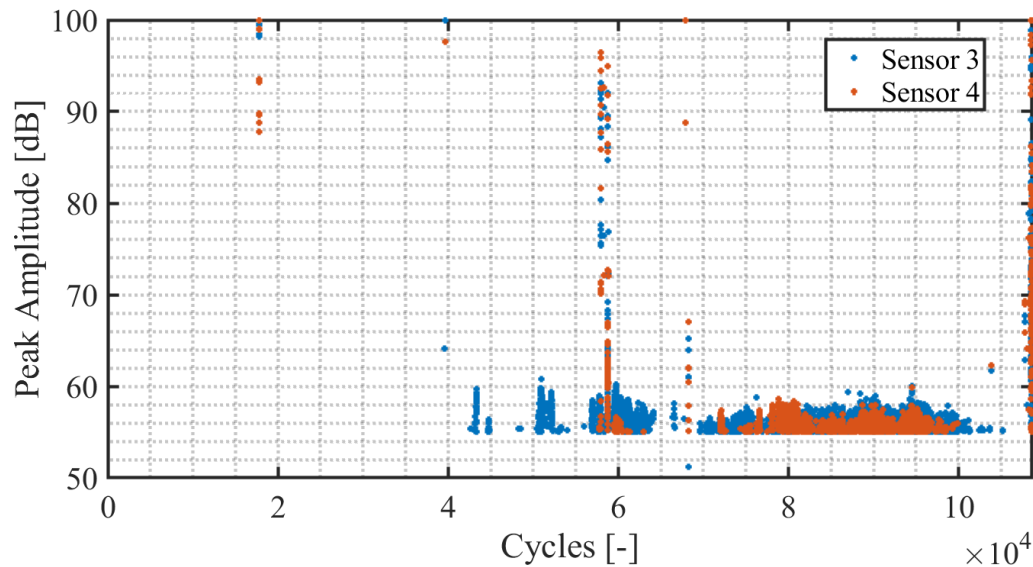


Figure 4.14: Peak Amplitude vs. Cycles. Sample 1

Figure 4.13 shows that crack initiation occurred at the bottom part of the exposed surface. Thus, sensor 3 was located closer to the source of fatigue related AE signals compared to sensor 4. This could be an explanation for the elevated peak amplitude of sensor 3, and hence the hits arriving at sensor 3 would exceed the recording threshold more often.

Figures 4.15, 4.17 and 4.16 give an overview of the rate of acoustic emission throughout the fatigue life of sample 1. Plotting the cumulative of the features can be helpful when performing experiments. From a practical point of view, for operational mooring chains, it is less convenient or simply not possible to monitor the entire lifetime. Therefore, the rate of emission will be investigated to provide more serviceable results for the practical applications.

In the first 50.000 cycles barely any activity is recorded. Between 50.000 and 100.000 cycles the activity and release of energy gradually rises. After 100.000 hits, the activity drops to just before it rises steeply during final fracture.

From the combined hit-rate, count-rate and energy-rate figures can be seen that single hits can have larger influence on the count-rate and energy-rate than on the hit-rate. Around 40.000, a peak in the energy-rate is the consequence of a single hit. Whereas this peak is of no significant height in the figure presenting hit-rate. From Figures 4.17 and 4.16 can be seen that the count-rate and the energy-rate seem scaled versions of each other. This is in line with the work of Yu et al. [24] and Chai et al. [27]. They concluded energy correlated better to damage than count for two reasons. First, the recorded counts strongly depend on the threshold settings. Second, increase in energy-rate can imply either more signals or higher magnitude signals. Whereas an increase in count-rate can also be induced by higher average frequency signals with an equal amount of energy.

It was expected to see the rate of emission grow in magnitude towards the final failure of the specimen. This is observed for the largest part of the fatigue life. However, from the figures is observed that the

recorded activity drops almost back to zero in the final stages of crack growth. An experiment performed with both contact and non-contact sensors could give more insight in the loss of activity when recording with non-contact sensors.

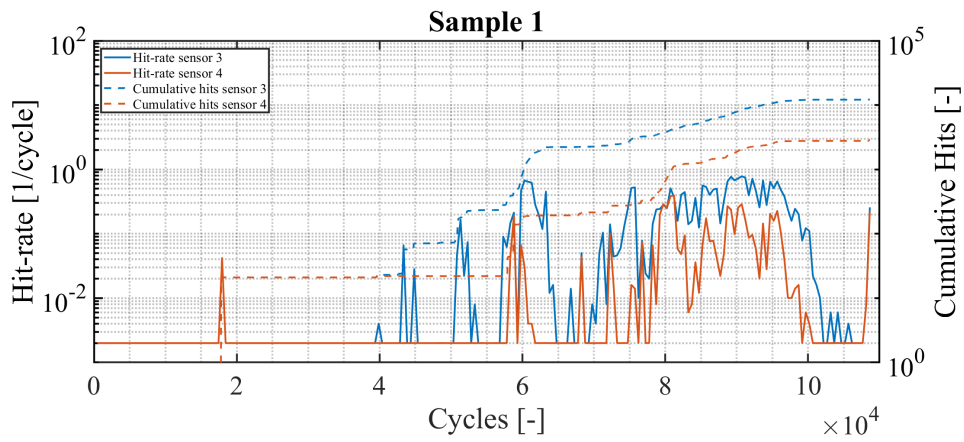


Figure 4.15: Hit-rate Sample 1

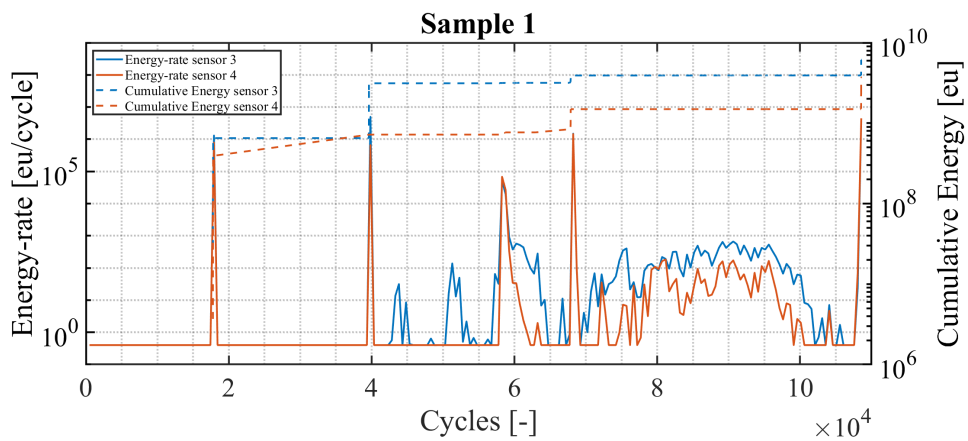


Figure 4.16: Energy-rate Sample 1

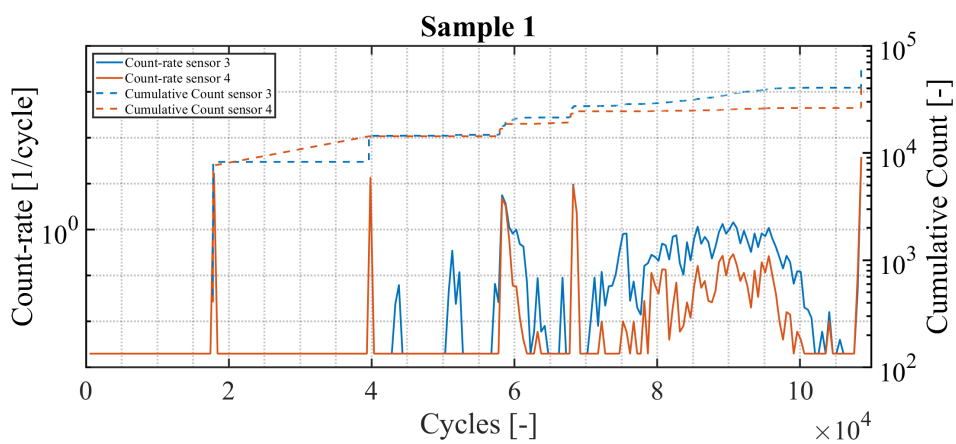


Figure 4.17: Count-rate Sample 1

Energy-Duration distribution

Figure 4.27 presents all the recorded hits of sample 1 in an Energy vs. Duration distribution. Note that in this figure cannot be seen in which point in time the hit is recorded. Angulo et al. [37] suggested that acoustic emission hits can be distinguished based on their energy and duration characteristics. It is believed that the signals induced by the fatigue damage mechanism is characterized by high levels of energy and duration, and noise induced hits are characterized by low energy levels.

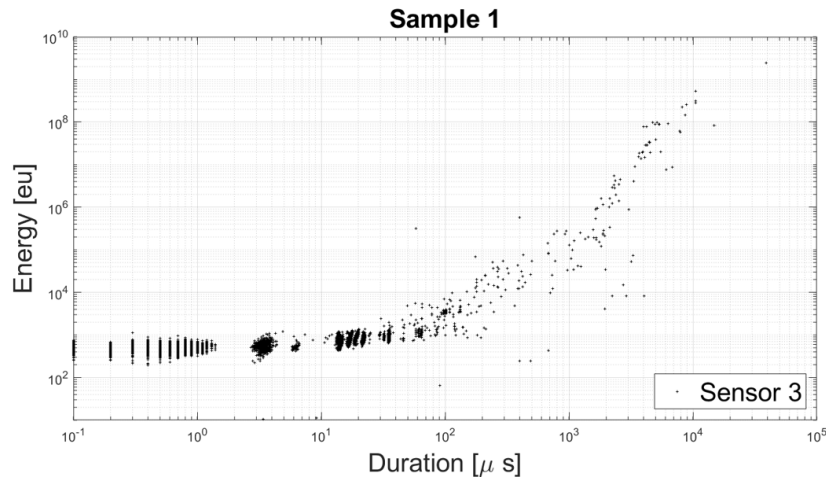


Figure 4.18: Energy-Duration distribution Sample 1

Figure 4.19 shows the same figure as above with added 3 different severity levels based on the signal parameters. The green area consist of signals with a duration below 10 μs and energy levels below 1000 eu. According to literature it can be assumed that such short signals are not characteristic for damage. The yellow area consist of signals with a duration between 10 and 100 μs and energy levels between 1.000 and 10.000 eu. The difference in the threshold for the three severity levels is about one order of magnitude, which is similar to the work of Angulo et al. [37].

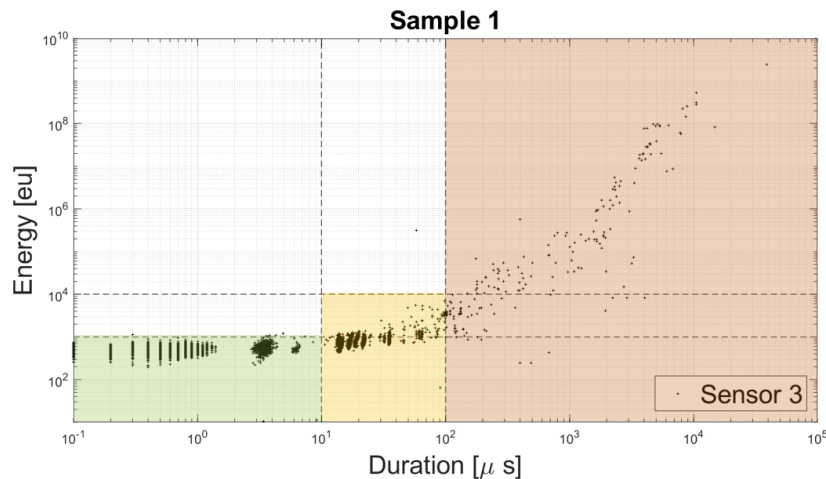


Figure 4.19: Energy-Duration distribution with severity levels

Distinguishing in signal severity is useful because it can be used to extend the analysis of the hit-rate. The hit-rate for the three different severity levels is plotted in Figure 4.20. To obtain this figure, the data is segmented in 256 windows with a window length of 424 load cycles and the amount of hits for each severity level is counted for each window. From the figure can be seen that the relative contribution of the low and medium level signals is similar in the last 30.000 load cycles. The high level signals

appear predominantly at final failure.

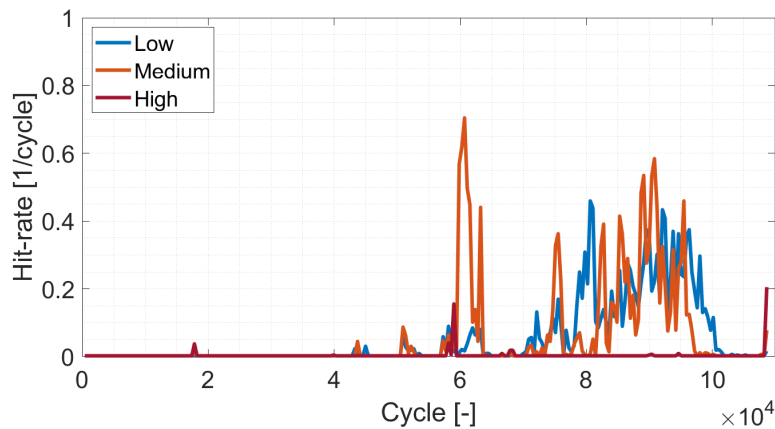


Figure 4.20: Hit-rate severity levels. SNR = 5

SNR substitute

The separation of signals that are taken into account in the three hit-rates could be a potential substitute for the SNR filter. Figure 4.21 shows the hit-rate for the three severity levels for the unfiltered data. In this figure can be seen that in the final 10.000 hits before failure only signals are recorded with low signal parameters.

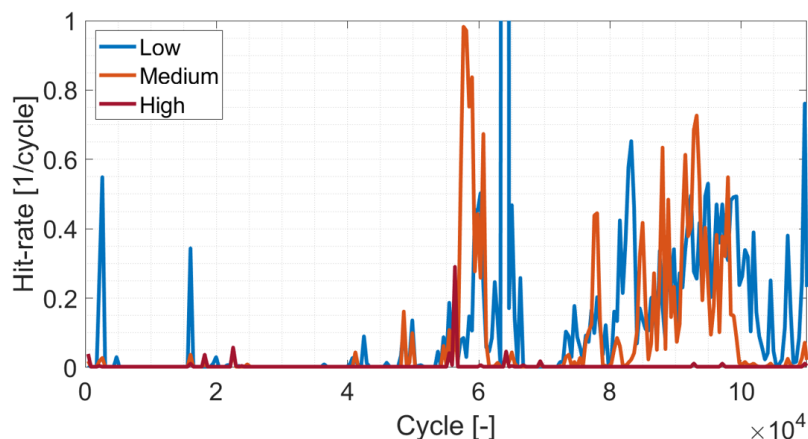


Figure 4.21: Hit-rate severity levels. SNR = 0

Comparison to other sensors

Figures 4.22 and 4.23 show the hit-rate for sensors 3, 4, 5 and 6. Sensors 5 and 6 are located directly above sensors 3 and recorded more medium level hits towards the end of the experiment than sensor 3. By looking at the unfiltered data of Figure 4.22, it is observed that sensor 4, 5 and 6 all record more activity than sensor 3, even though they are located further away from the location of the crack. This is not in line with expectations, as sensor 3, being closer to the source of the fatigue-induced hits, should record the most signals and with the highest energy levels. Given that this is not observed, this suggests that, at least a substantial part of the recorded hits does not originate from the crack.

For the filtered data in Figure 4.23, the same behaviour is observed. Sensor 5 and 6 have recorded higher energy levels and more hits than sensor 3. Without prior knowledge of the location of the source of the fatigue-induced hits, a global analysis of the hits would aim in the wrong direction, as it would be expected that sensor 5, and not sensor 3, is located the closest to the crack.

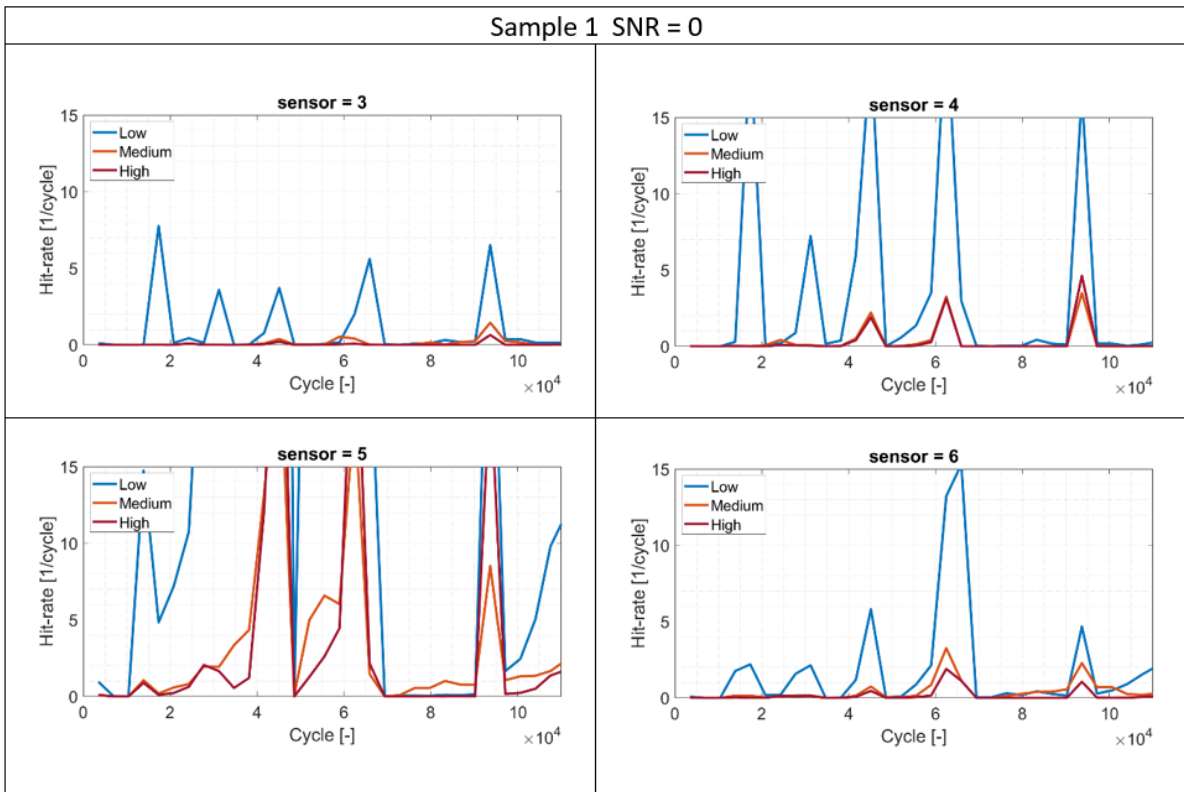


Figure 4.22: Hit-rate severity levels SNR = 0

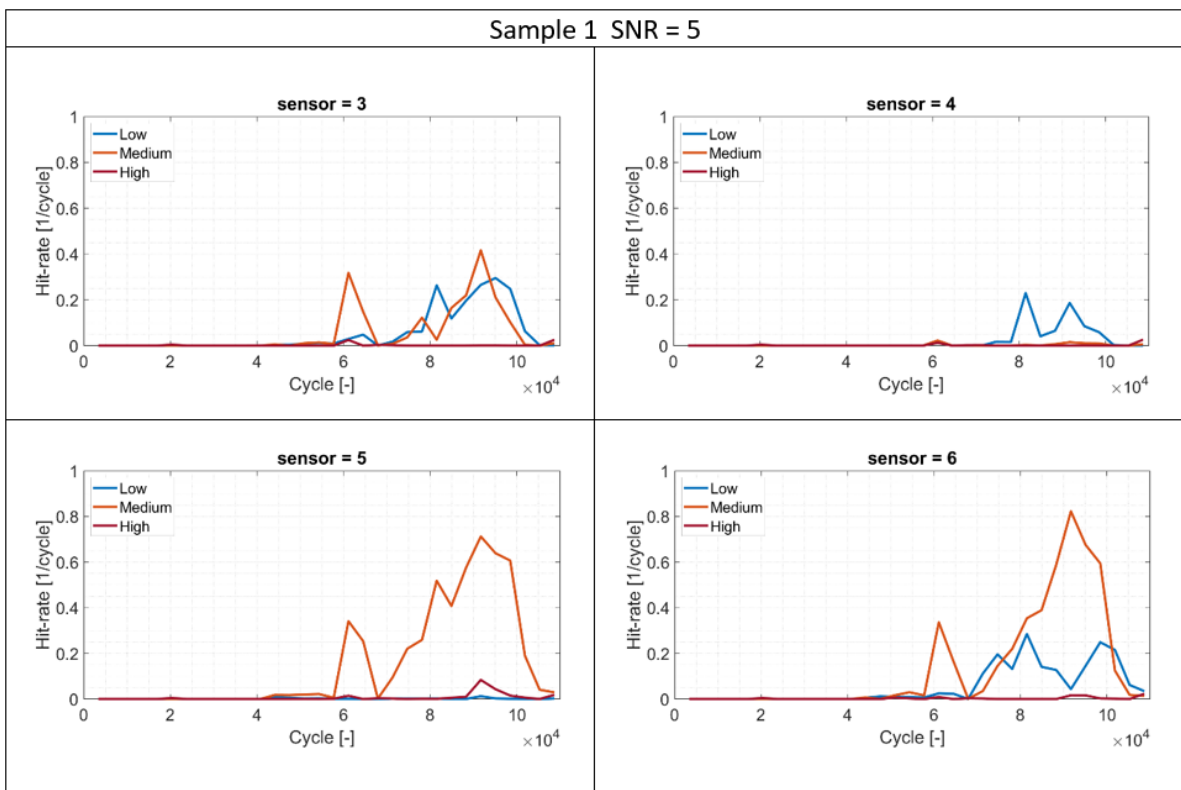


Figure 4.23: Hit-rate severity levels SNR = 5

4.2.2. Sample 2

Figure 4.24 presents the peak amplitude of the AE hits recorded during the corrosion-fatigue experiment of sample 2. Figure 4.13 shows that, for sample 2, crack initiation started at the top part of the exposed surface. Therefore, sensor 4 was located closer to the source of fatigue related AE signals. Sample 2 was not pre-corroded in advance to the fatigue test. This explains why the fatigue life of sample 2 is four times as that of sample 1.

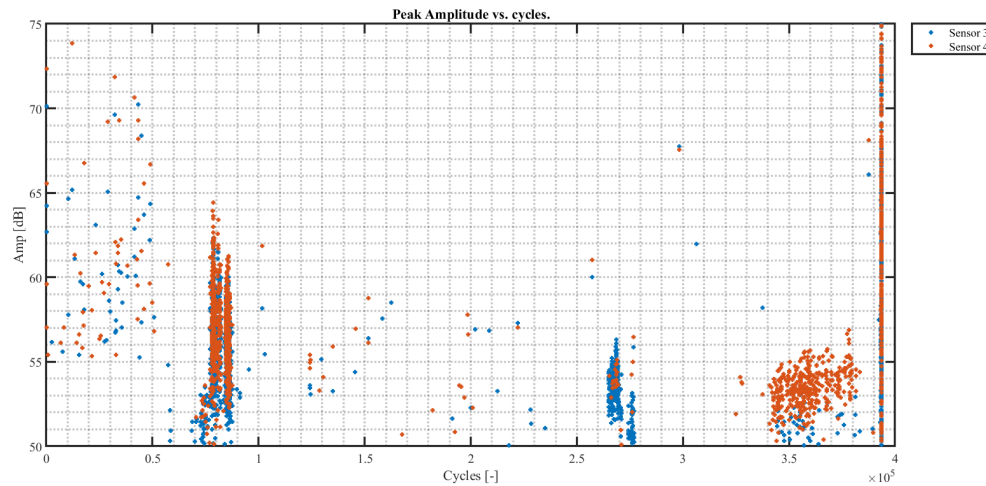


Figure 4.24: Sample 2. Peak Amplitude vs. Cycles. SNR = 5.

Sensor 3 and 4 recorded more activity in the experiment than only in the final stages of the fatigue life. They both recorded strokes of activity around 80.000 cycles and around 270.000 cycles. This activity was also captured by the majority of the other sensors. From a fatigue perspective, it is difficult to find an explanation for these moments of increased activity and release of energy. When using a local analysis with localization implemented, it can be investigated where the source of these hits is positioned. By doing, these strokes could be ruled out of the data.

In Figures 4.25 and 4.26, the rate of emission for energy and hits are presented. These figures enhance the differences in recorded activity for sensor 3 and 4. By looking at the combination of these figures, several moments in the experiments can be identified with increased rate of emission for hits and energy. For example, based on these two parameters, it is difficult to distinguish between the events occurring around 80.000 cycles and 270.000 cycles. In Figure 4.25 can be seen that the hit-rate of sensor 4 increases to a, more or less, stable rate towards the end of the fatigue life.

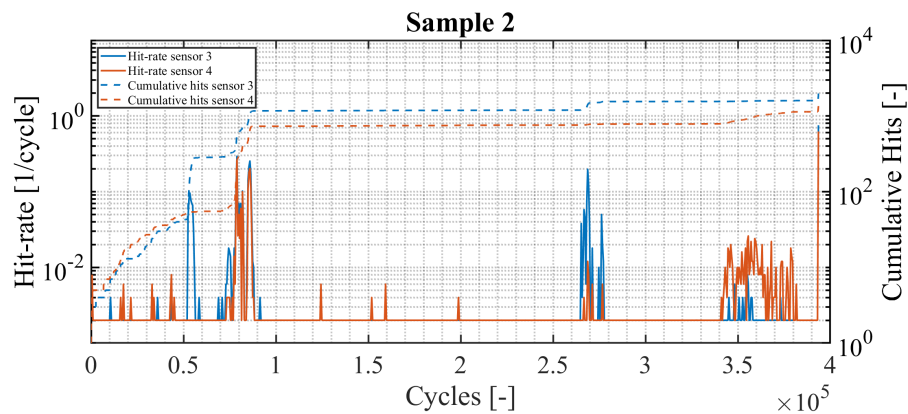


Figure 4.25: Hit-rate Sample 2

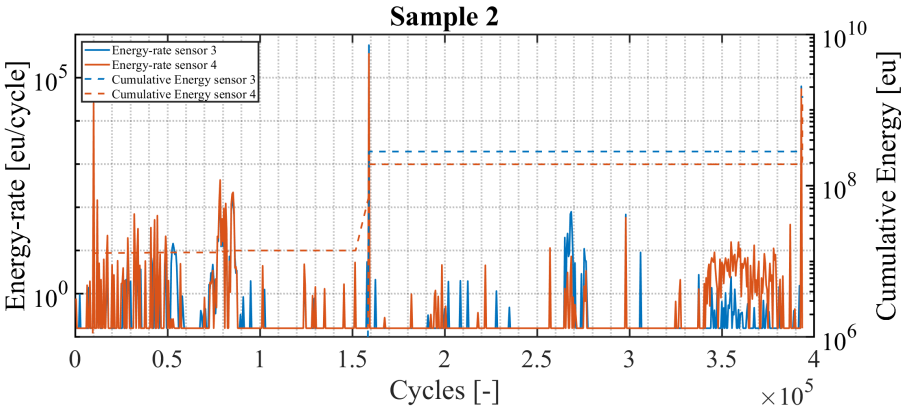


Figure 4.26: Energy-rate Sample 2

Energy-Duration distribution

Figure 4.27 presents all the recorded hits of sample 2 in an Energy vs. Duration distribution. The threshold during the measurement of sample 2 was set at 50 dB, instead of 55 dB during sample 1. Therefore, the limits for the three severity levels were raised to 50 and 200 μ s and 3.000 and 30.000 eu.

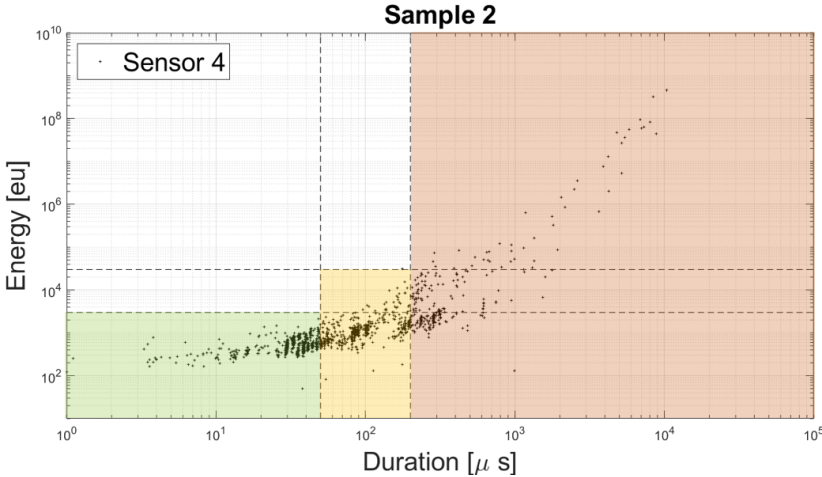


Figure 4.27: Energy-Duration distribution Sample 2

Figure 4.28 shows the hit-rate for the three different severity levels. There are both low and medium level signals recorded in the 50.000 cycles towards the end of the experiment. The high level signals were only captured at the final fracture of the specimen and in early stages of the test around 80.000 cycles.

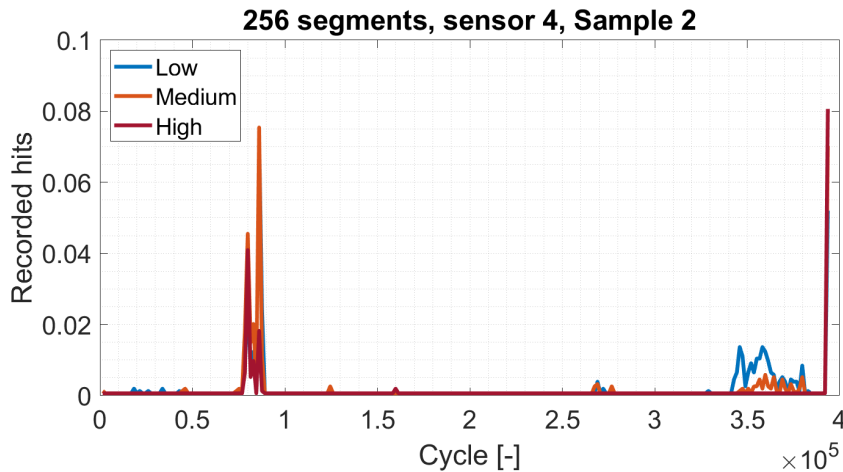


Figure 4.28: Hit-rate Sample 2

SNR substitute

For sample 2, it will also be investigated if the difference in severity level can be a substitute for the SNR filter. Figure 4.21 shows the hit-rate for the three severity levels for the unfiltered data of sample 2. A relatively large window size has been used due to the high computational time of the analysis. In this figure can be seen that the hit-rate for all three levels is increasing towards the end of the experiment. From the vertical axis can be seen that the hit-rate for the unfiltered data is two orders of magnitude higher than the hit-rate for the SNR = 5 filtered data from Figure 4.28. This exemplifies how many signals have been eliminated by the SNR filter.

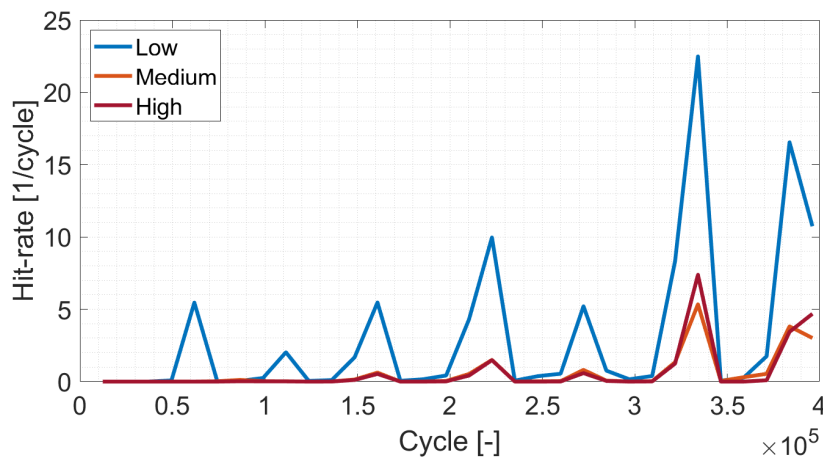


Figure 4.29: Hit-rate Sample 2, SNR = 0

Comparison to other sensors

Figure 4.30 shows the hit-rate for sensors 3, 4, 5 and 6 for the unfiltered data. In this figure is observed that sensor 5 has recorded significantly more low, medium and high level signals than sensor 4, which was located closer to the crack. It is also observed that the behaviour of the hit-rate of all three severity levels is rising towards the end of the fatigue test. Without prior knowledge of the location of the crack, a global analysis without SNR filter would lead to the wrong conclusions on source location.

After applying an SNR = 5 filter, over 99% of the hits from sensors 4 and 5 are eliminated. The remaining hits are recorded during the final stages of the fatigue life, except for some events around 80.000 cycles. From a fatigue-theoretical point of view, it is unlikely that these events are generated by the fatigue damage mechanisms. A visual observation at 100.000 cycles confirmed that there was no

visible crack formation at that moment in time.

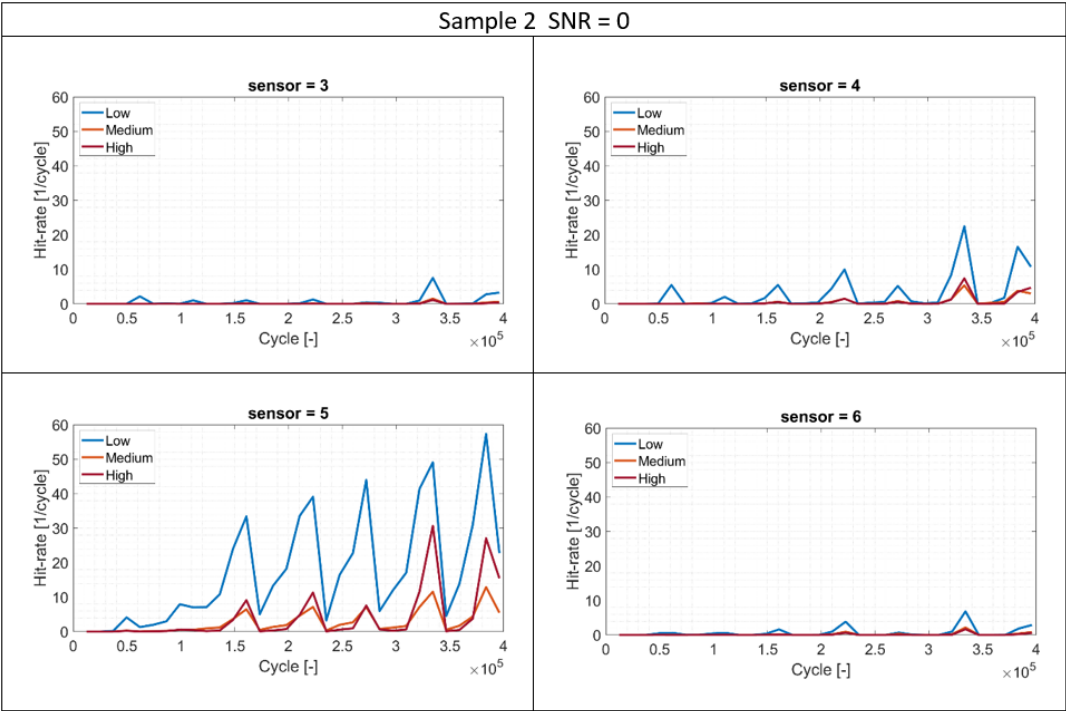


Figure 4.30: Hit-rate severity levels SNR = 0

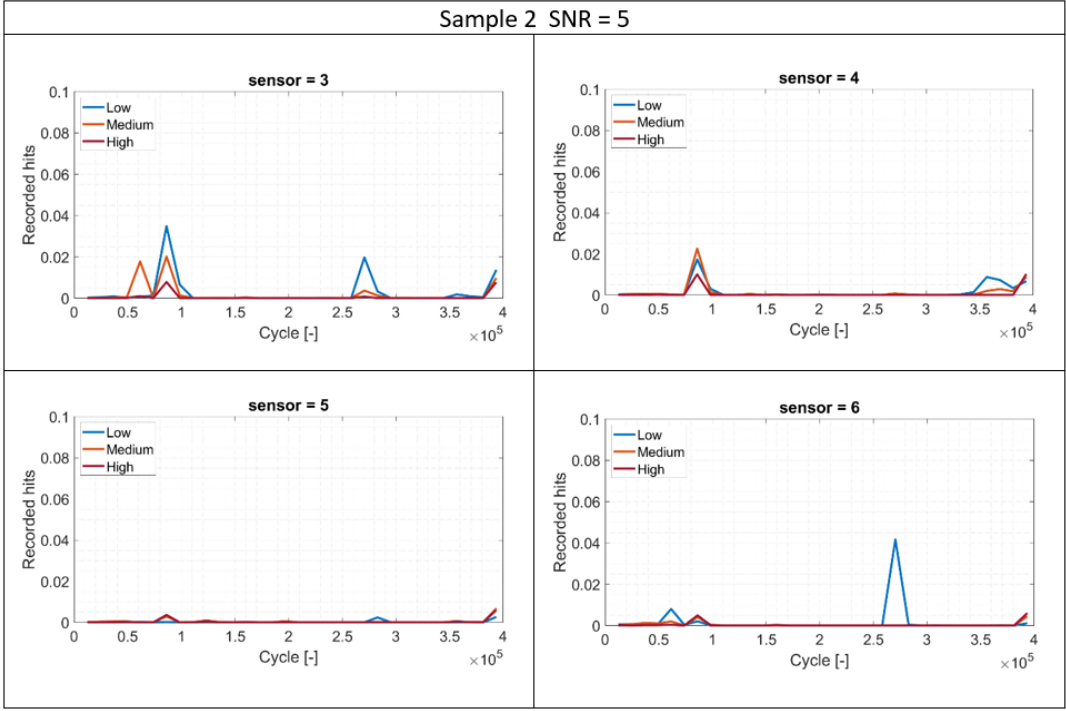


Figure 4.31: Hit-rate severity levels SNR = 5

4.2.3. Sample 3

The sensor layout used during the experiment was presented in Figure 3.12. As can be seen in Figure 4.13, the crack path for sample 3 started at the bottom of the exposed surface. This means that sensor 2, 3, 5 and 12 are located the closest to the source of fatigue induced acoustic emission. For convenience when comparing to the other two samples, the acoustic emission analysis of sample 3 is based on sensors 2 and 3, which correspond to sensor 3 and 4 for sample 1 and 2. The experiment was performed in seven days. The start of each new day is indicated with the red vertical dashed lines.

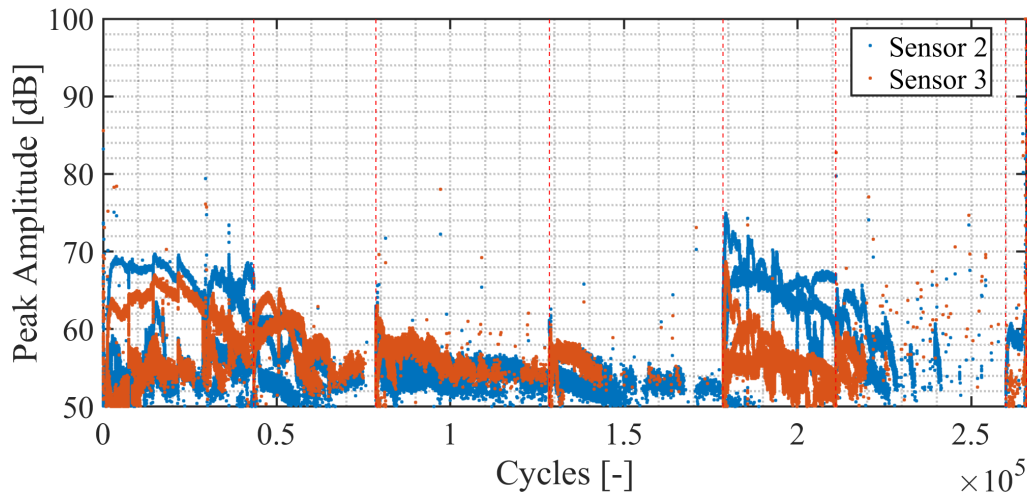


Figure 4.32: Peak Amplitude vs. Cycles sample 3

Figure 4.32 presents the peak amplitude over the cycles for AE sensors 2 and 3. Large amounts of hits are being recorded since the start of the fatigue test and is unusually high compared to the recordings of sample 1 and 2. When zooming in on the data, it is observed that there is recurring behaviour at the same frequency as the load frequency of 2 Hz. Based on the peak amplitude no differences between the behaviour in day 1 and day 5 can be observed. The other primary features have been reviewed, but gave no clear distinction between the different stages of the experiment because their behaviour displays the same trends as the Peak Amplitude.

The hit-rate for sensor 2 and 3 is visualized in Figure 4.33. The figure shows that, for the majority of the experiment, both sensors measure the same amount of activity. Over the entire experiment sensor 2 measured slightly more activity. It was expected to see an increase in activity towards the end of the fatigue life. However, the hit-rate in the final stage of the fatigue life is not higher than in other stages of the fatigue life. In day 7 the hit-rate barely exceeds an average of 1 hit per cycle. Whereas in other stages of the experiment, the hit-rate increased to an average of 3 to 4 hits per cycle.

Another remarkable aspect of the hit-rate is that it seems to decrease towards the end of the experiment. Day 6 contains very little activity compared to days 1 to 5. The absence of activity between 220.000 and 260.000 cycles in line with expectations. The hit-rate is expected to increase with increased damage evolution as was observed in sample 1 and 2. It is possible that the trends influenced by damage evolution are masked behind the abundance of AE hits recorded during the experiment. Further local analysis is required to draw more resolute conclusions.

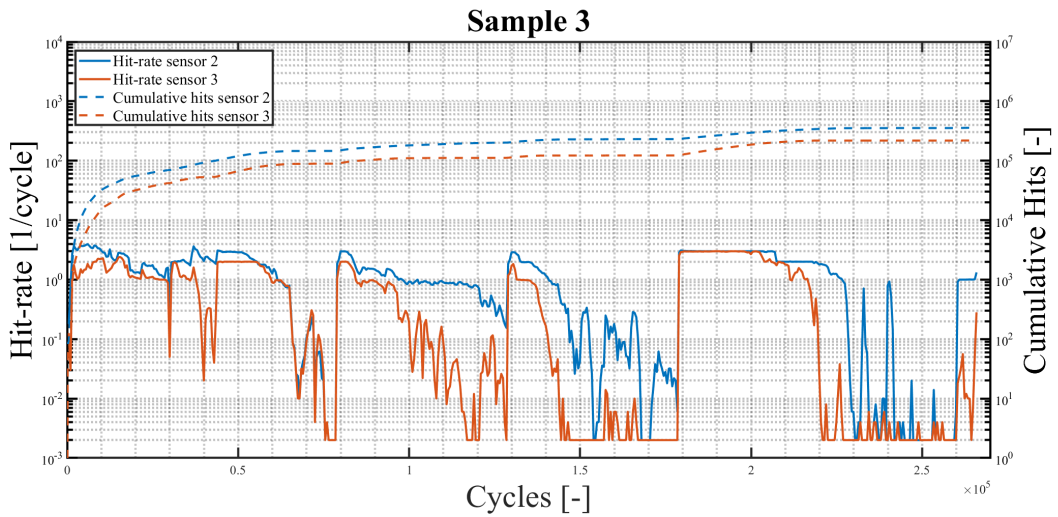


Figure 4.33: Hit-rate sample 3

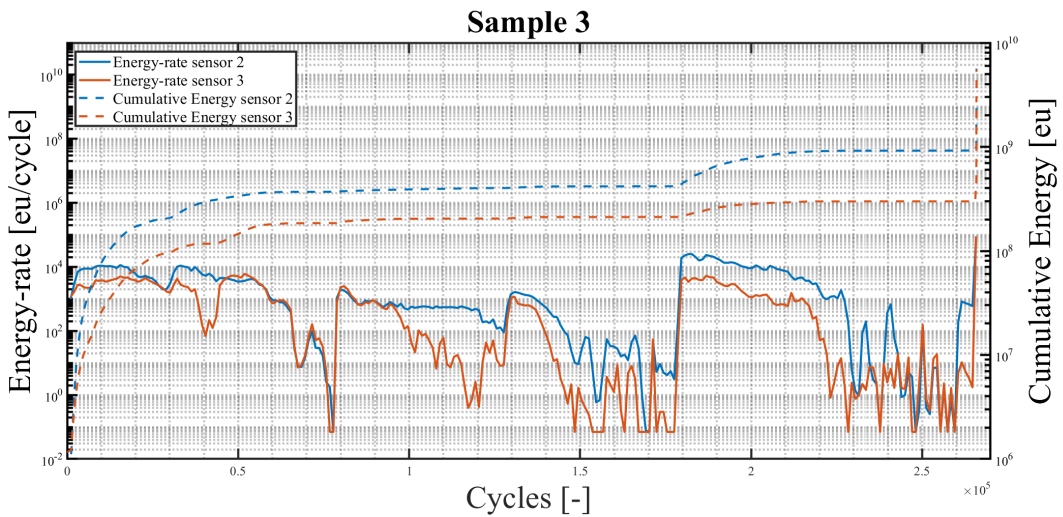


Figure 4.34: Energy-rate sample 3

Based on the analysis of the signal parameters of the hits recorded by the acoustic emission sensors, it is difficult to identify the warning signs before failure occurs. It was expected to see an increase in hit-rate and energy-rate in the stage preceding final fracture. However, different behaviour of what is expected is presented by the data. In the time leading up to stable crack growth, day 6, there is a decrease in hit-rate and energy-rate. When regarding the combination of the hit-rate and energy-rate measured for sample 3, it is difficult to distinguish between the different stages of crack growth. No clear moments of crack initiation or propagation could be identified. The characteristic features of stable crack growth in day 7 do not significantly stand out in comparison to other stages throughout the experiment.

The results of sample 3 do not necessarily diminish the correlation of hit-rate and energy-rate to the fatigue damage evolution. It is likely that the fatigue induced AE is overwhelmed and suppressed by an additional AE noise source.

Energy-Duration distribution

Figure 4.35 presents all the recorded hits of sample 2 in an Energy vs. Duration distribution. The threshold during the measurement of sample 3 is the same as sample 2. Therefore, the same limits

are applied. The distribution of the signals shows the same trends as sample 1 and 2. It does contain considerable more hits than have been recorded in the first two samples.

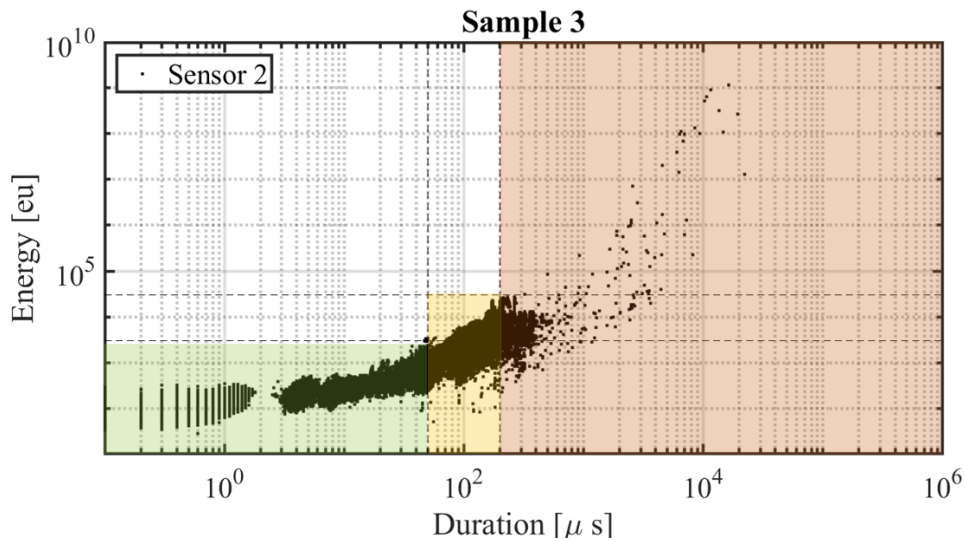


Figure 4.35: Energy-Duration distribution Sample 3

Figure 4.36 shows the hit-rate for the three different severity levels. In this figure can be seen that the relative contribution of the three levels of severity varies in random ways throughout the experiments. This reinforces the assumption that there is an external source emitting signals in the water tank.

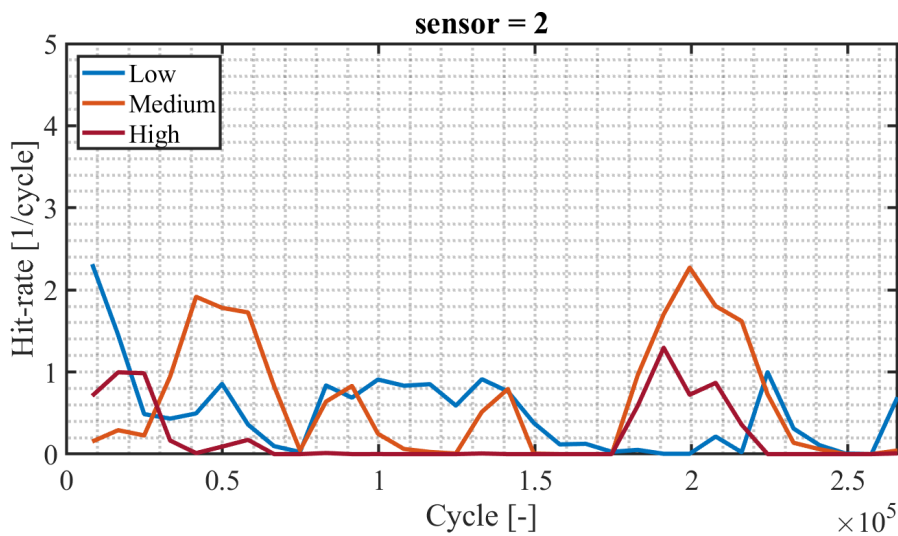


Figure 4.36: Hit-rate Sample 3

SNR substitute

For sample 2 will also be investigated if the difference in severity level can be a substitute for the SNR filter. Figure 4.37 shows the hit-rate for the three severity levels for the unfiltered data of sample 2. A relatively large window size has been used due to the high computational time of the analysis. In this figure can be seen that the hit-rate for all three levels is increasing towards the end of the experiment. From the vertical axis can be seen that the hit-rate for the unfiltered data is two orders of magnitude higher than the hit-rate for the SNR = 5 filtered data from Figure 4.28.

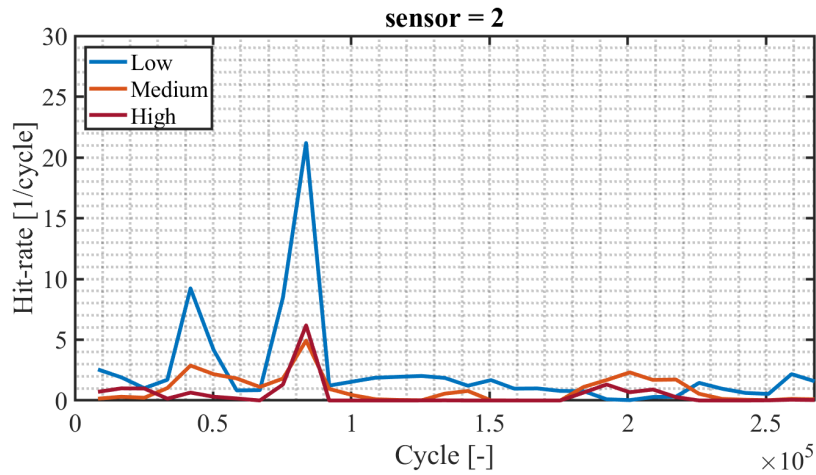


Figure 4.37: Hit-rate Sample 3, SNR = 0

Comparison to other sensors

Figures 4.38 and 4.39 show the hit-rate for sensors 2, 3, 5 and 12. There is no increase in hit-rate observed towards the end of the fatigue life for both the filtered and unfiltered data. The activity is similar in various stages in the experiment. The assumed presence of external AE signals makes it impossible to see the development of corrosion-fatigue damage evolution, when analyzing the data with a global analysis.

Fortunately, it observed that for both the filtered and unfiltered data, that large portions of the activity is recorded by all four sensors. This is very helpful when extending and improving the global analysis to a local analysis. Because at least three sensors are required to pinpoint the location of the emitting source.

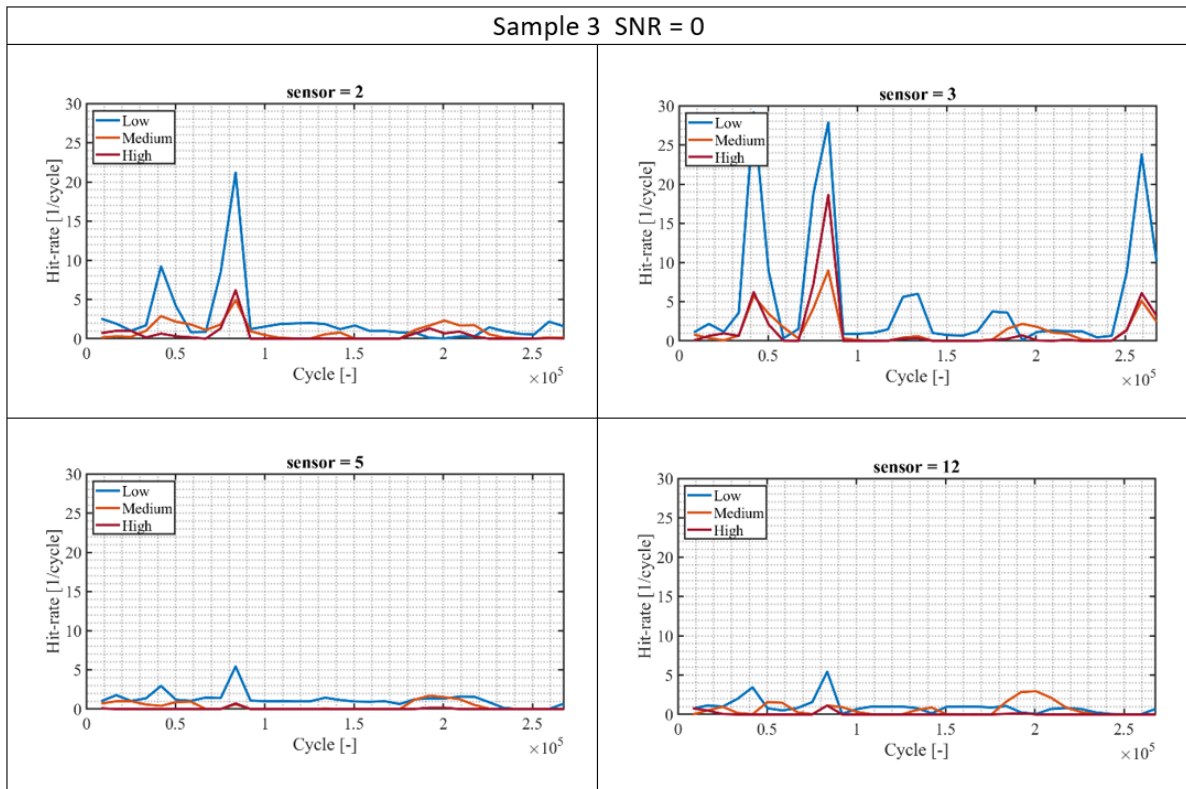


Figure 4.38: Hit-rate severity levels SNR = 0

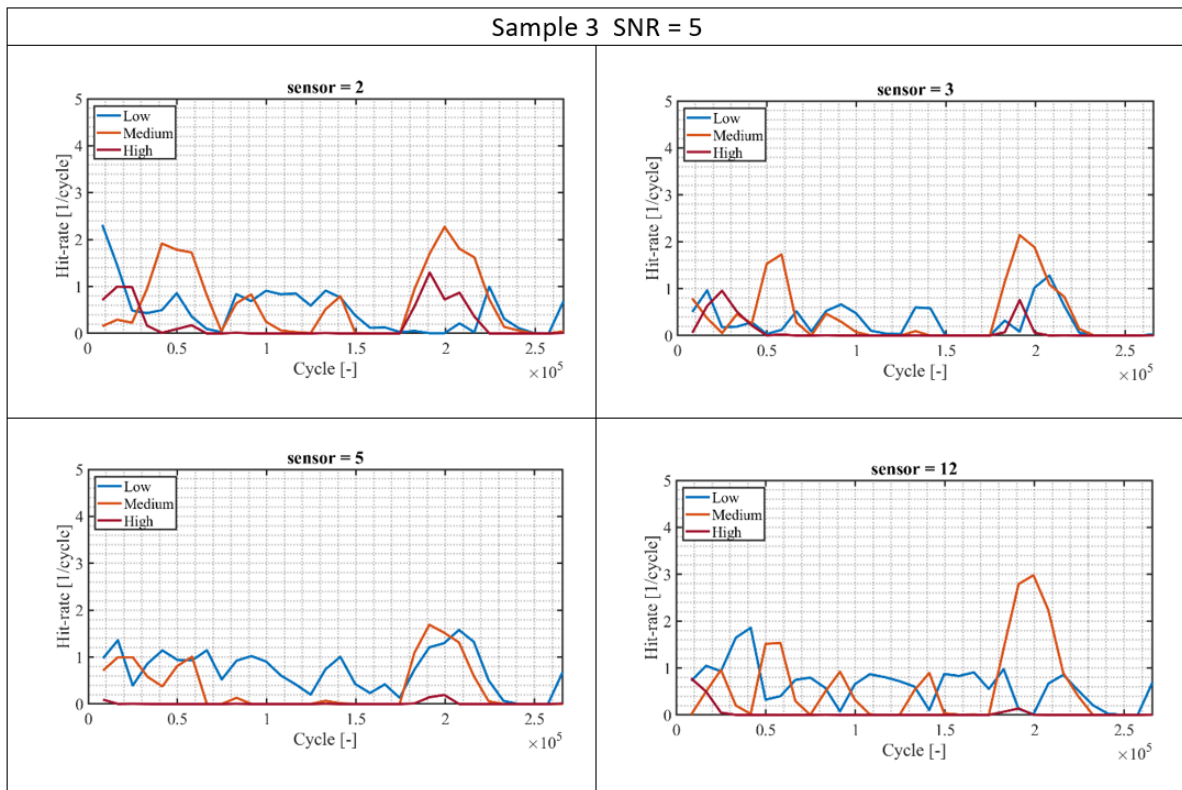


Figure 4.39: Hit-rate severity levels SNR = 5

Hydrophones

In addition to the Vallen AE sensors, custom made hydrophones have been used to measure the emitted signals during the experiment. In this section, the results of the hydrophones are presented. At the end of this section the comparison between the results of both sensor types will be made.

Figure 4.40 displays the peak amplitude over the cycles for the recorded hits during the corrosion-fatigue experiment. In this figure can be seen that the magnitude of the hits captured by the hydrophones is much higher than the AE sensors. Several values for the threshold level have been tested throughout the experiment to find a steady balance between sufficient hits, but without gathering too much irrelevant noise.

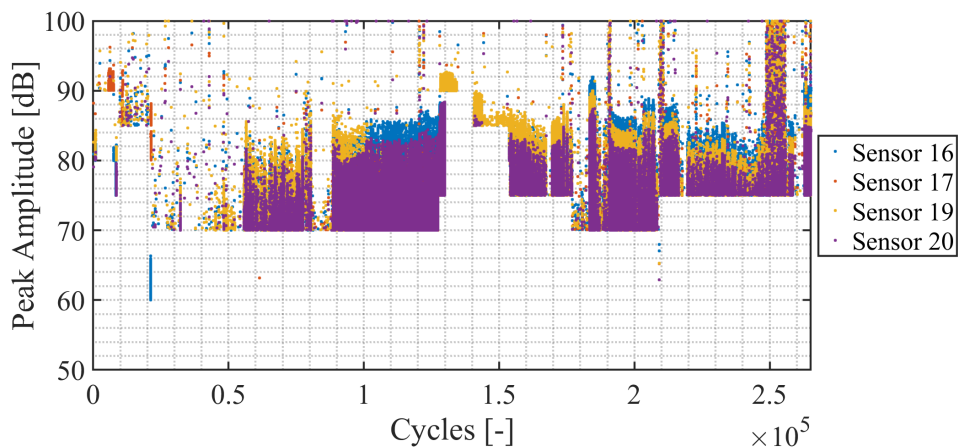


Figure 4.40: Peak Amplitude vs. Cycles.

From the amount of hits recorded by the hydrophones can be stated that these sensors are very sen-

sitive. After applying an SNR filter = 5, a substantial amount of hits is eliminated. Figure 4.41 presents the peak amplitude over the cycles for the SNR = 5 filtered hydrophone data.

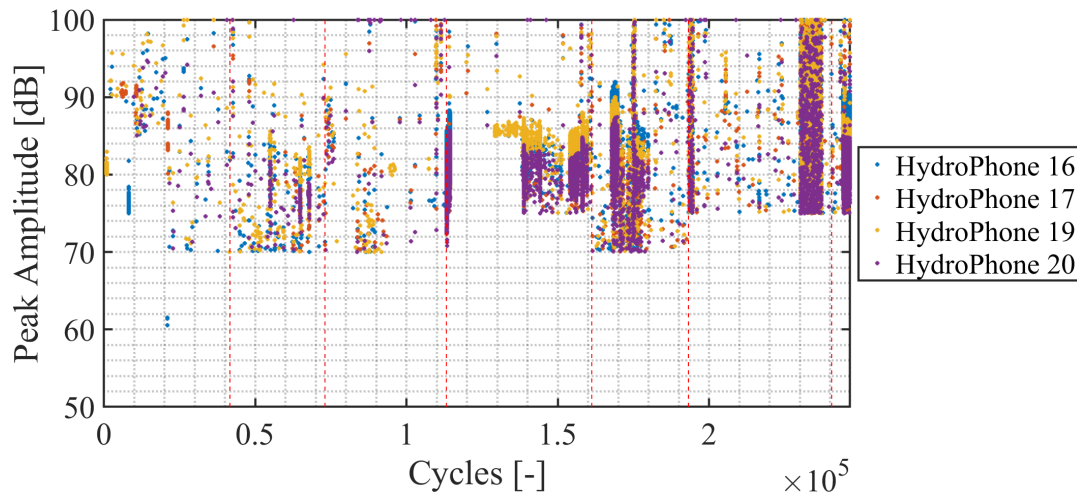


Figure 4.41: Peak Amplitude vs. Cycles. SNR = 5.

The difference in applied threshold level throughout the experiment makes it difficult to accurately assess these figures, but it looks like the amount of hits is increasing with certain spikes towards the end of the fatigue life. The rate of emission for the four hydrophones can give some additional insight and is presented in Figure 4.42.

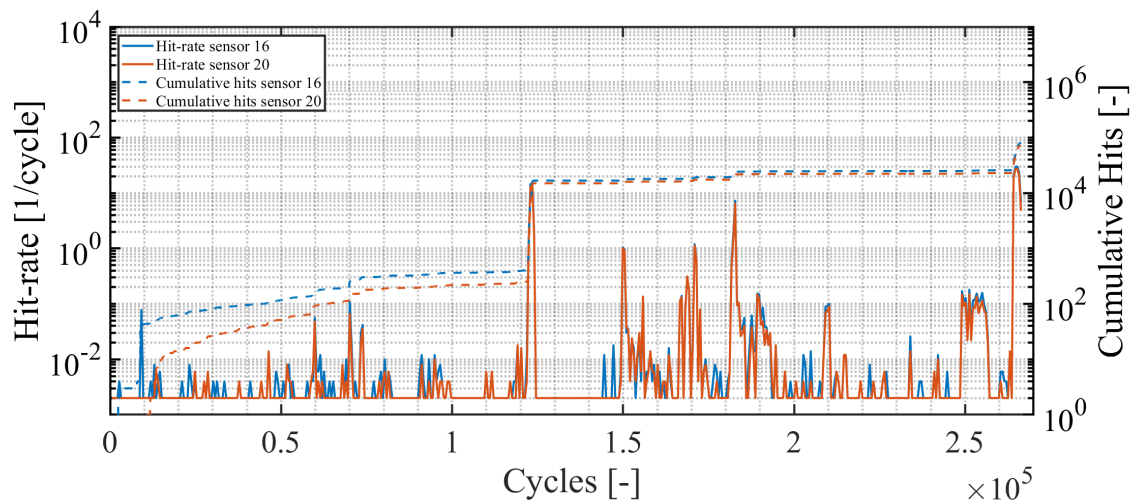


Figure 4.42: Hydrophone hit-rate sample 3

Figure 4.42 shows the hit-rate recorded by hydrophone 16 and 20. After the first significant peak around 115.000 cycles, the hydrophones started to record an extreme amount of activity. For size of the data was becoming so large that the threshold for all the sensors was lifted to the point where almost no more hits were recorded. This explains the moment of zero activity around 120.000 to 130.000 cycles. Figure 4.43 shows the energy-rate of the hydrophones. In the figure, there are three windows exceeding the 10^9 limit. There are no evident trends in the preceding cycles leading up to these peaks that can distinguish the peak of final failure from the other two.

What can be seen is that in several stages towards the end of the experiment, the hit-rate and energy-rate are increased. Unfortunately, these stages are also preceded and followed by stages of negligible

activity. No concise trends were observed based on the hydrophone measurements. It must be taken into account that these custom made hydrophones are prototypes and that the quality of the measurements is not verified.

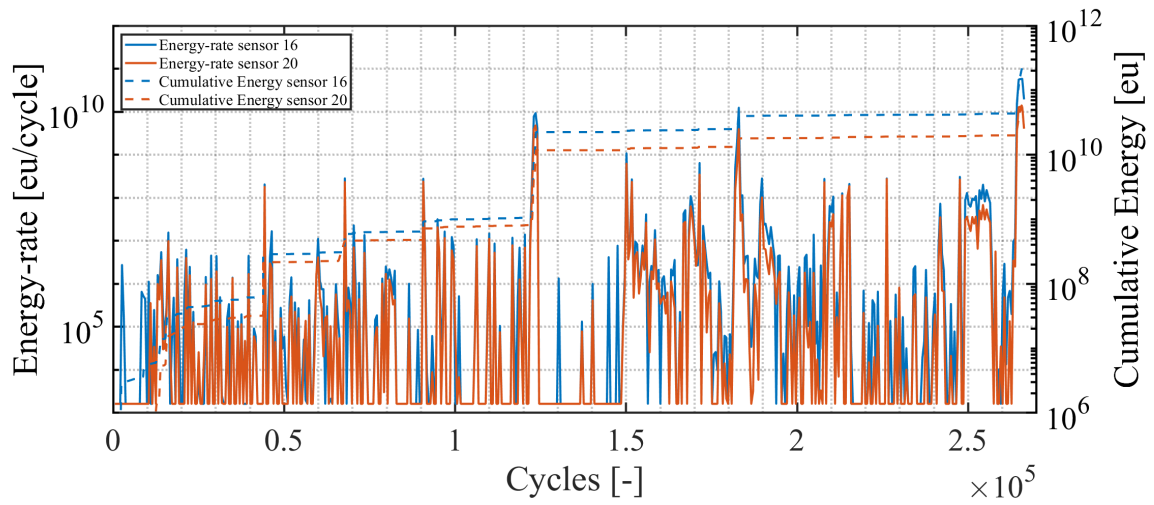


Figure 4.43: Hydrophone energy-rate sample 3

Figure 4.44 shows the recorded hits in the last 6000 load cycles leading up to failure. The visual observation shows that the fatigue crack is propagating. The hydrophones record little to zero hits in the first 3.500 cycles, whereas the record at a rate of 30-50 hits per cycle in the last 2.500 cycles. This extreme jump in hit-rate shows that there is potential for these hydrophones, but that at this stage they could be unreliable.

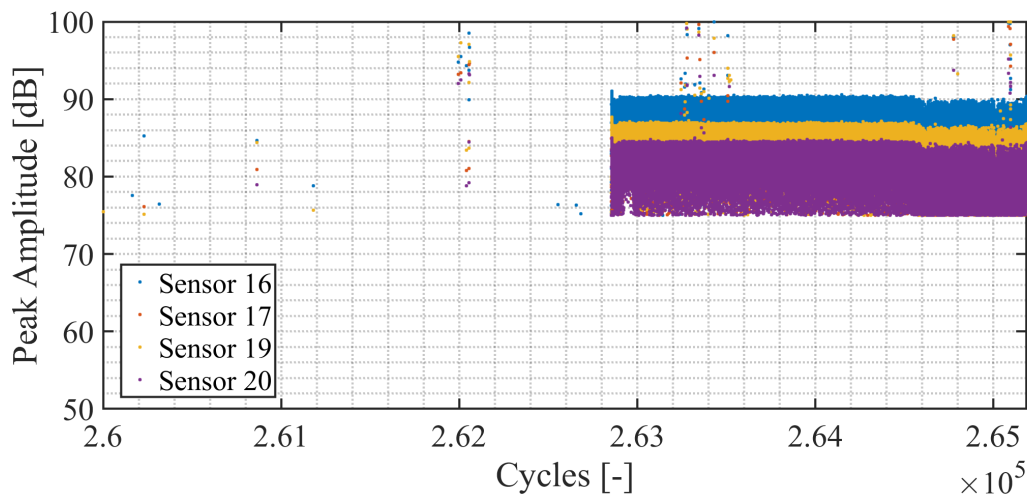


Figure 4.44: Hydrophone activity before final failure

4.3. Discussion

The loading conditions for the three executed experiments are quite similar. The starting conditions, however, were entirely different. The effect of pre-corrosion had the biggest influence on the fatigue life sample 1. The large differences in obtained fatigue life, being 107.000, 396.000 and 273.000 cycles, make it challenging to compare the observed phenomena in the AE data.

4.3.1. Correlation of signal parameters to damage evolution

In general, for sample 1 there is good correlation between the damage evolution and the hit-rate of the sensors directly in front of the crack. However, there are two phenomena making the outcome less reliable. First, the activity recorded by the sensor directly in front of the crack is recorded by other sensors with higher magnitude. And second, the period of less recorded activity just before failure casts doubt on the effectiveness of using hit-rate and energy-rate alone to describe the state of integrity during the corrosion-fatigue damage evolution.

The trends observed in sample 2 showed similar trends compared to sample 1 with alternating periods of elevated rates of emission and quiet phases. However, the absolute values of the parameters differ significantly. The hit-rate for sample 2 is, on average, almost 2 orders of magnitude lower than for sample 1. And the majority of the hits recorded for sample two ranged from 50 - 55 dB. These hits would not have been recorded if the threshold level of sample 1, which was 55 db, had been applied.

If the final 100.000 cycles of sample 2 are compared to sample 1, the trends of the rate of emission show some resemblance. In these stages, an increased rate of emission for energy and hits is observed. This increase in activity might suggest that fatigue crack are reaching the stable propagation phase.

The recurring AE behaviour that is recorded during the experiment of sample 3 shows little to no resemblance to the behaviour of sample 1 and 2. The energy levels of the generated signals are more or less in the same order of magnitude. But the hit-rate for sample 3 does not shows any similarity to sample 1 and 2. It varies throughout different stages in the experiment from 1-3 hits/cycle to 0.001 hits/cycle. Based on these parameters, it is not possible to identify different stages of fatigue crack propagation except for final failure.

The recorded data of the custom in-house made hydrophones looks promising, but shows too large variations in activity and is therefor not considered in the evaluation of the effectiveness of the primary features to correlate to the damage evolution.

Signal severity level

The distribution of the hits based on their signal parameters energy and duration lead to some interesting results. It is insightful to see the evolution of the hit-rate for the three different signal levels and could be considered a useful complementary tool. Substituting this differentiation for the SNR filter, which sometimes eliminates relevant signals, is not recommended because it has lead to misleading results regarding the location of the crack. Additionally, the downside of processing the hit-rate of unfiltered data is that it takes significantly more computational time to process the high amount of hits.

4.3.2. Characterization of different damage mechanisms

The energy-duration distribution of the recorded hits in the various stages can be used to distinguish between the corrosion-induced hits and the fatigue-induced hits. Figure 4.45 shows the energy-duration distribution for both corrosion-fatigue testing and corrosion only testing. From the figure can be seen that the corrosion-induced hits have longer duration for the same energy levels as the fatigue-induced hits. It must be kept in mind that the duration of the corrosion-induced hits were assessed using a 40 dB threshold. A 50 dB threshold would lower the duration of the corrosion induced hits. Further

investigation on the influence of threshold level on duration and the applicability of this method to distinguish between corrosion-induced and fatigue-induced hits is recommended.

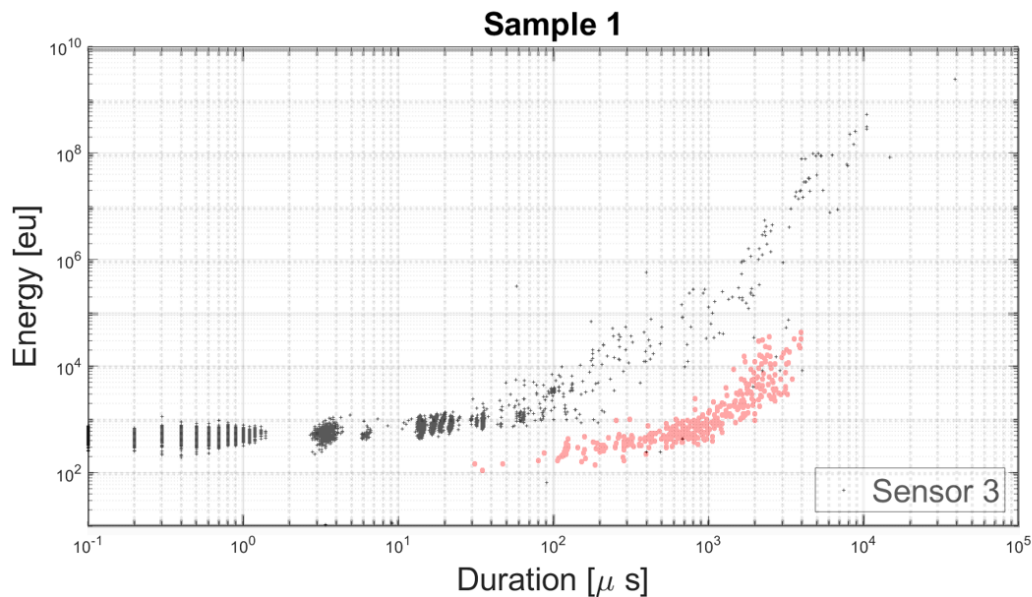


Figure 4.45: Energy-duration distribution during corrosion-fatigue measurements (black) and corrosion only (red)

4.3.3. Experiments improvements

In this final section, I would like to give some suggestions for future experiments. There are several elements that could be improved to increase the effectiveness of the experimental set-up.

- **Corrosion-particles**

Already after a day or two of accelerated corrosion, the water in the corrosion cell starts to become so polluted that it becomes increasingly difficult to make visual observations of high quality. Refreshing the water every day would be a waste of time, money and salt, because it is difficult to remove all the corrosion particles that have settled on the bottom of the water tank. In order to ensure a clean tank throughout the tests, the experimental set-up can be complemented with an external filter. With some investigation, there should be several options to implement this.

- **Epoxy layer**

The visual observation of the crack length of sample 3 did not provide the desired results. One of the reasons for this is that the crack path of the epoxy layer did not align with the steel crack path. Perhaps some type of grease can be used to treat the specimens in advance to the experiment. Another reason for the low quality images is the polluted water, as discussed in the previous item.

- **INSTRON**

To prevent the same amount of data recorded for sample 3, it is suggested to take another look at the fatigue machine. For regular fatigue tests, a vibrating machine is might not be a huge deal. But for sensitive test like these it seems to influence the outcome so badly, that it is of great importance that this possible source of noise is eliminated before commencing new experiments.

- **Strain gauge**

The data of the strain gauge was not recorded accurately during the experiment because the sampling rate was too low. Therefore it has not been used in the analysis. The elongation of the specimen is also recorded by the INSTRON, which is automatically saved if needed. However, measuring the elongation with the fatigue testing device might lead to latency problems. In a new round of testing, the strain gauge should be placed on the other side of the specimen and higher

than the exposed surface. It is expected that it will interfere less with the AE sensors. Additionally, the DAQ should be sampling this sensor better in order to make it more useful.

- **Hydrophones**

Additional research on appropriate threshold levels of the hydrophones is needed. It is shown that the sensitivity of these sensors is high and show potential in recording signals that have not been recorded by the AE sensors. However, it is suggested to find commercially available hydrophones instead of using in-house developed sensors to assure continuity in the experiments.

5

Conclusions and future work

In this chapter, the conclusions of this work are summarized by reflecting on the research questions:

5.1. Conclusion

In order to answer the main research question, the sub questions are answered first.

- *What is the contribution of corrosion-induced AE during corrosion-fatigue testing of submerged mooring chain steel?*

The recorded hit-rate of the corrosion induced AE depends on the applied threshold by the data acquisition system. For a threshold of 50 dB, as used in during the fatigue test, the hit-rate of the corrosion-induced events is between 0.01 and 0.001 hits per second. This means, on average, an equivalent of one hit for every thousand load cycles. This is a negligible contribution compared to the fatigue induced hit-rates that were observed in the fatigue tests presented in this report.

Additionally, corrosion-induced hits are characterized with longer duration in comparison to fatigue-induced hits. Therefore, it may be concluded that the energy-duration character has potential to discriminate between corrosion- and fatigue-induced AE.

- *How do the acoustic emission features change throughout the different stages of fatigue crack growth?*

The hit-rate and the energy-rate were found to be important indicators for different stages of crack growth. Energy-rate is the feature that is waveform dependent and most sensitive to identify anomalies in the data set. Based on the experiments of sample 1,2 and 3, the combined elevation of hit-rate and energy-rate is observed towards the later stages in the corrosion-fatigue degradation process.

Note that the waves are convolved with the transfer functions of the media and the sensors. This makes it difficult to value the reliability of the primary features. Compared to the other primary features, hit-rate is the least sensitive to the modification of the signal during propagation.

- *Is it possible to distinguish between sub-stages of fatigue crack growth based on the primary features?*

Based on the global analyses, the hit-rate for the three different levels of severity show good correlation to the damage evolution. However, it is not yet possible to distinguish different stages of crack growth because the data for experiment 1,2 and 3 vary so widely.

The data of sample 1 and 2 shows that the period leading up to crack initiation consists of low hit-rate and energy-rate. The first part of the crack propagation stage is related to an increase in hit-rate and energy-rate. The magnitude of the rate of emission seems to decay in the stage leading up to final failure. During final failure, the rates of emission take extreme values.

An accurate measurement of the crack length, and thus the stress intensity factor range ΔK , would have improved the possibility to distinguish different sub-stages of crack growth. The layer of epoxy prohibited an accurate measurement of the crack length of sensor 3.

The main research question of the thesis was:

'Which of the acoustic emission primary features can most accurately correlate to the corrosion-fatigue damage evolution of submerged mooring chain steel using non-contact sensors?'

Based on the global parametric analysis performed in this thesis, for sample 1 and 2, the hit-rate and energy-rate show good correlation to the corrosion-fatigue damage evolution. A differentiation in signal severity based on their energy and duration can be a useful tool to expose the relative contribution throughout the fatigue life. However, the global features seem to differ notably between different samples, hence performing assessment based on global features is not considered sufficient, and more advanced local analysis is required to improve the reliability.

The number of experiments on which these conclusions are based is small and should be extended to draw more decisive conclusions. As discussed in the end of Chapter 4, the hydrophones should be further tested to quantify their capabilities. As for now they show potential, but also remarkably strange behaviour.

The hypothesis presented in Chapter 2 cannot be confirmed with the obtained data. It is still possible that the generation of signals increases in magnitude and frequency in the final stages leading up to failure. Perhaps, the non-contact sensors were not able to record them.

5.2. Recommendations

Based on the above mentioned conclusions, the following recommendations for future research are derived. Afterwards some suggestions will be made on how to improve a new round of corrosion-fatigue experiments.

- The quality of the measurements made with non-contact sensors is promising. However, experiments with both contact and non-contact sensors will allow for more accurate assessment of the transmission losses for non-contact sensors.
- The current analysis focused on the time domain features. For future research, it can be very interesting to investigate the evolution in the frequency content of the signals. Already it was observed in this thesis that the frequency content of the hits varied considerably.
- In addition to previous recommendation, the measured signal is strongly influenced by the recording devices. Therefore, it is suggested to look into other AE sensors that are capable of recording a wider range of frequencies.
- The current experiments require several days of testing. In order to save time. It is possible to modify the test matrix in a way that experiments can be performed in less time. First examining multiple samples in the low cycle fatigue region and then extending it to the high cycle fatigue region could be good way to resume the research.

-
- For the practical purpose of monitoring offshore mooring chains, it is advised to start test measurements in operating conditions. An assessment of the environmental noise monitored in more representative situations could expose external unknown sources of ultrasound waves.



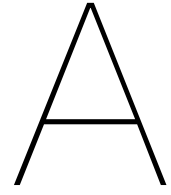
Figure 5.1: Visual inspection of full-scale mooring chain of the MARAN ARES.

References

- [1] <https://www.sofec.com/mooring-systems/>. *Figure of External Turret on Mooring System FPSO*. URL: <https://www.sofec.com/mooring-systems/>. (accessed: 07.03.2022).
- [2] Clean Energy Wire. *In the media: Floating wind turbines, RWE restructuring plans*. URL: <https://www.cleanenergywire.org/news/media-floating-wind-turbines-rwe-restructuring-plans>. (accessed: 16.06.2022).
- [3] Robert B Gordon, Martin G Brown, and Eric M Allen. "Mooring integrity management: a state-of-the-art review". In: *Offshore technology conference*. OnePetro. 2014.
- [4] Kai-tung Ma, Hongbo Shu, Philip Smedley, Didier L'Hostis, and Arun Duggal. "A historical review on integrity issues of permanent mooring systems". In: (2013).
- [5] Emmanuel Fontaine, Andrew Kilner, Christopher Carra, Daniel Washington, KT Ma, Amal Phadke, Derrick Laskowski, and Greg Kusinski. "Industry survey of past failures, pre-emptive replacements and reported degradations for mooring systems of floating production units". In: *Offshore technology conference*. OnePetro. 2014.
- [6] Remco Hageman, Pieter Aalberts, Richard Leeuwenburgh, and Nicola Grasso. "Integrity management of mooring systems". In: *Offshore Technology Conference*. OnePetro. 2019.
- [7] Feng Wen, Julie Pray, Kevin McSweeney, and Hai Gu. "Emerging inspection technologies—Enabling remote surveys/inspections". In: *Offshore Technology Conference*. OnePetro. 2019.
- [8] Ruqiang Yan, Xuefeng Chen, and Subhas C Mukhopadhyay. "Advanced signal processing for structural health monitoring". In: *Structural Health Monitoring*. Springer, 2017, pp. 1–11.
- [9] Charles R Farrar and Keith Worden. "An introduction to structural health monitoring". In: *Philosophical Transactions of the Royal Society A: Mathematical, Physical and Engineering Sciences* 365.1851 (2007), pp. 303–315.
- [10] Christoph Kralovec and Martin Schagerl. "Review of structural health monitoring methods regarding a multi-sensor approach for damage assessment of metal and composite structures". In: *Sensors* 20.3 (2020), p. 826.
- [11] Edward McCafferty. *Introduction to corrosion science*. Springer Science & Business Media, 2010.
- [12] AE Potts, Emmanuel Fontaine, and Robert Melchers. "Investigation of severe corrosion of mooring chain in West African waters". In: *Proc. Conf. Corrosion & Prevention, Melbourne*. 2012.
- [13] Marion Fregonese, Hassane Idrissi, Henri Mazille, Luc Renaud, and Y Cetre. "Initiation and propagation steps in pitting corrosion of austenitic stainless steels: monitoring by acoustic emission". In: *Corrosion science* 43.4 (2001), pp. 627–641.
- [14] C Jirarungsatian and A Prateepasen. "Pitting and uniform corrosion source recognition using acoustic emission parameters". In: *Corrosion Science* 52.1 (2010), pp. 187–197.
- [15] Junlei Tang, Junyang Li, Hu Wang, Yingying Wang, and Geng Chen. "In-situ monitoring and analysis of the pitting corrosion of carbon steel by acoustic emission". In: *Applied Sciences* 9.4 (2019), p. 706.
- [16] Jian Xu, Xinqiang Wu, and En-Hou Han. "Acoustic emission during pitting corrosion of 304 stainless steel". In: *Corrosion Science* 53.4 (2011), pp. 1537–1546.
- [17] Jaap Schijve. *Fatigue of structures and materials*. Springer, 2009.
- [18] Jonathan Fernández, Walther Storesund, and Jesús Navas. "Fatigue performance of grade R4 and R5 mooring chains in seawater". In: *International Conference on Offshore Mechanics and Arctic Engineering*. Vol. 45370. American Society of Mechanical Engineers. 2014, V01AT01A035.

- [19] V Moorthy, T Jayakumar, and Baldev Raj. "Influence of micro structure on acoustic emission behavior during stage 2 fatigue crack growth in solution annealed, thermally aged and weld specimens of AISI type 316 stainless steel". In: *Materials Science and Engineering: A* 212.2 (1996), pp. 273–280.
- [20] DG Aggelis, EZ Kordatos, and TE Matikas. "Acoustic emission for fatigue damage characterization in metal plates". In: *Mechanics Research Communications* 38.2 (2011), pp. 106–110.
- [21] TM Morton, RM Harrington, and JG Bjeletich. "Acoustic emissions of fatigue crack growth". In: *Engineering fracture mechanics* 5.3 (1973), pp. 691–697.
- [22] Paul Paris and Fazil Erdogan. "A critical analysis of crack propagation laws". In: (1963).
- [23] TM Roberts and M Talebzadeh. "Acoustic emission monitoring of fatigue crack propagation". In: *Journal of constructional steel research* 59.6 (2003), pp. 695–712.
- [24] Jianguo Yu, Paul Ziehl, Boris Zárate, and Juan Caicedo. "Prediction of fatigue crack growth in steel bridge components using acoustic emission". In: *Journal of Constructional Steel Research* 67.8 (2011), pp. 1254–1260.
- [25] Masoud Rabiei and Mohammad Modarres. "Quantitative methods for structural health management using in situ acoustic emission monitoring". In: *International Journal of Fatigue* 49 (2013), pp. 81–89.
- [26] Jalaj Kumar, S Ahmad, CK Mukhopadhyay, T Jayakumar, and Vikas Kumar. "Acoustic emission studies for characterization of fatigue crack growth behavior in HSLA steel". In: *Nondestructive Testing and Evaluation* 31.1 (2016), pp. 77–96.
- [27] Mengyu Chai, Jin Zhang, Zaoxiao Zhang, Quan Duan, and Guangxu Cheng. "Acoustic emission studies for characterization of fatigue crack growth in 316LN stainless steel and welds". In: *Applied acoustics* 126 (2017), pp. 101–113.
- [28] Mengyu Chai, Zaoxiao Zhang, Quan Duan, and Yan Song. "Assessment of fatigue crack growth in 316LN stainless steel based on acoustic emission entropy". In: *International Journal of Fatigue* 109 (2018), pp. 145–156.
- [29] Seyed Fouad Karimian, Mohammad Modarres, and Hugh A Bruck. "A new method for detecting fatigue crack initiation in aluminum alloy using acoustic emission waveform information entropy". In: *Engineering fracture mechanics* 223 (2020), p. 106771.
- [30] Christine M Sauerbrunn, Ali Kahirdeh, Huisung Yun, and Mohammad Modarres. "Damage assessment using information entropy of individual acoustic emission waveforms during cyclic fatigue loading". In: *Applied Sciences* 7.6 (2017), p. 562.
- [31] Md Yeasin Bhuiyan, Jingjing Bao, Banibrata Poddar, and Victor Giurgiutiu. "Analysis of acoustic emission waveforms from fatigue cracks". In: *Health Monitoring of Structural and Biological Systems 2017*. Vol. 10170. International Society for Optics and Photonics. 2017, 101702A.
- [32] Md Yeasin Bhuiyan, Jingjing Bao, Banibrata Poddar, and Victor Giurgiutiu. "Toward identifying crack-length-related resonances in acoustic emission waveforms for structural health monitoring applications". In: *Structural Health Monitoring* 17.3 (2018), pp. 577–585.
- [33] Thierry Palin-Luc, Rubén Pérez-Mora, Claude Bathias, Gonzalo Domínguez, Paul C Paris, and Jose Luis Arana. "Fatigue crack initiation and growth on a steel in the very high cycle regime with sea water corrosion". In: *Engineering Fracture Mechanics* 77.11 (2010), pp. 1953–1962.
- [34] H Chang, E Han, JQ Wang, and W Ke. "Acoustic emission study of corrosion fatigue crack propagation mechanism for LY12CZ and 7075-T6 aluminum alloys". In: *Journal of materials science* 40.21 (2005), pp. 5669–5674.
- [35] Fernando Galvan Rivera, Graham Edwards, Elvin Eren, and Slim Soua. "Acoustic emission technique to monitor crack growth in a mooring chain". In: *Applied Acoustics* 139 (2018), pp. 156–164.
- [36] Ángela Angulo, Jialin Tang, Ali Khadimallah, Slim Soua, Cristinel Mares, and Tat-Hean Gan. "Acoustic emission monitoring of fatigue crack growth in mooring chains". In: *Applied Sciences* 9.11 (2019), p. 2187.

- [37] Ángela Angulo, Cristinel Mares, and Tat-Hean Gan. “Diagnostic Feature Extraction and Filtering Criterion for Fatigue Crack Growth Using High Frequency Parametrical Analysis”. In: *Sensors* 21.15 (2021), p. 5030.
- [38] FPSO Forum. *FPSO Forum welcome page*. URL: <https://www.fpsforum.com>. (accessed: 07.03.2022).
- [39] Christian U Grosse, Masayasu Ohtsu, Dimitrios G Aggelis, and Tomoki Shiotani. *Acoustic Emission Testing: Basics for Research-Applications in Engineering*. Springer Nature, 2021.
- [40] Josef Krautkrämer and Herbert Krautkrämer. *Ultrasonic testing of materials*. Springer Science & Business Media, 2013.
- [41] S. Alkhateeb. “Feasibility evaluation for non-contact ultrasonic inspection of mooring chains through marine growth.” In: *TU Delft repository* (2020).
- [42] Lotfollah Pahlavan and Gerrit Blacquièrre. “Fatigue crack sizing in steel bridge decks using ultrasonic guided waves”. In: *Ndt & E International* 77 (2016), pp. 49–62.
- [43] Bart Scheeren, Mirosław Lech Kaminski, and Lotfollah Pahlavan. “Evaluation of Ultrasonic Stress Wave Transmission in Cylindrical Roller Bearings for Acoustic Emission Condition Monitoring”. In: *Sensors* 22.4 (2022), p. 1500.
- [44] Victor Igwemezie and Ali Mehmanparast. “Waveform and frequency effects on corrosion-fatigue crack growth behaviour in modern marine steels”. In: *International Journal of Fatigue* 134 (2020), p. 105484.
- [45] M Nani Babu, CK Mukhopadhyay, and G Sasikala. “Fatigue crack growth study in p91 and 316ln steels using acoustic emission”. In: *Transactions of the Indian Institute of Metals* 72.12 (2019), pp. 3067–3080.
- [46] Mengyu Chai, Xinglong Hou, Zaoxiao Zhang, and Quan Duan. “Identification and prediction of fatigue crack growth under different stress ratios using acoustic emission data”. In: *International Journal of Fatigue* (2022), p. 106860.
- [47] DNV GL - OS - E302. *Offshore Mooring Chain*. URL: <https://rules.dnv.com/docs/pdf/DNV/os/2015-07/DNVGL-OS-E302.pdf>. (accessed: 28.02.2022).
- [48] DNV GL OS E301. *Position Mooring*. URL: <https://rules.dnv.com/docs/pdf/DNV/os/2018-07/dnvg1-os-e301.pdf>. (accessed: 01.03.2022).



Primary Features

A.1. Sample 1

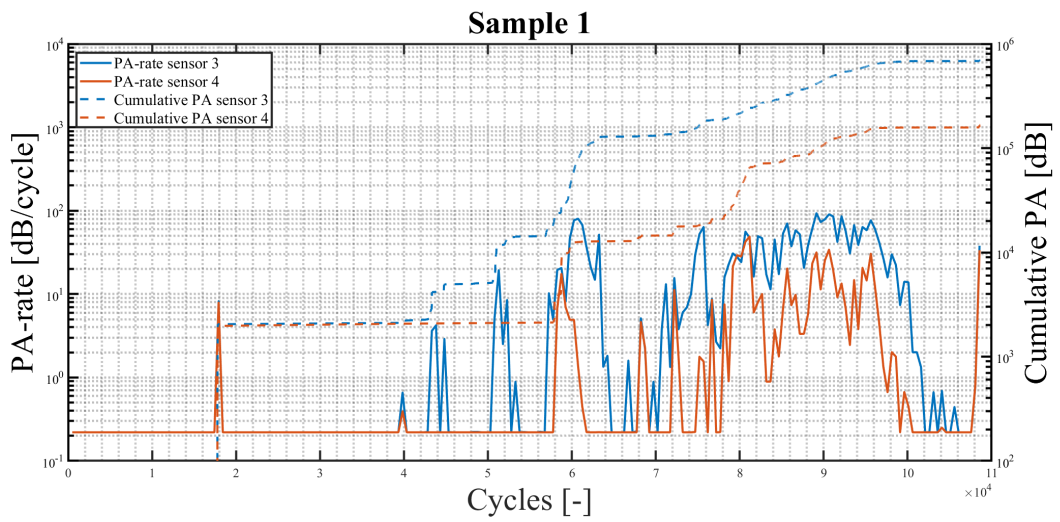


Figure A.1: -

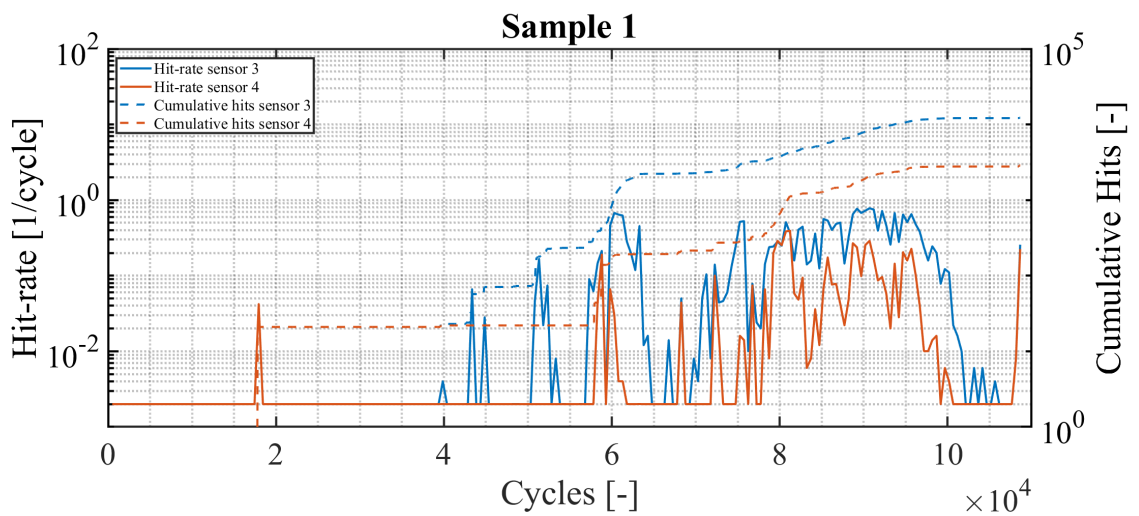


Figure A.2: -

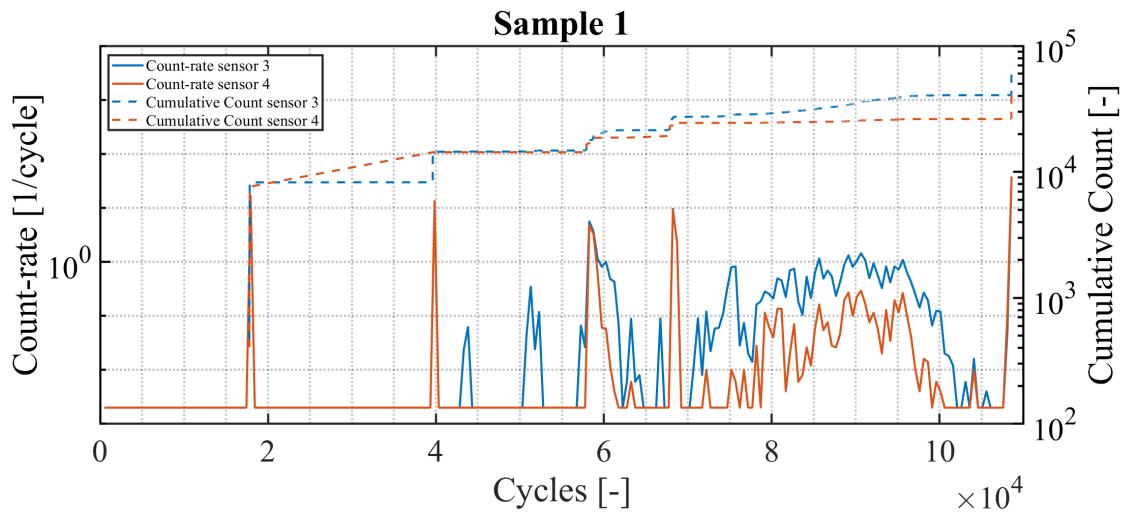


Figure A.3: -

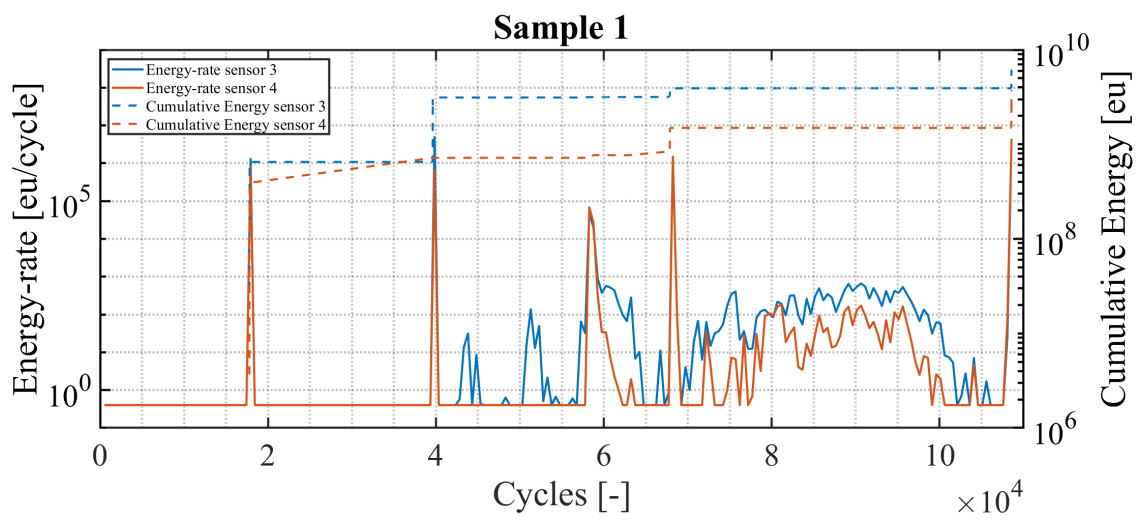


Figure A.4: -

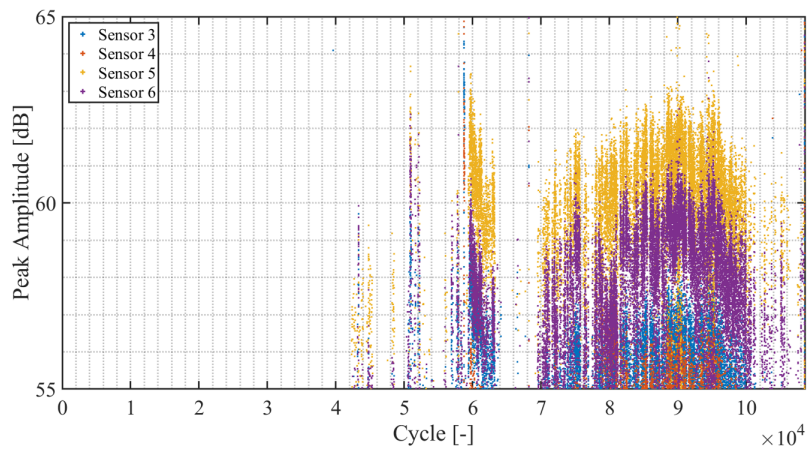


Figure A.5: Peak Amplitude vs. cycles for four sensors Sample 1

A.2. Sample 2

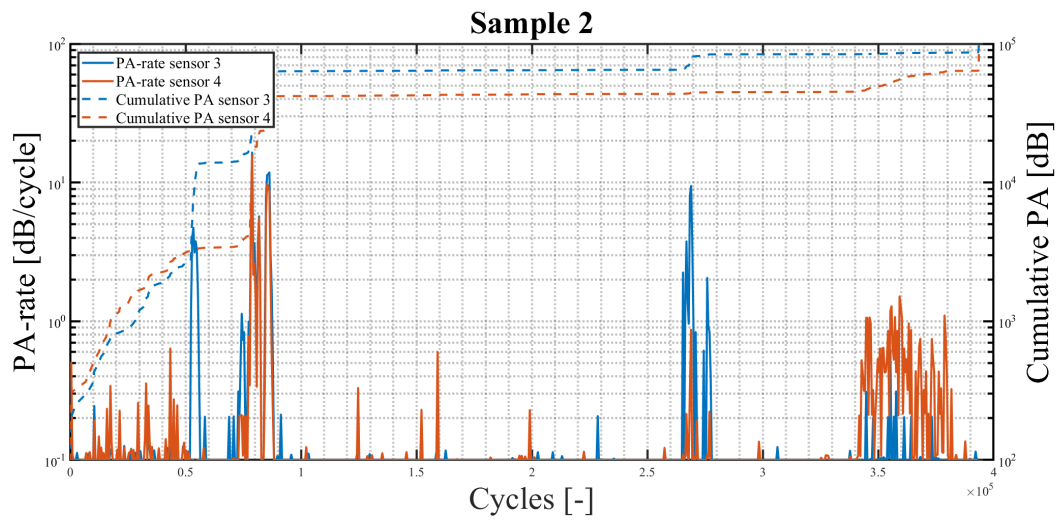


Figure A.6: –

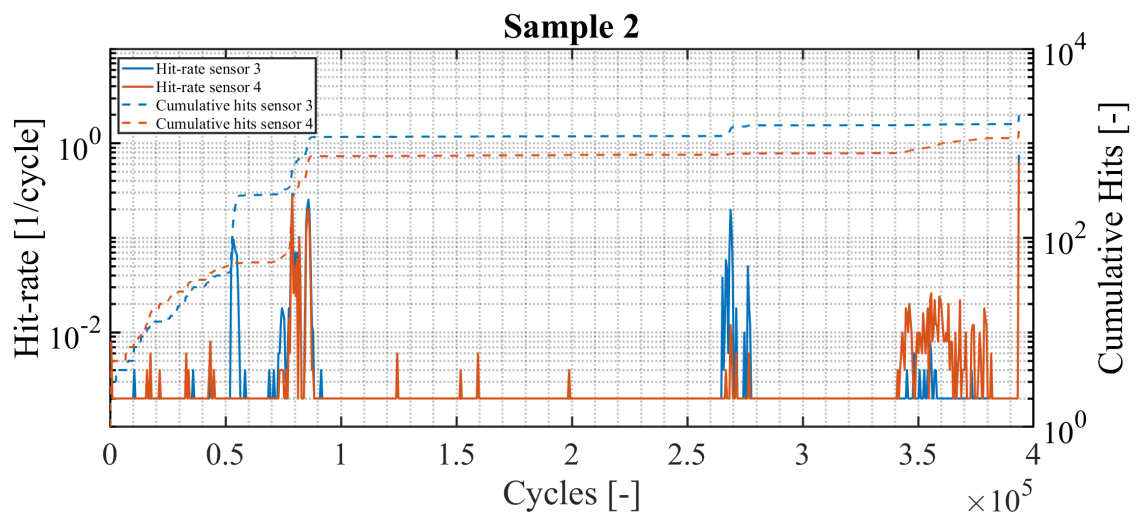


Figure A.7: –

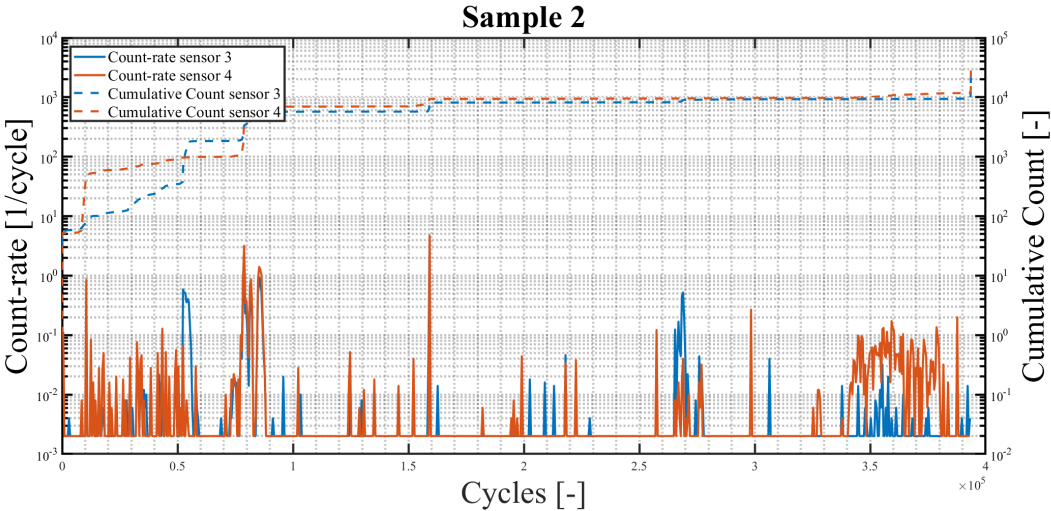


Figure A.8: -

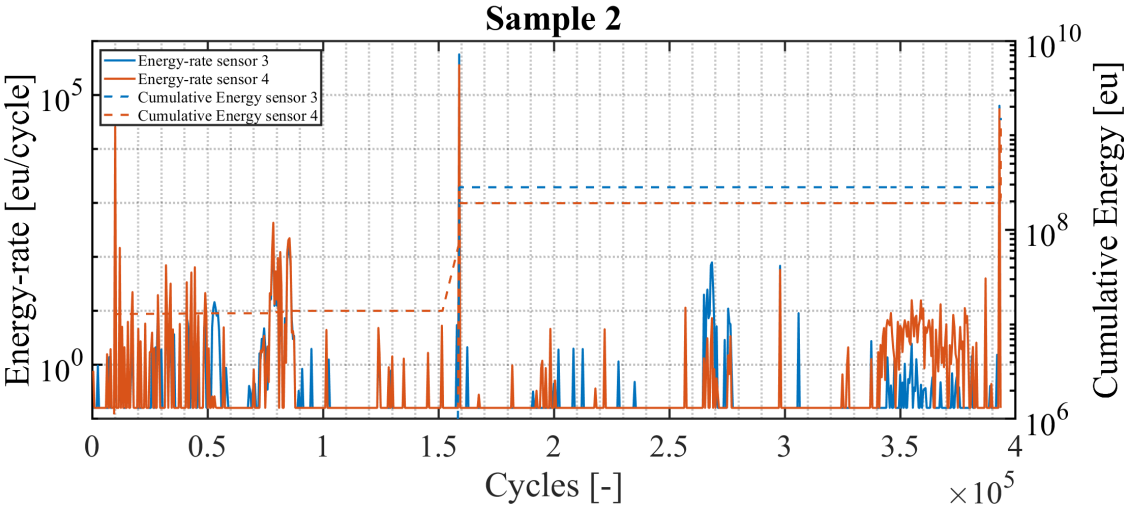


Figure A.9: -

A.3. Sample 3

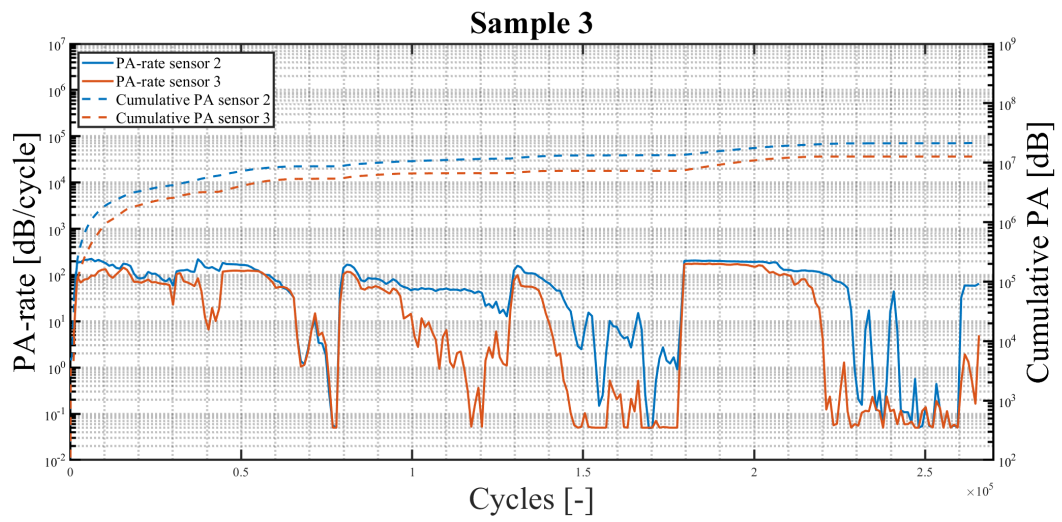


Figure A.10: –

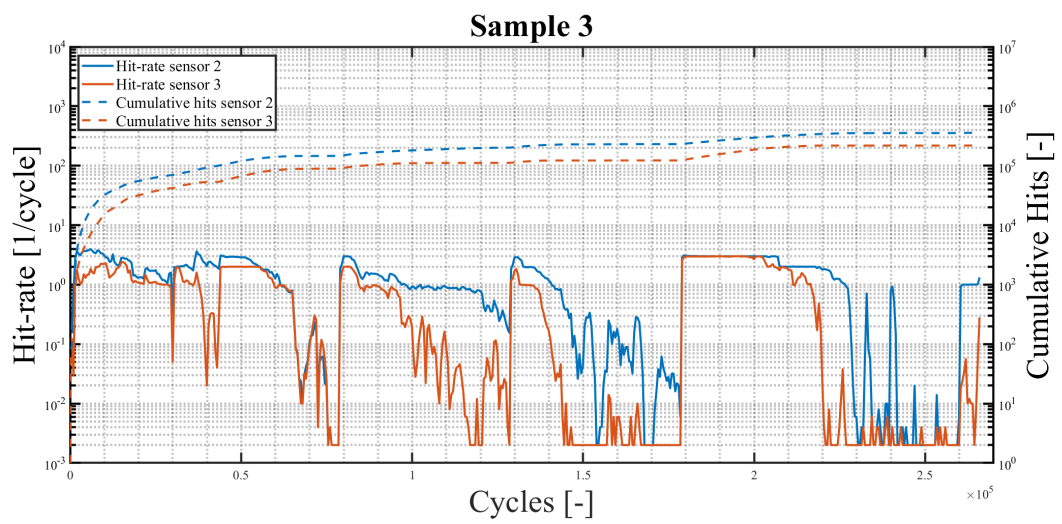


Figure A.11: –

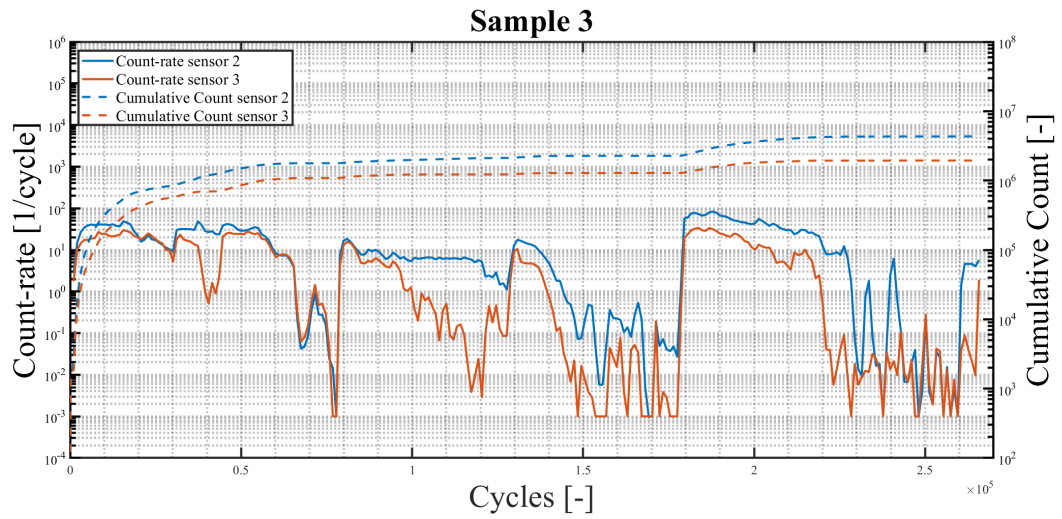


Figure A.12: –

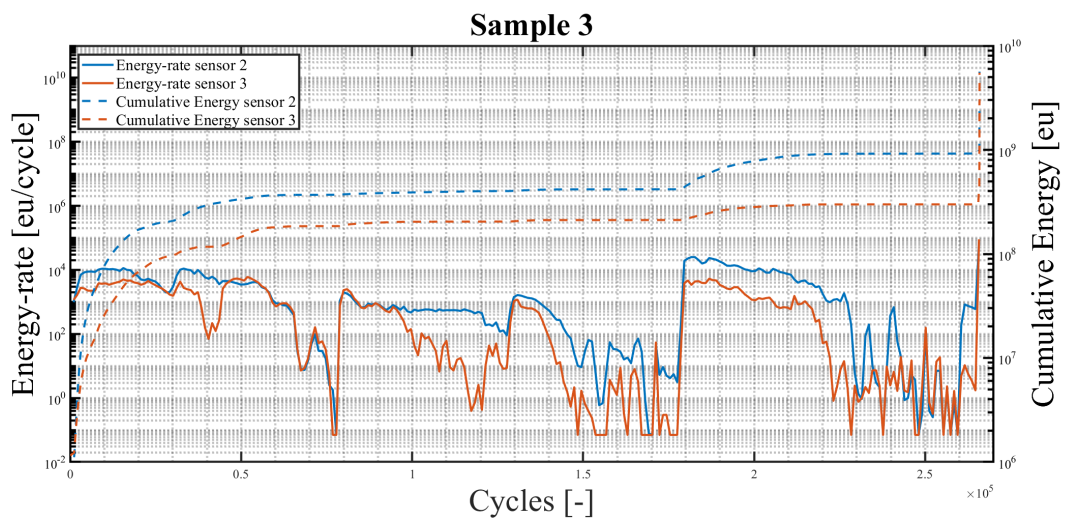
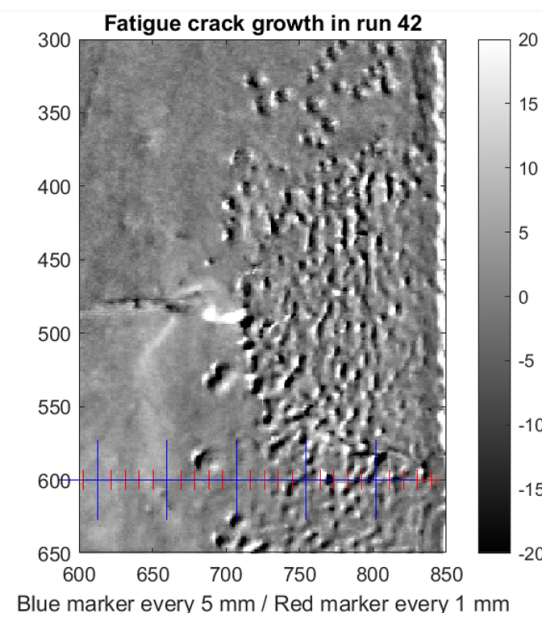
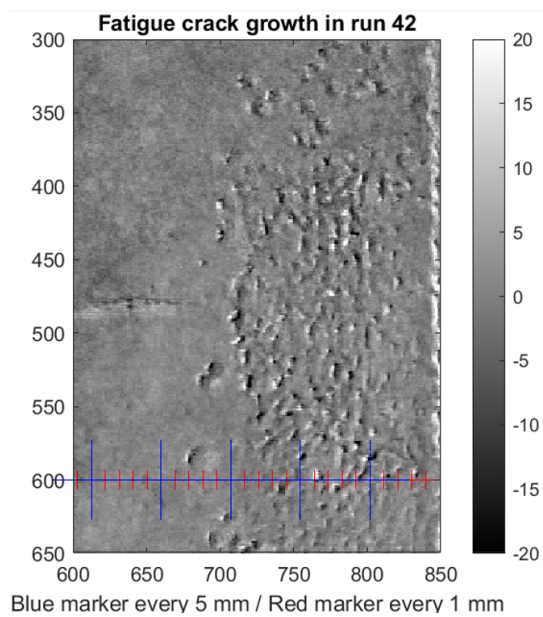


Figure A.13: –

B

Footage & Crack size measurement



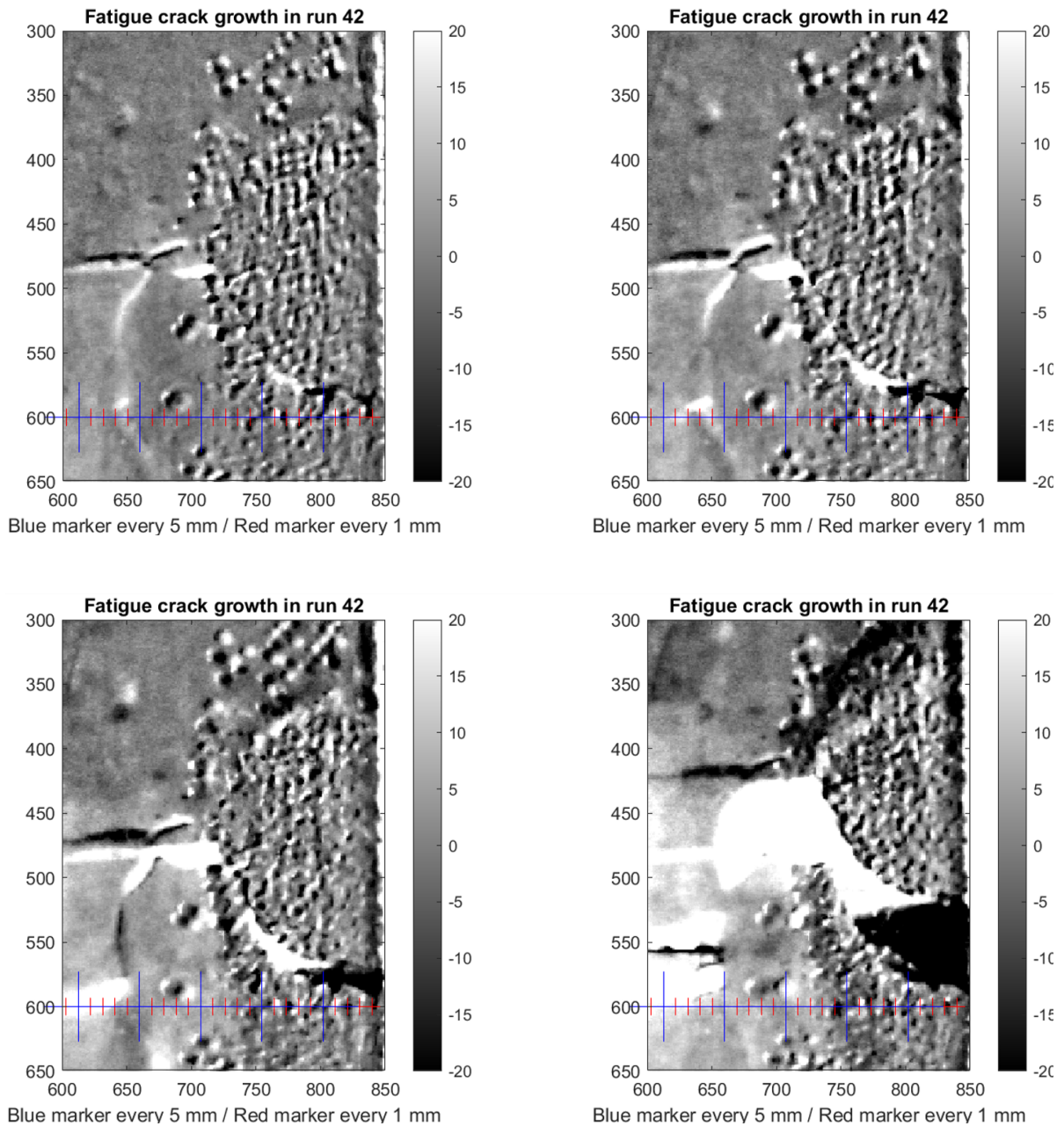
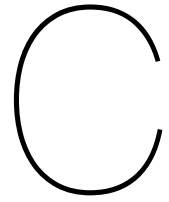


Figure B.1: Six frames of the crack propagation video.



Pre-Corrosion data

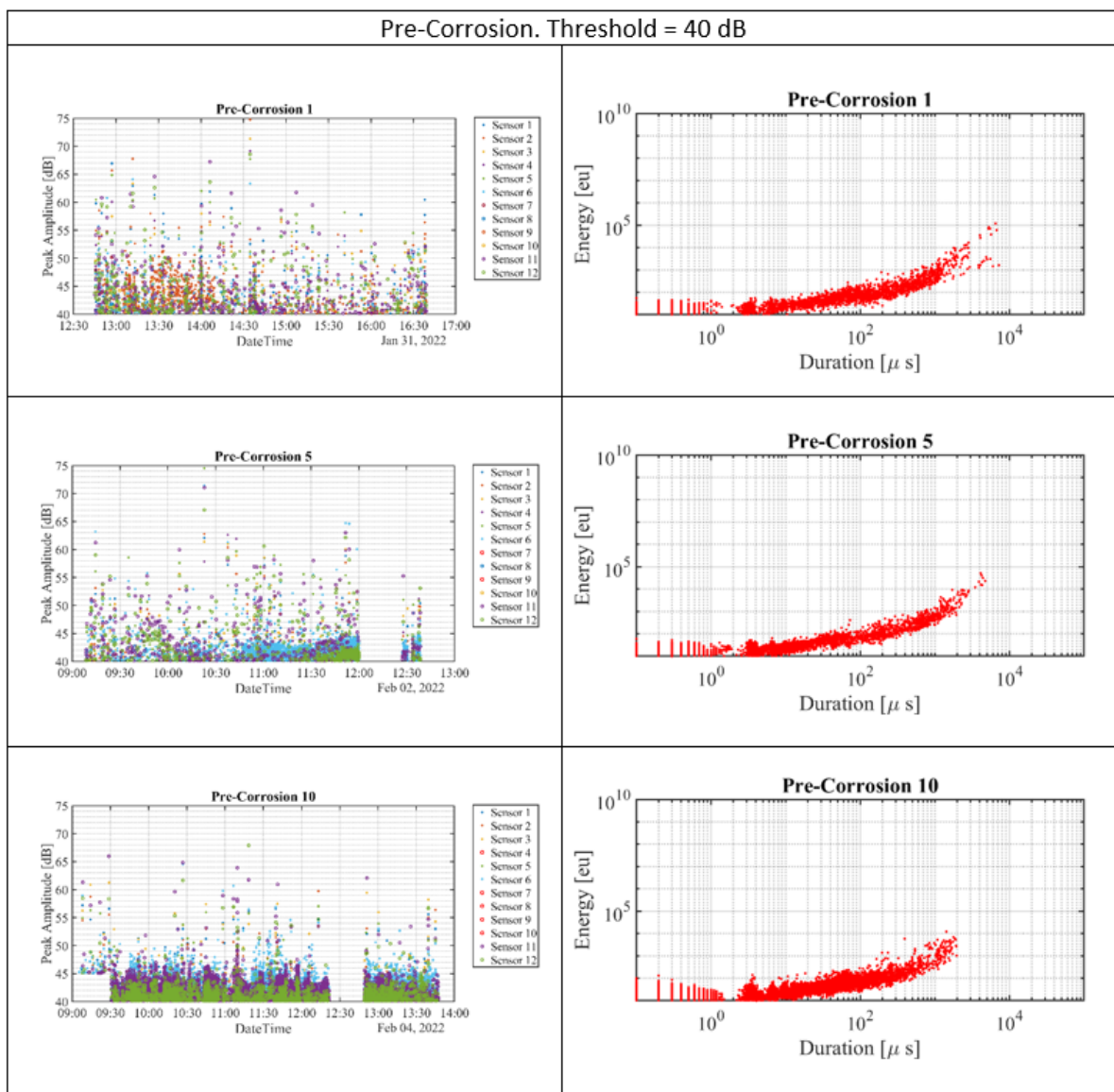


Figure C.1: –

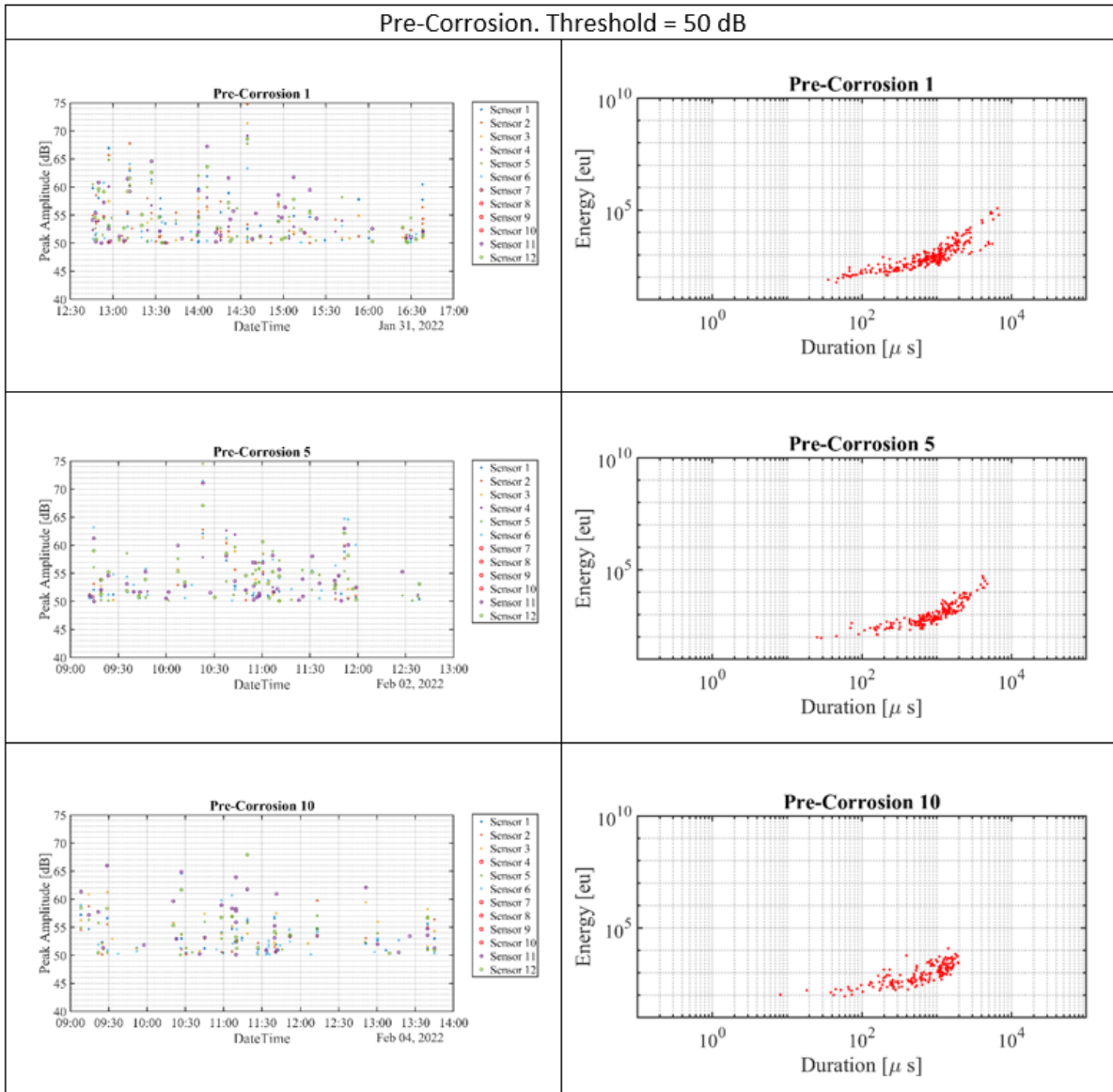


Figure C.2: –